Gluino and Squark Pair Production
at
Future Linear Colliders

Dissertation
zur Erlangung des Doktorgrades
des Fachbereichs Physik
der Universität Hamburg

vorgelegt von
Stefan Berge
aus Leipzig

Hamburg
2003

Zusammenfassung

In der vorliegenden Arbeit werden die Squark- und Gluino-Paarproduktion an zukünftigen Linearbeschleunigern in Elektron-Positron Annihilation und Photon-Photon Kollision untersucht. Die Gluino-Paarerzeugung wird für beide Streuarten analysiert. Alle Feynman Diagramme in niedrigster Ordnung sind Einschleifendiagramme, in denen Squarks und Quarks umlaufen. Aufgrund destruktiver Interferenz der einzelnen Schleifenbeiträge ist eine Messung von Gluino-Paaren in Elektron-Positron Annihilation für Gluinomassen größer als 200 GeV nur äußerst eingeschränkt zu erwarten. In Photon-Photon Streuung hingegen ist mit einer Signalrate von bis zu 6000 Ereignissen pro Jahr für leichte Squarks (350 GeV) und leichte Gluinos (300 GeV) bei einer Luminosität von $330\,fb^{-1}$ zu rechnen. Falls die Squarkmassen 700 GeV nicht übersteigen, treten Signalraten von 300 Ereignissen pro Jahr für Gluinomassen bis 1700 GeV auf. Weiterhin werden die Beiträge durch aufgelöste Photonen untersucht. Diese können nicht vernachlässigt werden, wenn die Schwerpunktsenergie viel größer als die Produktionsschwelle der Teilchen ist oder falls die Gluinos leicht (200 GeV) und die Squarks sehr schwer sind (1500 GeV).

Außerdem wird die Squark-Paarproduktion in Photon-Photon Streuung untersucht. Da dieser Prozess bereits auf Born-Niveau stattfindet, ist der Wirkungsquerschnitt von geeigneter Größe, um Präzisionsmessungen durchzuführen. Deshalb werden die kompletten MSSM Einschleifen-Korrekturen berechnet, und deren Einfluss am Beispiel der beiden Benchmark Punkte SPS1 und SPS5 aufgezeigt. Hierbei wurde ermittelt, dass sowohl QCD-Korrekturen als auch die elektroschwachen Korrekturen wichtig sind. Darüberhinaus besitzen beide Korrekturen ein entgegengesetztes Vorzeichen, wodurch sich für Energien, die etwas größer als die Produktionsschwelle der auslaufenden Teilchen sind, stabile Korrekturen von -5% für SPS1 und $+10\%$ für SPS5, ergeben. Die Beiträge aufgelöster Photonen zur Squarkproduktion sind nur für leichte Squarks um 200 GeV und hohe Schwerpunktsenergien von Bedeutung.

Abstract

In this thesis gluino and squark pair production processes at future linear colliders are considered. The scattering processes relevant for the pair production are the electron-positron annihilation and the photon-photon collisions. The gluino pair production is analyzed for both cases. The Feynman diagrams are all one-loop with squarks and quarks inside the loops. Unfortunately, the matrix elements in electron-positron annihilation interfere destructively, and only very optimistic MSSM parameters lead to 65 detectable gluino pairs per year. In photon-photon scattering, however, up to 6000 events per year are expected for light squarks (350 GeV) and light gluinos (300 GeV), and a photon-photon luminosity of $330\,fb^{-1}$. If the squark masses increase up to 700 GeV, around 300 events per year are expected almost independently from the gluino mass. The resolved contributions were found to be important for center-of-mass energies much higher than the pair production threshold or light gluino masses (200 GeV) and heavy squarks masses (1500 GeV).

Furthermore, the squark pair production in photon-photon collisions is discussed. Since the scattering process occurs at Born level, large cross sections arise that offer the

possibility of precision measurements. Moreover, the full MSSM next-to-leading order corrections are calculated for the benchmark points SPS1 and SPS5. It has been shown that the QCD as well as the electroweak corrections are important, summing to an overall contribution of -5% for SPS1 and $+10\%$ for SPS5, for energies far above the production threshold. The resolved contributions are only important for light squark masses of 200 GeV and large center-of-mass ernergies.

Contents

Chapter 1

Introduction

The intention of high energy physics is to understand and to describe the nature of particles and their interactions using mathematical methods. Three of the four known interactions and all experimentally detected particles have been embedded into the Standard Model (SM) [1–5]. The SM describes the particle interactions within the experimental errors. However, an important particle, predicted by the SM, has not yet been observed. This particle, the Higgs boson [6–10], is needed to generate the particle masses. Therefore, the main purpose of the present collider measurements at the Tevatron and that of the next generation, the LHC, is to discover the Higgs particle to complete the SM. The next step would be a precise measurement of the Higgs mass and its properties. A linear electron-positron collider would enhance the precision significantly.

The SM combines three known interactions. It can not describe gravity and does not explain the origin of its parameters. Using Supersymmetry [11–13] the SM can be embedded into unified theories that explain parts of the structure of the SM. The unification of the coupling constants, the naturalness problem and non-baryonic dark matter are examples of other problems that Supersymmetry could solve. The Minimal Supersymmetric Standard Model (MSSM) is considered in this thesis. Within the MSSM every SM particle is accompanied by a supersymmetric partner, whose spin differs by 1/2. Furthermore, a second Higgs doublet and the corresponding supersymmetric doublet have to be introduced.

The supersymmetric partners of the quarks and the gluon are the squarks and the gluino, respectively. Both couple strongly and it is expected to be discovered at the LHC, between 800 GeV and 2.5 TeV [14], depending on the scenario. The LHC has the advantage of providing high center-of-mass energies and, due to the initial hadrons, large cross sections for strongly interacting particles.

However, if the center-of-mass energy of a linear electron-positron collider is sufficient to produce a given particle, much more precise measurements of the masses can be performed. Additionally, the quantum numbers and couplings become accessible. The much higher precision of linear colliders originates in the exactly known center-of-mass energy and the clean scattering process.

In this thesis, the squark and gluino production at linear colliders is considered. The possible production channels of gluinos are pair production, associated production of squark, quark and gluino, and production channels with more than three particles in the final state. Since it is assumed that gluinos are heavier than 200 GeV, cross sections with more than three particles in the final state are likely to be suppressed. The NLO-SQCD corrections to squark-quark-gluino production in electron-positron annihilation were calculated in [15]. This process can be used to detect the gluino as well as to verify the supersymmetric coupling relations. If squarks are heavier than gluinos, gluino pair production [16–20] becomes accessible at smaller energies. Since the initial electrons of a linear collider couple only electro-weakly and gluinos only strongly, the production process starts at the one loop level. Due to squarks with large masses inside the loops, the cross section might be suppressed. However, the precision of a linear collider could compensate this disadvantage. Furthermore, measuring the angular distribution would allow a determination of the spin and point out the Majorana nature of the gluino [16]. Since different results for this process exist in the literature, gluino pair production will be recalculated and comparisons will be performed.

Besides electron-positron annihilation, a linear collider offers the possibility for other types of scattering processes. These are the $e^- e^-$ collision and the possibility of building a photon collider [21–27]. At a photon collider, laser light will be Compton-scattered on high energy electrons, and the backscattered photons will hold up to 85% of the initial electron energy [28, 29]. If this is realized for both beams, photon-photon scattering processes can be performed with high luminosity. Gluino pairs can be produced in photon-photon collisions, starting at the one loop level. The loops contain squarks and quarks, therefore the process depends on the gluino mass and the squark sector of the MSSM. Gluino pair production in photon-photon collisions is also calculated in this thesis.

Squark pair production in electron-positron annihilation has been studied intensively. The NLO QCD corrections were calculated in [30, 31], and the supersymmetric contributions were performed in [32, 33]. Susy-QCD corrections to squark decay and implications to precision measurements have been worked out in [34]. The corresponding process in photon-photon scattering occurs also at tree level, thus large cross sections comparable to the electron-positron annihilation are produced. The NLO-SQCD corrections to this process have been considered in [35]. A favorable property of squark production in photon-photon collision is the dependence on the final squark mass, at tree level. No other MSSM parameter enters the process. Then, e.g., it is possible to extract the mixing angle for the third generation from the squark decay. However, loop corrections will affect the squark pair production process. Since squarks also couple strongly, QCD corrections may become large. Because of the large number of diagrams the electroweak corrections might also become important. Therefore, the NLO-MSSM corrections to squark pair production in photon-photon collision will be calculated to study their influence on the cross section.

The outline of this thesis is as follows: in the next Chapter an introduction to the MSSM is presented. There the particle content as well as the MSSM parameter are discussed. Furthermore, in Section 2.5 renormalization of the squark sector is discussed, which is needed to calculate the one-loop corrections for squark pair production. The

appropriate counter terms of this production process are given in Section 2.5.4.

In Chapter 3, the general configuration of a scattering process at a linear collider is demonstrated. The laser-backscattering spectrum and luminosity of a photon collider are discussed. The Chapter is completed with the kinematic formulae for general hadronic process (Section 3.4) and a detailed overview of the developed computer calculation tools (Section 3.5).

In Chapter 4, the gluino pair production process in electron-positron annihilation is discussed. The Chapter is divided into Section 4.1, where the analytical results are denoted, and Section 4.2, where the numerical results are presented.

Chapter 5, deals with the gluino pair production process in photon-photon scattering where the high energy photons are produced by laser backscattering. While Section 5.1 discusses the direct scattering process, in Section 5.2 the resolved contribution of this process is given.

In Chapter 6 the squark pair production process in photon-photon collisions is investigated. Here, the tree level behavior is shown in Section 6.1 while in the following section the full next-to-leading order corrections are discussed. At the end of this Chapter the contributions from resolved squark pair production are considered.

A short conclusion of the three scattering processes is drawn in Chapter 7. Finally, one can find some used formulae and parameters in the appendix.

Chapter 2

Supersymmetry

2.1 The Standard Model

To describe the particles and their interactions, the principles of relativistic quantum field theory and symmetry relations based on symmetry groups are used. Besides gravity all known particles and their interactions can be embedded into the gauge group $SU(3)_C \times SU(2)_W \times U(1)_Y$ that consists of three unitary groups with three different coupling constants: g_s, g and g'. This is the underlying gauge group of the Standard Model (SM). The SM consists of the electroweak interaction [1–3] described by the product $SU(2)_W \times U(1)_Y$, and the strong interaction [4, 5], described by the group $SU(3)_C$. Up to now the SM is consistent with all experiments [36] apart from experimental evidence for mixing between the neutrinos [37–39], thus they are not massless. Although the left-handed neutrino masses are very small they can be generated by the seesaw machanism [40]. This can be embedded in a Grand Unified SO(10) theory where the MSSM as an effective theory and right-handed neutrinos with masses of $10^9 - 10^{15}$ GeV [41] remain. Throughout this thesis the neutrinos are assumed to be massless, therefore also no right-handed sneutrinos occur.

The matter fields of the SM are the fermions with spin quantum number 1/2. They are divided into leptons and quarks by the group $SU(3)_C$ where leptons are singlets and quarks are triplets under a gauge transformation of this group. Six types of leptons (e, μ, τ, $\nu_{\{e,\mu,\tau\}}$) and six flavors of quarks[1] (u, c, t, d, s, b) are known from experiments. They can be grouped into three generations of left-handed and right-handed particles.

$$\begin{pmatrix} \nu_{eL} \\ e_L \end{pmatrix}, \begin{pmatrix} \nu_{\mu L} \\ \mu_L \end{pmatrix}, \begin{pmatrix} \nu_{\tau L} \\ \tau_L \end{pmatrix}, e_R, \mu_R, \tau_R,$$

$$\begin{pmatrix} u_L \\ d_L \end{pmatrix}, \begin{pmatrix} c_L \\ s_L \end{pmatrix}, \begin{pmatrix} t_L \\ b_L \end{pmatrix}, u_R, c_R, t_R, d_R, s_R, b_R$$

The left-handed generations transform as doublets under a gauge transformation of the $SU(2)_W$ whereas the right-handed particles transform as singlets.

---

[1]The Cabibbo-Kobayashi-Maskawa-matrix (CKM) [42, 43] is set to unity in this thesis.

The interaction of the matter particles is mediated by gauge fields with spin 1, for the strong interaction the gluon fields and for the electroweak interaction the triplet fields $W_\mu^{1,2,3}$ and the singlet field B_μ.

If the symmetry were unbroken, all particles would be massless. A possible solution is the Higgs mechanism [6–10], where masses are generated in a gauge invariant way such that the renormalizibility of the theory is maintained. This mechanism postulates a spin 0 field with potential $V(\phi) = -\mu^2|\phi|^2 + \lambda/4|\phi|^2$. For a convenient choice of real and positive parameters λ and μ^2 the Higgs field self interaction leads to a finite vacuum expectation value that breaks the $SU(2)_W \times U(1)_Y$ symmetry. All fields that couple to the Higgs field will receive a mass. Unfortunately, the Higgs boson was not found so far, only a lower mass bound of 114.4 GeV is known with 95% confidence level from LEP experiments [44]. There is a small hint corresponding to a Higgs mass around 116 GeV.

The Standard Model can not explain all phenomena of particle interactions. This becomes evident e.g. at higher energies around the Planck scale. At this point gravitation will play an important role and one may expect that the gauge interactions unify with gravity to one general force. But the Standard Model does not include any gravitational forces.
Additionally there are other problems, where the Standard Model fails.

2.2 The Minimal Supersymmetric Extension of the SM

A model that could solve some of the known problems is supersymmetry [13]. It provides a symmetry between fermionic quantities and bosonic ones. Let the operator Q to be an anti-commuting spinor, which generates the transformation between bosonic and fermionic states

$$Q|\text{Boson} >= |\text{Fermion} >, \qquad Q|\text{Fermion} >= |\text{Boson} > .$$

In principle it is possible to introduce a system of N supersymmetries but for $N > 1$ no chiral interactions are allowed [45]. Therefore, this thesis restricts to the Minimal Supersymmetric Standard Model (MSSM) that is a $N = 1$ [11, 12] supersymmetric model with only soft breaking terms. For the MSSM each fermionic particle is accompanied by a bosonic particle and vice versa. Apart from the spin, the quantum numbers of the bosonic and the corresponding fermionic particles are identical.

2.2.1 Motivation for Supersymmetry

Theoretically there are no constraints that supersymmetry has to be realized at the electroweak scale rather than on higher scales. But its realization up to a few TeV has nice advantages. Below some examples are given how supersymmetry can solve some of the known problems of the SM.

- Coupling unification: If one believes in grad unification theories one would expect that the three coupling constants would unify at a high scale $\mathcal{O}(10^{16})$GeV to one

general coupling. This can be tested by evaluating the three coupling constants to higher energies using 2-loop renormalization group equation [46–48]. In the SM the three couplings will not unify at high energies in one point. Whereas, for the MSSM the running is affected by Susy-loop contributions [49–52]. This leads to a unification at one point for $M_{GUT} \approx 2 \cdot 10^{16}$ GeV if the breaking scale is around 1 TeV or one order of magnitude higher or lower [53, 54].

- A serious problem in Standard Model is the naturalness problem, see [45, 55–59]. As a result of the Higgs mechanism, a massive scalar Higgs boson occurs with the mass proportional to the electroweak scale $\Lambda_W = \mathcal{O}(100$ GeV$)$. Due to loops of other particles, that couple directly or indirectly to the Higgs field, the Higgs mass receives huge virtual corrections. These corrections are proportional to the square of the ultraviolet momentum cutoff that is used to regularize the loop integral. At this scale, usually the Planck scale or the unification scale of the coupling constants, new physics should enter into the theory. The problem is that the quantum corrections, different from fermions and gauge bosons, are around 30 orders of magnitude larger than the Higgs mass itself of $m_H^2 = (100$ GeV$)^2$. Thus the bare Higgs mass and the Higgs counter term are much larger than m_H^2 and have to be fine-tuned at each order of perturbation theory to obtain a Higgs mass at the electroweak scale. It seems unnatural that the mass of the Higgs boson is so light and not of the order of the cutoff scale.
  In supersymmetric theories the large contributions cancel with the corresponding contributions of the superpartners if the masses of the supersymmetric particles are not too high. Therefore, one believes that supersymmetry is realized at the electroweak scale up to a few TeV.

- From measurements of the rotation of the galaxies one obtains that the universe matter consists mainly of "dark matter" (around 90%). The dominant non-baryonic part could possibly be explained by a stable supersymmetric particle [60]. A candidate for this lightest supersymmetric particle (LSP), that means that it does not decay into Standard Model particles, could be the neutralino $\tilde{\chi}^0$. A LSP is obtained in supersymmetry if one forbids baryon and lepton number violating terms in the lagrangian by imposing R-parity conservation. R-parity is an additional symmetry where the eigenvalues of the Standard Model particles are equal to $+1$ and -1 for their supersymmetric partners. It is defined as

$$R = (-1)^{3(B-L)+2s} ,$$

where B and L are baryon and lepton number and s is the spin of the particle. As a consequence of R-parity conservation sparticles at collider experiments can only be produced in pairs.

- Furthermore one can consider Supersymmetry as a local symmetry. It turns out that the algebra of General Relativiy, the Lorentz-algebra, is part of such a symmetry. One obtains a connection between internal gauge symmetries and gravity, leading to the construction of Supergravity [61–63]. This would be the first step of a unification of the strong and electroweak interaction with gravity to one fundamental force.

Super-field	Boson-field	Fermion-field	$(SU(3)_C,$ $SU(2)_W, U(1)_Y)$	Name
Matter fields				
$\hat{L} = \{\tilde{L}, L\}$	$\begin{pmatrix} \tilde{\nu}_L \\ \tilde{e}_L \end{pmatrix}$	$\begin{pmatrix} \nu_L \\ e_L \end{pmatrix}$	(1, 2, -1)	{sleptonen, leptonen}
$\hat{E} = \{\tilde{E}, E\}$	$\tilde{e}_R^*$	e_R	(1, 1, 2)	
$\hat{Q} = \{\tilde{Q}, Q\}$	$\begin{pmatrix} \tilde{u}_L \\ \tilde{d}_L \end{pmatrix}$	$\begin{pmatrix} u_L \\ d_L \end{pmatrix}$	(3, 2, $\frac{1}{3}$)	{squarks, quarks}
$\hat{U} = \{\tilde{U}, U\}$	$\tilde{u}_R^*$	u_R	$(3^*, 1, -\frac{4}{3})$	
$\hat{D} = \{\tilde{D}, D\}$	$\tilde{d}_R^*$	d_R	$(3^*, 1, \frac{2}{3})$	
Gauge fields				
V'	B_μ	λ'	(1, 1, 0)	{B_μ-boson, bino}
V^a	W_μ^a	λ^a	(1, 3, 0)	{W_μ^a-bosonen, winos}
V_s^a	G_μ^a	λ_s^a	(8, 1, 0)	{gluonen, gluinos}
Higgs fields				
$\hat{H}_1 = \{H_1, \tilde{H}_1\}$	$\begin{pmatrix} H_1^1 \\ H_1^2 \end{pmatrix}$	$\begin{pmatrix} \tilde{H}_1^1 \\ \tilde{H}_1^2 \end{pmatrix}$	(1, 2, -1)	{Higgs− bosonen, higgsinos}
$\hat{H}_2 = \{H_2, \tilde{H}_2\}$	$\begin{pmatrix} H_2^1 \\ H_2^2 \end{pmatrix}$	$\begin{pmatrix} \tilde{H}_2^1 \\ \tilde{H}_2^2 \end{pmatrix}$	(1, 2, 1)	

Table 2.1: The field content and quantum numbers of the MSSM. For quarks, leptons and their supersymmetric partners only the first generation is indicated.

2.2.2 Lagrangian of the MSSM

To construct the MSSM one extends the SM to a minimal number of particles [64–66], necessary to obtain a supersymmetric theory. This particle content with quantum numbers is given in Table 2.1.

Each fermion obtains a scalar partner combined in a chiral multiplet. Only the first generation of fermions are shown in Table 2.1. The gauge bosons and the gluon are accompanied by the spin-1/2 gauginos and gluinos. They compose a vector multiplet. The Standard Model Higgs boson obtains a spin-1/2 partner, the higgsino. Contrary to the SM, a second Higgs-doublet has been introduced, because Yukawa couplings are forbidden that involve conjugated Higgs fields. A second reason is that the sum of all hyper-charges has to vanish for anomaly-cancellation, which would not be fulfilled for only one Higgs doublet. The fermions with isospin $-1/2$ receive their masses from the doublet H_1 and the fermions with isospin $1/2$ from H_2.

The supersymmetric part of the lagrangian of the MSSM is given as

$$\mathcal{L}_{Susy} = + \int d^2\theta \left(\frac{1}{16g^2} W^{a\alpha} W^a_\alpha + \frac{1}{16g'^2} W'^\alpha W'_\alpha + \frac{1}{16g_s^2} W_s^{a\alpha} W^a_{s\alpha} + h.c. \right)$$

$$+ \int d^2\theta d^2\bar{\theta} \left(\hat{\bar{Q}} e^{g'YV'+2gT^aV^a+2g_sV_s} \hat{Q} \right.$$

$$+ \hat{\bar{U}} e^{g'YV'+2gT^aV^a+2g_sV_s} \hat{U} + \hat{\bar{D}} e^{g'YV'+2gT^aV^a+2g_sV_s} \hat{D}$$

$$+ \hat{\bar{L}} e^{g'YV'+2gT^aV^a} \hat{L} + \hat{\bar{E}} e^{g'YV'+2gT^aV^a} \hat{E}$$

$$\left. + \hat{\bar{H}}_1 e^{g'YV'+2gT^aV^a} \hat{H}_1 + \hat{\bar{H}}_2 e^{g'YV'+2gT^aV^a} \hat{H}_2 \right)$$

$$+ \int d^2\theta \left(\epsilon_{ij} \left[\lambda_d \hat{H}_1^i \hat{Q}^j \hat{D} - \lambda_u \hat{H}_2^i \hat{Q}^j \hat{U} + \lambda_e \hat{H}_1^i \hat{L}^j \hat{E} - \mu \hat{H}_1^i \hat{H}_2^j \right] + h.c. \right), \quad (2.1)$$

where $V_s = V_s^a \frac{\lambda^a}{2}$. The first line of equation (2.1) denotes the kinetic term of the vector super-fields with field tensors

$$W_{s\alpha}^a = -\frac{1}{4} \bar{D}\bar{D} \left(e^{2g_s V_s} D_\alpha e^{2g_s V_s} \right), \qquad W_\alpha^a = -\frac{1}{4} \bar{D}\bar{D} \left(e^{2gV} D_\alpha e^{2gV} \right),$$

$$W'_\alpha = -\frac{1}{4} \bar{D}\bar{D} \left(e^{2g'V'} D_\alpha e^{2g'V'} \right),$$

where the covariant derivatives are $D_\alpha = \partial_\alpha - i_\alpha (\sigma_\mu \bar{\theta}) \partial^\mu$ and $\bar{D}_{\dot{\alpha}} = \bar{\partial}_{\dot{\alpha}} + i(\theta\sigma_\mu)_{\dot{\alpha}} \partial^\mu$ with $\alpha, \dot{\alpha}$ Weyl-spinor indices and σ the Pauli matrices. The second to the fifth line in equation (2.1) show the kinetic and gauge interaction terms of the fermions and their superpartners. The last line of equation (2.1) denotes the superpotential. It contains the Yukawa couplings λ_u, λ_d and λ_e of the Higgs bosons to the matter fields, which in case of three generations are arbitrary complex 3×3 matrices in generation space. Baryon and lepton number violating terms are forbidden by imposing R-parity conservation.

In the MSSM, supersymmetry is softly broken by explicit breaking terms. Soft breaking means that only terms are introduced which do not lead to new quadratic divergences. These terms were worked out by [67], and the soft breaking lagrangian reads

$$\mathcal{L}_{Soft} = + \frac{1}{2} \left(M_1 \lambda' \lambda' + M_2 \lambda^a \lambda^a + M_3 \lambda_s^a \lambda_s^a + h.c. \right)$$

$$- M_{\tilde{q}_L}^2 |\tilde{q}_L|^2 - M_{\tilde{u}_R}^2 |\tilde{u}_R|^2 - M_{\tilde{d}_R}^2 |\tilde{d}_R|^2 - M_{\tilde{l}_L}^2 |\tilde{l}_L|^2 - M_{\tilde{e}_R}^2 |\tilde{e}_R|^2$$

$$- m_1^2 |H_1|^2 - m_2^2 |H_2|^2 + (m_3^2 \epsilon_{ij} H_1^i H_2^j + h.c.)$$

$$- \epsilon_{ij} \left(\lambda_u A_u H_2^i \tilde{Q}^j \tilde{U} + \lambda_d A_d H_1^i \tilde{Q}^j \tilde{D} + \lambda_e A_e H_1^i \tilde{L}^j \tilde{E} + h.c. \right),$$

where the sfermion breaking parameters $M_{\tilde{q}_L}^2$, $M_{\tilde{u}_R}^2$, $M_{\tilde{d}_R}^2$, $M_{\tilde{l}_L}^2$ and $M_{\tilde{e}_R}^2$ are general hermitian 3x3 matrices. The trilinear couplings A_u, A_d, A_e are complex 3x3 matrices. For the quantization of the lagrangian, see e.g. [68, 69], one also has to add the ghost term and the gauge fixing term. A full on-shell lagrangian of the MSSM can be found e.g. in [70].

2.3   Particle mass spectrum of the MSSM

2.3.1   Higgs Sector

The Higgs superfields (Table 2.1) contain two Higgs doublets H_1 and H_2 with opposite hypercharge $Y_1 = -1$ and $Y_2 = 1$, respectively. Both doublets have a non-vanishing vacuum expectation value

$$H_{1vac} = \begin{pmatrix} v_1 \\ 0 \end{pmatrix}, \qquad H_{2vac} = \begin{pmatrix} 0 \\ v_2 \end{pmatrix}.$$

Their general structure is given as

$$H_1 = \begin{pmatrix} v_1 + \frac{1}{\sqrt{2}}(\phi_1^0 - i\chi_1^0) \\ -\phi_1^- \end{pmatrix}, \qquad H_2 = \begin{pmatrix} \phi_1^+ \\ v_2 + \frac{1}{\sqrt{2}}(\phi_2^0 + i\chi_2^0) \end{pmatrix}.$$

The ratio of the vacuum expectation values defines

$$\tan\beta = \frac{v_2}{v_1} \qquad \text{with} \qquad 0 < \beta < \frac{\pi}{2}.$$

There are four non-diagonal mass matrices, one for the χ fields, one for the neutral ϕ fields, and two for the charged ϕ fields. They can be diagonalized with appropriate transformations

$$\begin{pmatrix} G^0 \\ A^0 \end{pmatrix} = \begin{pmatrix} \cos\beta & \sin\beta \\ -\sin\beta & \cos\beta \end{pmatrix} \begin{pmatrix} \chi_1^0 \\ \chi_2^0 \end{pmatrix},$$

$$\begin{pmatrix} G^\pm \\ H^\pm \end{pmatrix} = \begin{pmatrix} \cos\beta & \sin\beta \\ -\sin\beta & \cos\beta \end{pmatrix} \begin{pmatrix} \phi_1^\pm \\ \phi_2^\pm \end{pmatrix},$$

$$\begin{pmatrix} H^0 \\ h^0 \end{pmatrix} = \begin{pmatrix} \cos\alpha & \sin\alpha \\ -\sin\alpha & \cos\alpha \end{pmatrix} \begin{pmatrix} \phi_1^0 \\ \phi_2^0 \end{pmatrix}, \tag{2.2}$$

where the mixing angle α ist defined by the relation

$$\tan 2\alpha = \tan 2\beta \frac{M_{A^0}^2 + M_Z^2}{M_{A^0}^2 - M_Z^2} \qquad \text{with} \qquad -\frac{\pi}{2} < \alpha < 0.$$

The three fields G^0 and $G^\pm$ in equation (2.2) are unphysical Goldstone bosons. Their masses in the 't Hooft-Feynman-gauge is $m_{G^0} = M_Z$ and $m_{G^\pm} = M_W$. The other 5 fields are physical Higgs bosons $(A^0, H^\pm, H^0, h^0)$ with tree level masses

$$M_{A^0}^2 = m_3^2 (\tan\beta + \cot\beta),$$

$$M_{H^\pm}^2 = M_{A^0}^2 + M_W^2,$$

$$M_{H^0,h^0}^2 = \frac{1}{2}\left(M_{A^0}^2 + M_Z^2 \pm \sqrt{(M_{A^0}^2 + M_Z^2)^2 - 4M_Z^2 M_{A^0}^2 \cos^2 2\beta}\right).$$

2.3.2 Vector Bosons

The part of the lagrangian where the vector bosons receive their masses is

$$\mathcal{L} = (D_\mu H_1)^\dagger D^\mu H_1 + (D_\mu H_2)^\dagger D^\mu H_2$$

with the covariant derivation:

$$D_\mu = \partial_\mu + igT^a W_\mu^a + ig'\frac{Y}{2}B_\mu.$$

The weak isospin T^a are the generators of the gauge group $SU(2)$ with $T^a = \sigma^a/2$ for isospin dublets and $T = 0$ for isospin singlets.

The gauge fields W_μ^i with $i = 1, 2, 3$ and B_μ transform into the physical fields as

$$W_\mu^\pm = \frac{1}{\sqrt{2}}(W_\mu^1 \mp iW_\mu^2), \qquad \begin{pmatrix} Z_\mu \\ A_\mu \end{pmatrix} = \begin{pmatrix} c_W & -s_W \\ s_W & c_W \end{pmatrix}\begin{pmatrix} W_\mu^3 \\ B_\mu \end{pmatrix},$$

where $c_W = \cos\theta_W$ and $s_W = \sin\theta_W$ and θ_W is the weak mixing angle with $\theta_W = g'/g$. The electrical charge Q is related to the third component of the weak isospin and the hypercharge by $Q = T^3 + Y/2$ and it is $g = e/s_W$ and $g' = e/c_W$. The masses of the vector bosons (the charged W-bosons, the neutral Z-boson and the neutral photon γ) are given as

$$M_W = \frac{g}{\sqrt{2}}\sqrt{v_1^2 + v_2^2}, \qquad M_Z = \frac{g}{\sqrt{2}\,c_W}\sqrt{v_1^2 + v_2^2}, \qquad M_\gamma = 0.$$

The weak mixing angle θ_W can be re-expressed in terms of the W- and Z-boson masses

$$c_W = \frac{g}{\sqrt{g^2 + g'^2}} = \frac{M_W}{M_Z}, \qquad s_W = \frac{g'}{\sqrt{g^2 + g'^2}} = \sqrt{1 - \frac{M_W^2}{M_Z^2}}. \qquad (2.3)$$

2.3.3 Charginos

The superpartners of the W-bosons are the winos $\tilde{W}^\pm$ and the superpartners of the Higgs boson the higgsinos. The fields of the winos and the charged higgsinos are defined through

$$\tilde{W}^+ = \begin{pmatrix} -i\lambda^+ \\ i\bar{\lambda}^- \end{pmatrix}, \quad \tilde{W}^- = \begin{pmatrix} -i\lambda^- \\ i\bar{\lambda}^+ \end{pmatrix}, \quad \tilde{H}_1^+ = \begin{pmatrix} \tilde{H}_2^1 \\ \bar{\tilde{H}}_1^2 \end{pmatrix}, \quad \tilde{H}_2^+ = \begin{pmatrix} \tilde{H}_2^2 \\ \bar{\tilde{H}}_2^1 \end{pmatrix},$$

where $\lambda^\pm = \frac{1}{\sqrt{2}}(\lambda^1 \mp i\lambda^2)$. The winos and higgsinos mix to four-component Dirac-spinors, called charginos $\chi_i^\pm (i = 1, 2)$. With the spinors $\psi_L^T = (-i\lambda^+, \tilde{H}_2^2)^T$ and $\psi_R^T = (-i\lambda^-, \tilde{H}_1^2)^T$ the corresponding mass term in the lagrangian can be written as

$$\mathcal{L}_{m_{\tilde{\chi}^\pm}} = -\frac{1}{2}\left(\psi_L^T, \psi_R^T\right)\begin{pmatrix} 0 & X^T \\ X & 0 \end{pmatrix}\begin{pmatrix} \psi_L \\ \psi_R \end{pmatrix} + h.c.$$

with the mass matrix

$$X = \begin{pmatrix} M_2 & \sqrt{2}M_W \sin\beta \\ \sqrt{2}M_W \cos\beta & \mu \end{pmatrix}. \tag{2.4}$$

The matrix (2.4) is diagonalized and the fields are transformed by two unitary 2×2 matrices U, V as follows

$$U^* X V^\dagger = \begin{pmatrix} m_{\tilde{\chi}_1^\pm} & 0 \\ 0 & m_{\tilde{\chi}_2^\pm} \end{pmatrix}, \qquad \chi_i^+ = V_{ij}\psi_j^+, \quad \chi_i^- = U_{ij}\psi_j^-.$$

Then, in the Dirac bases the charginos mass eigenstates are defined as

$$\tilde{\chi}_1^+ = \begin{pmatrix} \chi_1^+ \\ \bar{\chi}_1^- \end{pmatrix}, \quad \text{and} \quad \tilde{\chi}_2^+ = \begin{pmatrix} \chi_2^+ \\ \bar{\chi}_2^- \end{pmatrix}.$$

2.3.4 Neutralinos

The charged higgsinos and gauginos have mixed to the charginos. Also the neutral higgsinos, the $\tilde{H}_1^0$, $\tilde{H}_2^0$, and the neutral gauginos, the photino $\tilde{A}$ and the zino $\tilde{Z}$, will mix. If $\lambda_A = c_W\lambda' + s_W\lambda^3$ and $\lambda_Z = -s_W\lambda' + c_W\lambda^3$ are the two-component spinors of the photino and zino, respectively, the fields become

$$\tilde{H}_1^0 = \begin{pmatrix} \tilde{H}_1^1 \\ \bar{\tilde{H}}_1^1 \end{pmatrix}, \quad \tilde{H}_2^0 = \begin{pmatrix} \tilde{H}_2^2 \\ \bar{\tilde{H}}_2^2 \end{pmatrix}, \quad \tilde{A} = \begin{pmatrix} -i\lambda_A \\ i\bar{\lambda}_A \end{pmatrix}, \quad \tilde{Z} = \begin{pmatrix} -i\lambda_Z \\ i\bar{\lambda}_Z \end{pmatrix}.$$

The neutralino mass term in the lagrangian is given by the contributions from gauge interaction, the super potential and soft breaking terms. The relevant terms can be written by use of the vector $\psi_0^T = (-i\lambda_A, -i\lambda_Z, \tilde{H}_1^1, \tilde{H}_2^2)$ as

$$\mathcal{L}_{m_{\tilde{\chi}^0}} = -\frac{1}{2}\psi_0^T Y' \psi_0 + h.c.$$

and the symmetric mass matrix

$$Y' = \begin{pmatrix} c_W^2 M_1 + s_W^2 M_2 & -c_W s_W(M_1 - M_2) & 0 & 0 \\ -c_W s_W(M_1 - M_2) & s_W^2 M_1 + c_W^2 M_2 & M_Z\cos\beta & -M_Z\sin\beta \\ 0 & M_Z\cos\beta & 0 & \mu \\ 0 & -M_Z\sin\beta & -\mu & 0 \end{pmatrix}.$$

The neutralino mass matrix Y' can be diagonalized by one unitary 4×4 matrix N'

$$N'^* Y' N'^{-1} = \text{diag}(m_{\chi_1^0}, m_{\chi_2^0}, m_{\chi_3^0}, m_{\chi_4^0}) \ .$$

The neutralinos are four-component Majorana spinors $\tilde{\chi}_i^0$ with

$$\tilde{\chi}_i^0 = \begin{pmatrix} \chi_i^0 \\ \bar{\chi}_i^0 \end{pmatrix} \quad \text{with} \quad \chi_i^0 = N_{ij}\psi_{0j}, \qquad i,j = 1,2,3,4.$$

2.3.5 Gluinos

The gluino is the superpartner of the SM gluon. Therefore, eight gluinos exist corresponding to the eight linear independent $SU(3)_C$ generators. Gluinos are neutral with spin 1/2 and therefore Majorana fermions. They do not mix with other particles because they take part only at strong interactions. The mass term in the lagrangian is

$$\mathcal{L}_{\text{soft}} = \frac{1}{2} M_3 \lambda_s^a \lambda_s^a + h.c. \ ,$$

thus, the gluinos are mass eigenstates and directly related to the soft breaking parameter M_3 ($M_3 \in \mathcal{R}$)

$$m_{\tilde{g}} = |M_3|.$$

2.3.6 Sfermions

The mass term of the sfermion fields in the lagrangian reads

$$\mathcal{L}_{m_{\tilde{f}}} = - \left(\tilde{f}_L^*, \ \tilde{f}_R^* \right) M_{\tilde{f}}^2 \left(\begin{matrix} \tilde{f}_L \\ \tilde{f}_R \end{matrix} \right),$$

with the sfermion fields $\tilde{f}$ and the anti-sfermion field $\tilde{f}^*$. The mass matrix is given as

$$M_{\tilde{f}}^2 = \left(\begin{matrix} M_{\tilde{f}_L}^2 + M_Z^2 \cos 2\beta \, (I_3^f - e_f s_W^2) + m_f^2 & m_f(A_f^* - \mu\{\cot\beta, \tan\beta\}) \\ m_f(A_f - \mu^*\{\cot\beta, \tan\beta\}) & M_{\tilde{f}_R}^2 + M_Z^2 \cos 2\beta \, e_f s_W^2 + m_f^2 \end{matrix} \right). \quad (2.5)$$

where $\cot\beta$ holds for sneutrinos and up-type squarks and $\tan\beta$ for the other sfermions. Generally these matrices are non-diagonal. Each left- and right-handed superpartners of a fermion field have the same $SU(3)_C$ quantum numbers and the same charge. Because the $SU(2)_W \times U(1)_Y$ symmetry is broken these field can mix into mass eigenstates $\tilde{f}_1$ and $\tilde{f}_2$. The mass matrix (2.5) can be diagonalized with an unitary matrix $U_{\tilde{f}}$

$$D_{\tilde{f}} = U_{\tilde{f}} M_{\tilde{f}}^2 U_{\tilde{f}}^\dagger = \left(\begin{matrix} m_{\tilde{f}_1}^2 & 0 \\ 0 & m_{\tilde{f}_2}^2 \end{matrix} \right), \qquad \text{with} \quad U_{\tilde{f}} = \left(\begin{matrix} U_{\tilde{f}_{11}} & U_{\tilde{f}_{12}} \\ U_{\tilde{f}_{21}} & U_{\tilde{f}_{22}} \end{matrix} \right). \quad (2.6)$$

In case of real parameters A_f and μ the mixing matrix can be expressed in terms of a real mixing angle $\theta_{\tilde{f}}$ as

$$U_{\tilde{f}} = \left(\begin{matrix} \cos\theta_{\tilde{f}} & \sin\theta_{\tilde{f}} \\ -\sin\theta_{\tilde{f}} & \cos\theta_{\tilde{f}} \end{matrix} \right) = \left(\begin{matrix} c_{\theta_{\tilde{f}}} & s_{\theta_{\tilde{f}}} \\ -s_{\theta_{\tilde{f}}} & c_{\theta_{\tilde{f}}} \end{matrix} \right). \quad (2.7)$$

The left and right handed sfermion fields transform into the mass eigenstates by

$$\left(\begin{matrix} \tilde{f}_1 \\ \tilde{f}_2 \end{matrix} \right) = U_{\tilde{f}} \left(\begin{matrix} \tilde{f}_L \\ \tilde{f}_R \end{matrix} \right), \quad \text{and} \quad \left(\begin{matrix} \tilde{f}_L \\ \tilde{f}_R \end{matrix} \right) = U_{\tilde{f}}^\dagger \left(\begin{matrix} \tilde{f}_1 \\ \tilde{f}_2 \end{matrix} \right).$$

The squared masses of the sfermion mass eigenstates can be expressed as

$$m^2_{\tilde{f}_{1,2}} = \frac{1}{2}(M^2_{\tilde{f}_L} + M^2_{\tilde{f}_R}) + \frac{1}{2}M^2_Z c_{2\beta} T^3_f + m^2_f$$
$$\pm \frac{1}{2}\sqrt{\left(M^2_{\tilde{f}_L} - M^2_{\tilde{f}_R} + M^2_Z c_{2\beta}\left(T^3_f - 2e_f s^2_W\right)\right)^2 + 4m^2_f\left(A_f - \mu^*\{\cot\beta, \tan\beta\}\right)^2} \quad (2.8)$$

with the abbreviation $c_{2\beta} = \cos 2\beta$. Here $+$ holds for sfermions $\tilde{f}_1$ and $-$ for sfermions $\tilde{f}_2$. The squark mixing angle can be expressed as

$$\tan 2\theta_{\tilde{q}} = \frac{2m_q\left(A_f - \mu^*\{\cot\beta, \tan\beta\}\right)}{M^2_{\tilde{f}_L} - M^2_{\tilde{f}_R} + M^2_Z \cos 2\beta\left(I^f_3 - 2e_f s^2_W\right)}. \quad (2.9)$$

2.4   Parameters of the MSSM

If no unification theory is assumed, the MSSM contains of a large number of parameters. They can be grouped into parameters of the Standard Model, parameters of the Higgs sector and soft Susy breaking parameters.

The Standard Model parameters are the 12 fermion masses m_f, 2 gauge boson masses M_W, M_Z and 3 coupling constants g_s, g, g'. The CKM matrix [42, 43] was set to unity. The fermion masses are

$$m_{\nu_e} = 0 \text{ GeV}, \quad m_e = 0.51099907 \text{ MeV}, \quad m_u = 53.8 \text{ MeV}, \quad m_d = 53.8 \text{ MeV},$$
$$m_{\nu_\mu} = 0 \text{ GeV}, \quad m_\mu = 0.105658389 \text{ GeV}, \quad m_c = 1.5 \text{ GeV}, \quad m_s = 0.15 \text{ GeV},$$
$$m_{\nu_\tau} = 0 \text{ GeV}, \quad m_\tau = 1.777 \text{ GeV}, \quad m_t = 174.3 \text{ GeV}, \quad m_b = 4.5 \text{ GeV}.$$

The light quark masses are effective parameters [71, 72]. The masses of the gauge bosons are $M_W = 80.451$ GeV and $M_Z = 91.1875$ GeV. Instead of the gauge couplings g_s, g, g', the parameters α_s, α and $\sin^2\theta_W$ are used. If not indicated otherwise an effective $\alpha(m_Z) = 1/127.934$ is used. The weak mixing angle is fixed by the tree level relation $s^2_W = 1 - \frac{M^2_W}{M^2_Z}$.

The strong coupling constant α_s is evaluated at a typical scale of the considered process. In case of the gluino pair production the gluino mass, and in case of squark pair production the final squark mass is used. The strong coupling α_s is calculated with the α_s-routine of the CERN PDFLIB version 8.04 [73] and an implemented routine for the formulas of [74], where agreement among them was found. The following parameters are used to determine α_s

$$\Lambda^{n_f=5}_{LO} = 83.76 \text{ MeV}, \qquad \text{TMAS} = 174.3 \text{ GeV},$$

leading to an $\alpha_s(m_{Z^0}) = 0.1172$.

The free parameters of the Higgs sector are the Higgs boson mass M_A, the ratio of the vacuum expectation value $\tan\beta = v_1/v_2$ and the mixing parameter μ.

The Susy breaking parameters consist of the 3 parameters (M_1, M_2, M_3) for the supersymmetric partners of the bosons. Since mixing between the generations is neglected,

there are 24 parameters for the sfermions. These are 15 left- and right-handed break-ing parameters $M^2_{\tilde{q}_L}$, $M^2_{\tilde{u}_R}$, $M^2_{\tilde{d}_R}$, $M^2_{\tilde{l}_L}$, $M^2_{\tilde{e}_R}$ where $\tilde{q}$ denotes all flavors of squarks, $\tilde{u}$ the up-type and $\tilde{d}$ the down-type squarks, $\tilde{l}$ all leptons and $\tilde{e} = \{\tilde{e}, \tilde{\mu}, \tilde{\tau}\}$. The other 9 parameters are the trilinear couplings A_u, A_d, A_e.

In general M_1, M_2, M_3, μ, A_u, A_d, A_e are complex, but for this thesis they are assumed to be real. Therefore, CP invariance holds and the diagonalization matrices $U_{\tilde{f}}$ of equation (2.7) are real. Since mixing effects for the first two generations of sfermions are always small, all mixing angles of these generations are fixed to 0.

Mass Constraints

The gluino pair production in electron-positron and photon-photon collisions depends on the gluino mass and the squark masses and mixing angles. The following limits have been used: as mass limit for the gluino $m_{\tilde{g}} \geq 200$ GeV is used, taken from the CDF [75] and D0 [76] searches in jets with missing energy channels, relevant for non-mixing squark masses of $m_{\tilde{q}} \geq 325$ GeV and $\tan\beta = 3$. A possible gluino with light mass [77] is not considered. For the third generation squark the CERN LEP limits on the light top and bottom squark masses, $m_{\tilde{t}_1} \geq 100$ GeV and $m_{\tilde{b}_1} \geq 99$ GeV [78] have been taken. Furthermore, it was ensured that the Susy one-loop contributions [79–81] to the ρ-parameter are $\rho_{\text{Susy}} < 0.0035$ [77]. The squark masses depend directly only slightly on $\tan\beta$. Therefore, a fixed value of $\tan\beta = 10$ has been used.

The NLO corrections to the squark pair production depend on too many parameters, as all can be varied. Therefore, the corrections are demonstrated at the two parameter points SPS1 and SPS5, Appendix B.

2.5 Renormalization

2.5.1 Regularization

Calculating higher order matrix elements, one encounters loop integrals, which contain integrations over the loop momentum. Depending on the particles and number of propagators inside the loop, these integrals diverge. To handle these divergences one has to regularize them. A widely used method in non-supersymmetric gauge theories is the dimensional regularization (DREG) [82–84]. In DREG, the space-time dimension and the dimensionality of fields are extended from 4 to $D = 4 - \epsilon$. All loop integrals will converge for sufficiently small D and one can divide the integral into a part that remains finite for $\epsilon \to 0$ respectively $D \to 4$, and one that diverges like $(1/\epsilon^n)$. To get rid of the divergences one has to renormalize the theory.
In supersymmetry it is required that the number of degrees of freedom for fermions and bosons are equal in each super-multiplet. Using DREG this equivalence will be destroyed leading to a violation of supersymmetry and will spoil the Slavnov-Taylor identities. However, one can use DREG and restore the Slavnov-Taylor identities adding appropriate counterterms [85, 86].
A more comfortable calculation procedure is the method of dimensional reduction (DRED)[87–89]. In DRED the dimension of space-time is continued to $D = 4 - \epsilon$,

whereas the fields remain unchanged. Thus the Dirac algebra is performed in four dimensions while the loop integrals are performed in D dimensions. Then, counterterms are only necessary to cancel the UV divergences. The nice feature of DRED is that it preserves gauge symmetry and supersymmetry. Unfortunately, there is also an ambiguity in the treatment of the antisymmetric Levi-Civita tensor [90], that exactly speaking D must be an integer with $D \leq 4$ and there is no continuous transition to $D = 4$. However, it was shown by [87, 88] that for simple cases DR preserves supersymmetry.

At the tree level squark pair production in photon-photon collisions only gauge-boson-sfermion-sfermion couplings occur. Therefore, using DREG no supersymmetry restoring counterterms are necessary. In this thesis all calculations have been performed using DREG and DRED.

2.5.2 Renormalization Procedure

Through the regularization procedure unphysical parameters have been introduced that have to be removed by renormalization. Using multiplicative renormalization, in the bare lagrangian the bare parameters (g_0, ...) and fields (Φ_0, ...) are replaced by renormalized ones ($g, \Phi, ...$), e.g.:

$$g_0 = Z_g\, g = (1 + \delta Z_g)g = g + \delta g \;, \qquad \Phi_0 = Z_\Phi^{\frac{1}{2}}\Phi = (1 + \frac{1}{2}\,\delta Z_\Phi)\Phi,$$

where δg and δZ_Φ are the counter terms. With these replacements, the bare lagrangian splits into a renormalized part and a counterterm part

$$\mathcal{L}(g_0, \Phi_0) = \mathcal{L}(g, \Phi) + \mathcal{L}(g, \delta g, \Phi, \delta Z_\Phi \Phi).$$

Applying appropriate renormalization conditions, it fixes the counterterms and determines the physical meaning of the renormalized parameters.

Different renormalization schemes are available. A scheme used in QCD is the "Minimal Subtraction scheme" (MS) [91, 92]. After renormalization, the parameters will depend on an arbitrary scale μ.

In electroweak theories the on-shell scheme [93] can be used. Here the Thomson scattering sets a natural scale for $e = \sqrt{4\pi\alpha}$, and for stable particles the masses are well-defined and can be used as input parameters. For a review of the electroweak Standard Model see [94] and for the renormalization of the MSSM [95]. In this thesis the on-shell scheme is used.

2.5.3 Renormalization of the Squark Sector

The renormalization of the squark sector, that determines the squark mass counter term and squark wave function Z-factor, is taken from [96, 97]. In this section "f" always stands for "{u,d}" and "i" for "{1,2}".

The Lagrangian of the squark sector is given as

$$\mathcal{L}_m = \left(\tilde{f}_L^*, \tilde{f}_R^* \right) k^2 \begin{pmatrix} \tilde{f}_L \\ \tilde{f}_R \end{pmatrix} - \left(\tilde{f}_L^*, \tilde{f}_R^* \right) M_{\tilde{f}}^2 \begin{pmatrix} \tilde{f}_L \\ \tilde{f}_R \end{pmatrix},$$

where the mass matrix is defined in equation (2.5). To renormalize the squark sector the parameters and fields have to be replaced by renormalized ones.

$$M_{\tilde{f}}^2 \rightarrow M_{\tilde{f}}^2 + \delta M_{\tilde{f}}^2 \quad \text{and} \quad \begin{pmatrix} \tilde{f}_L \\ \tilde{f}_R \end{pmatrix} \rightarrow \left(\mathbb{1} + \frac{1}{2} \delta Z_{\tilde{f}} \right) \begin{pmatrix} \tilde{f}_L \\ \tilde{f}_R \end{pmatrix},$$

where the field renormalization matrix is diagonal: $\delta Z_{\tilde{f}} = \text{diag}\{ \delta Z_L^{\tilde{f}}, \delta Z_R^{\tilde{f}} \}$.

To transform the squark states of the left-right basis to the basis of the mass eigenvalues a mixing matrix $R_{\tilde{f}}$ is introduced

$$\begin{pmatrix} \tilde{f}_1 \\ \tilde{f}_2 \end{pmatrix} = R_{\tilde{f}} \begin{pmatrix} \tilde{f}_L \\ \tilde{f}_R \end{pmatrix}, \qquad R_{\tilde{f}} = \left(\mathbb{1} + \frac{1}{2} \delta Z_{U_{\tilde{f}}} \right) U_{\tilde{f}}. \tag{2.10}$$

The unitary matrix $U_{\tilde{f}}$ diagonalizes the squark mass matrix as given in equation (2.6). The Z-factor in equation (2.10) does not absorb divergences, it describes the deviation of the matrix $R_{\tilde{f}}$ from $U_{\tilde{f}}$.

The replacement of the squark fields can now be written as:

$$\begin{pmatrix} \tilde{f}_L \\ \tilde{f}_R \end{pmatrix} \rightarrow \left(\mathbb{1} + \frac{1}{2} \delta Z_{\tilde{f}} \right) \begin{pmatrix} \tilde{f}_L \\ \tilde{f}_R \end{pmatrix} = \left(\mathbb{1} + \frac{1}{2} \delta Z_{\tilde{f}} \right) R_{\tilde{f}}^{-1} \begin{pmatrix} \tilde{f}_1 \\ \tilde{f}_2 \end{pmatrix}$$

$$= U_{\tilde{f}}^\dagger \left(\mathbb{1} + \frac{1}{2} \delta \breve{Z}_{\tilde{f}} \right) \begin{pmatrix} \tilde{f}_1 \\ \tilde{f}_2 \end{pmatrix} \tag{2.11}$$

where the non-diagonal matrix $\delta \breve{Z}_{\tilde{f}}$ is introduced as

$$\delta \breve{Z}_{\tilde{f}} = U_{\tilde{f}} \delta Z_{\tilde{f}} U_{\tilde{f}}^\dagger - \delta Z_{U_{\tilde{f}}}, \quad \text{with} \quad \delta \breve{Z}_{\tilde{f}} = \begin{pmatrix} \delta \breve{Z}_{\tilde{f}_{11}} & \delta \breve{Z}_{\tilde{f}_{12}} \\ \delta \breve{Z}_{\tilde{f}_{21}} & \delta \breve{Z}_{\tilde{f}_{22}} \end{pmatrix}.$$

After replacing the parameters and fields, the lagrangian is divided into a renormalized part and the counterpart:

$$\mathcal{L} \quad \rightarrow \quad \mathcal{L} + \delta \mathcal{L},$$

$$\mathcal{L} \quad = \quad \left(\tilde{f}_1^*, \tilde{f}_2^* \right) \left(k^2 - D_{\tilde{f}} \right) \begin{pmatrix} \tilde{f}_1 \\ \tilde{f}_2 \end{pmatrix}, \tag{2.12}$$

$$\delta \mathcal{L} \quad = \quad \left(\tilde{f}_1^*, \tilde{f}_2^* \right) \left(\frac{k^2}{2} \left[\delta \breve{Z}_{\tilde{f}}^\dagger + \delta \breve{Z}_{\tilde{f}} \right] - \frac{1}{2} \left[\delta \breve{Z}_{\tilde{f}}^\dagger D_{\tilde{f}} + D_{\tilde{f}} \delta \breve{Z}_{\tilde{f}} \right] - U_{\tilde{f}} \delta M_{\tilde{f}}^2 U_{\tilde{f}}^\dagger \right) \begin{pmatrix} \tilde{f}_1 \\ \tilde{f}_2 \end{pmatrix}.$$

The Feynman rules for the counter squark propagators are defined by the last line in equation (2.12). The matrix $D_{\tilde{f}} = U_{\tilde{f}} M_{\tilde{f}}^2 U_{\tilde{f}}^\dagger$ is defined in equation (2.6). One can now write down the renormalized squark self energy $\hat{\Sigma}_{\tilde{f}}(k^2)$ as

$$\hat{\Sigma}_{\tilde{f}}(k^2) = \Sigma_{\tilde{f}}(k^2) + \frac{k^2}{2} \left[\delta \breve{Z}_{\tilde{f}}^+ + \delta \breve{Z}_{\tilde{f}} \right] - \frac{1}{2} \left[\delta \breve{Z}_{\tilde{f}}^+ D_{\tilde{f}} + D_{\tilde{f}} \delta \breve{Z}_{\tilde{f}} \right] - U_{\tilde{f}} \delta M_{\tilde{f}}^2 U_{\tilde{f}}^\dagger,$$

where $\Sigma_{\tilde{f}}(k^2)$ is the unrenormalized squark self energy. Now one has to define the renormalization conditions.

For one generation of squarks there are one mixing matrix (2.5) for up-type squarks and one for down-type. They contain five parameters $M_{\tilde{q}_L}$, $M_{\tilde{u}_R}$, $M_{\tilde{d}_R}$, A_u, A_d that are not fixed by other sectors. The three mass parameters M can be fixed by three on-shell conditions, choosing the isospin "+" system

$$\mathrm{Re}\,\hat{\Sigma}_{\tilde{u}_{ii}}(m_{\tilde{u}_i}^2) = 0 , \qquad i = 1, 2 \tag{2.13}$$

$$\mathrm{Re}\,\hat{\Sigma}_{\tilde{d}_{22}}(m_{\tilde{d}_2}^2) = 0 , \tag{2.14}$$

where in equation (2.14) it is assumed that $\tilde{d}_2 \neq \pm\tilde{d}_L$. If $\tilde{d}_2 = \pm\tilde{d}_L$ then (2.14) contains only the counterterm for $M_{\tilde{f}_L}^2$ which however is already defined by equation (2.13). Therefor one has to replace (2.14) by the condition $\mathrm{Re}\,\hat{\Sigma}_{\tilde{d}_{11}}(m_{\tilde{d}_1}^2) = 0$ to fix $M_{\tilde{d}_R}$.
The counterterms δA_f in the non-diagonal entries of the mass matrix can be fixed by the condition

$$\mathrm{Re}\,\hat{\Sigma}_{\tilde{f}_{12}}(m_{\tilde{f}_1}^2) + \mathrm{Re}\,\hat{\Sigma}_{\tilde{f}_{12}}(m_{\tilde{f}_2}^2) = 0 .$$

The diagonal Z-factors can be fixed by imposing that the residues of the propagators are equal to unity

$$\mathrm{Re}\,\frac{\partial\hat{\Sigma}_{\tilde{f}_{ii}}(k^2)}{\partial k^2}\bigg|_{(k^2=m_{\tilde{f}_i}^2)} = 0 ,$$

and the non-diagonal Z-factors by the condition $\mathrm{Re}\,\hat{\Sigma}_{\tilde{f}_{12}}(m_{\tilde{f}_2}^2) = 0$. With the choice $\delta\tilde{Z}_{\tilde{f}_{12}} = \delta\tilde{Z}_{\tilde{f}_{21}}$ one obtains

$$\delta\tilde{Z}_{\tilde{f}_{ii}} = -\,\mathrm{Re}\,\frac{\partial\hat{\Sigma}_{\tilde{f}_{ii}}(k^2)}{\partial k^2}\bigg|_{(k^2=m_{\tilde{f}_i}^2)} \qquad \text{and} \qquad \delta\tilde{Z}_{\tilde{f}_{12}} = -\frac{\mathrm{Re}\,\Sigma_{\tilde{f}_{12}}(m_{\tilde{f}_1}^2) - \mathrm{Re}\,\Sigma_{\tilde{f}_{12}}(m_{\tilde{f}_2}^2)}{m_{\tilde{f}_1}^2 - m_{\tilde{f}_2}^2} .$$

Three of the four mass counter terms are fixed by the conditions (2.13) and (2.14) to

$$\delta m_{\tilde{u}_1}^2 = \mathrm{Re}\Sigma_{\tilde{u}_{11}}(m_{\tilde{u}_1}^2) , \quad \delta m_{\tilde{u}_2}^2 = \mathrm{Re}\Sigma_{\tilde{u}_{22}}(m_{\tilde{u}_2}^2) , \quad \delta m_{\tilde{d}_1}^2 = \mathrm{Re}\Sigma_{\tilde{d}_{11}}(m_{\tilde{d}_1}^2) .$$

The fourth mass counterterm can be expressed as

$$\begin{aligned}
\delta m_{\tilde{d}_1}^2 &= -\frac{U_{\tilde{d}_{12}}^2}{U_{\tilde{d}_{11}}^2}\delta m_{\tilde{d}_2}^2 + 2\frac{U_{\tilde{d}_{12}}U_{\tilde{d}_{22}}}{U_{\tilde{d}_{11}}^2}\delta Y_{\tilde{d}_{12}} + \frac{U_{\tilde{u}_{11}}^2}{U_{\tilde{d}_{11}}^2}\delta m_{\tilde{u}_1}^2 + \frac{U_{\tilde{u}_{12}}^2}{U_{\tilde{d}_{11}}^2}\delta m_{\tilde{u}_2}^2 \\
&\quad - 2\frac{U_{\tilde{u}_{12}}U_{\tilde{u}_{22}}}{U_{\tilde{d}_{11}}^2}\delta Y_{\tilde{u}_{12}} + \frac{1}{U_{\tilde{d}_{11}}^2}(\delta C_{\tilde{d}_{11}} - \delta C_{\tilde{u}_{11}}),
\end{aligned} \tag{2.15}$$

where $\delta Y_{\tilde{f}_{12}}$ and $\delta C_{\tilde{f}_{11}}$ are defined by

$$\delta Y_{\tilde{f}_{12}} = \frac{1}{2}\left(\mathrm{Re}\,\Sigma_{\tilde{f}_{12}}(m_{\tilde{f}_1}^2) + \mathrm{Re}\,\Sigma_{\tilde{f}_{12}}(m_{\tilde{f}_2}^2)\right),$$

$$\delta C_{\tilde{f}_{11}} = 2m_f\delta m_f - e_f M_Z^2 \cos(2\beta)\,\delta s_W^2 + \left(T_f^3 - e_f s_W^2\right)\left(\cos(2\beta)\delta M_Z^2 + M_Z^2\,\delta\cos(2\beta)\right).$$

The counterterm δs_W^2 can be taken from the relation (2.3), then the dependence on δM_Z^2 in (2.15) drops out. The on-shell renormalization conditions for the fermion masses are $\delta m_f = \frac{1}{2} m_f [\mathrm{Re}\, \Sigma_{f_L}(m_f^2) + \mathrm{Re}\, \Sigma_{f_R}(m_f^2) + 2\mathrm{Re}\, \Sigma_{f_S}(m_f^2)]$ and the gauge-boson mass $\delta M_W^2 = \Sigma_W(M_W^2)$ [98]. The counterterm of $\tan\beta$ can be determined for vanishing $A^0 - Z$-mixing as $\delta\tan\beta = \mathrm{Im}\{\Sigma_{A^0 Z}(M_A^2)\}/(2 M_Z \cos^2\beta)$ [99, 100].

2.5.4   Counterterms of the Squark Vertices

Calculating loop corrections to the squark pair production, divergent loop integrals occur. The divergences are canceled by the corresponding counterterms. For squark pair production in photon-photon collision the counterterms to the $\gamma\tilde{f}\tilde{f}$ and $\gamma\gamma\tilde{f}\tilde{f}$ vertices are necessary. The relevant lagrangian is

$$\mathcal{L} = \mathcal{L}_{\tilde{f}\tilde{f}\gamma} + \mathcal{L}_{\tilde{f}\tilde{f}Z} + \mathcal{L}_{\tilde{f}\tilde{f}\gamma\gamma} + \mathcal{L}_{\tilde{f}\tilde{f}\gamma Z} \tag{2.16}$$

with

$$\mathcal{L}_{\tilde{f}\tilde{f}\gamma} = -iee_f A^\mu (\tilde{f}_L^*, \tilde{f}_R^*) \overleftrightarrow{\partial}_\mu \begin{pmatrix} \tilde{f}_L \\ \tilde{f}_R \end{pmatrix}, \quad \mathcal{L}_{\tilde{f}\tilde{f}Z} = \frac{-ie}{s_W c_W} Z^\mu (\tilde{f}_L^*, \tilde{f}_R^*) \overleftrightarrow{\partial}_\mu C_{\tilde{f}_{L/R}} \begin{pmatrix} \tilde{f}_L \\ \tilde{f}_R \end{pmatrix},$$

$$\mathcal{L}_{\tilde{f}\tilde{f}\gamma\gamma} = e^2 e_f^2 \, A^\mu A_\mu (\tilde{f}_L^*, \tilde{f}_R^*) \begin{pmatrix} \tilde{f}_L \\ \tilde{f}_R \end{pmatrix}, \quad \mathcal{L}_{\tilde{f}\tilde{f}\gamma Z} = \frac{2e^2 e_f}{s_W c_W} A_\mu Z^\mu (\tilde{f}_L^*, \tilde{f}_R^*) C_{\tilde{f}_{L/R}} \begin{pmatrix} \tilde{f}_L \\ \tilde{f}_R \end{pmatrix},$$

where $\overleftrightarrow{\partial}_\mu$ is defined in equation (A.6) and

$$C_{\tilde{f}_{L/R}} = \begin{pmatrix} T_f^3 - e_f s_W^2 & 0 \\ 0 & -e_f s_W^2 \end{pmatrix}. \tag{2.17}$$

The bare parameters of the lagrangian (2.16) are replaced by the renormalized ones $e \to e(1 + \delta Z_e)$ and $s_W \to s_W(1 + \delta Z_{sw})$, and for the squark fields relation (2.11) is used. The photon and Z-boson fields are replaced by

$$\begin{pmatrix} Z \\ A \end{pmatrix} \to \begin{pmatrix} 1 + \frac{1}{2}\delta Z_{ZZ} & \frac{1}{2}\delta Z_{ZA} \\ \frac{1}{2}\delta Z_{AZ} & 1 + \frac{1}{2}\delta Z_{AA} \end{pmatrix} \begin{pmatrix} Z \\ A \end{pmatrix}.$$

Introducing the renormalized fields and parameters into (2.16), the lagrangian splits into a renormalized part and a counterpart. The counterterm lagrangian of the $\tilde{f}\tilde{f}\gamma$ and $\tilde{f}\tilde{f}\gamma\gamma$ couplings are

$$\delta\mathcal{L}_{\tilde{f}\tilde{f}\gamma} = -iee_f A^\mu (\tilde{f}_1^*, \tilde{f}_2^*) \overleftrightarrow{\partial}_\mu \left(\delta Z_e + \frac{1}{2}\delta Z_{AA} + \frac{\delta Z_{ZA} \check{C}_{\tilde{f}}}{2 e_q c_W s_W} + \frac{1}{2}\delta\check{Z}^\dagger + \frac{1}{2}\delta\check{Z} \right) \begin{pmatrix} \tilde{f}_1 \\ \tilde{f}_2 \end{pmatrix},$$

$$\delta\mathcal{L}_{\tilde{f}\tilde{f}\gamma\gamma} = e^2 e_f^2 \, A^\mu A_\mu (\tilde{f}_L^*, \tilde{f}_R^*) \left(2\delta Z_e + \delta Z_{AA} + \frac{\delta Z_{ZA} \check{C}_{\tilde{f}}}{e_q s_W c_W} + \frac{1}{2}\delta\check{Z}^\dagger + \frac{1}{2}\delta\check{Z} \right) \begin{pmatrix} \tilde{f}_L \\ \tilde{f}_R \end{pmatrix}.$$
$$\tag{2.18}$$

where the matrix $\check{C}_{\tilde{f}}$ is defined as $\check{C}_{\tilde{f}} = U_{\tilde{f}} C_{\tilde{f}_{L/R}} U_{\tilde{f}}^\dagger$ and $U_{\tilde{f}}$ is given in (2.6) and $C_{\tilde{f}_{L/R}}$ in (2.17). From equation (2.18) one can read off the Feynman rules for the counterterm

vertices. For the automatic calculation, these expressions have to be implemented into the MSSM model-file [101] of FeynArts [102, 103], and have been taken from [104]. The renormalization conditions for the renormalization constants δZ_e, δZ_{AA} and δZ_{ZA} can be found in [94, 98] and are always implemented in the MSSM model-file.

Chapter 3

Particle Production at Future Linear Colliders

In great agreement of the high energy particle physicists, the next type of collider after the LHC will be a linear electron positron collider. Although the available center-of-mass energy will be much lower than that of the LHC, the advantage of this type of collider is the enormous precision with which particles can be detected. Currently, four different projects have been developed: NLC [21], JLC [22], Clic [105], and at most advanced level TESLA with a complete Technical Design Report [106].

3.1   Scattering Types at Linear Collider

The basic concept of the next linear collider is the scattering of high energy electrons with positrons of opposite direction. In addition to this there are other running options that could be realized in practice. One possibility which can be carried out easily is e^-e^- scattering (see e.g. [106, 107] and references therein). Another option is to construct a photon collider. Using Compton backscattered laser light off the high energy electrons [28, 29, 108–110] one can built either an electron-photon or photon-photon collider. Developments for these options are made for all four colliders NLC [21], JLC [22–24], Clic [25], and TESLA [26, 27].

In real experiments one does not have pure $e^-e^\pm$, $e^-\gamma$ or $\gamma\gamma$ scattering. Several reactions occur simultaneously because of background and beam-beam interactions [111]. In $e^-e^\pm$ collisions, photons arise from beamstrahlung and bremsstrahlung effects, leading to $e^-\gamma$ and $\gamma\gamma$ background reactions. Whereas at a $\gamma\gamma$-collider background reactions appear from e^-e^-, $e^-\gamma$ collisions and at a $e^-\gamma$ collider from $\gamma\gamma$ and e^-e^- scattering.

Beamstrahlung photons arises due to the high density of the electrons and positrons in the bunches at the interaction point. At e^+e^- colliders the two bunches focus each other, thus the particle trajectories are bent, resulting in a synchrotron radiation (referred to as beamstrahlung). This so-called pinch effect was analyzed in detail for a

collider energy of 500 GeV in [111]. This effect leads to an increased e^+e^- luminosity but also to an energy loss of the scattering particles. This energy spread is important for all precision measurements at linear colliders. The largest spread will occur at the current 3 TeV Clic design with a momentum spread of 31% [105].

In contrast to e^+e^- scattering, in e^-e^- the two beams will blow up each other at the interaction point (Beam Repulsion). Therefore, the luminosity and the beamstrahlung are much smaller than in e^+e^- scattering (To increase the luminosity in e^-e^- scattering, one can decrease the horizontal beam size.).

Bremsstrahlung processes are the second source of photons in $e^-e^\pm$ scattering. Here, two particle beams of opposite direction collide and one of them emits a photon. The spectrum can be calculated as Compton scattering of an electron and a virtual photon in the equivalent photon approximation (see e.g.[112]). It is reduced by the beam size effect (see for example [113]) that roughly decreases the spectrum by a factor of two [111]. The total number of photons in this case is much smaller than that of beamstrahlung [111, 114, 115]. The photon density function for low x (ratio of photon energy with respect to the electron beam energy E_0) is much smaller than for beamstrahlung. Only for large x the bremsstrahlung can be higher than beamstrahlung, even if in a region where they are both very small.

At a e^+e^- collider the produced brems- and beamstrahlung photons lead to $\gamma\gamma$ background reactions, that produce the same final states as the e^+e^- collisions. Backgrounds from $e\gamma$ scattering can be reduced by the overall charge of the final state. To include beamstrahlung effects in precise e^+e^- calculations one can use the program Circe [116] for collider energies up to 1 TeV. It provides a simple and, in terms of computing time, fast approximation for the beamstrahlung effect, based on simulations of the program Guinea-Pig [115]. In this thesis, the calculation of the process $e^+e^- \to \tilde{g}\tilde{g}$ (Chapter 4) is presented. Because of the large gluino masses, the small cross section and the much larger uncertainty of the cross section due to the scale dependence of the results ($\alpha_s(\mu)$), brems- and beamstrahlung effects are neglected for this process.

At a photon collider one will have a mixture of e^-e^-, $e^-\gamma$ and $\gamma\gamma$ scattering processes. Electron beams on both sides will be used, because of the overall charge it is easy to distinguish between the different scattering types of collisions. Also the lower e^-e^- luminosity reduces the background reactions due to beam repulsion. Another advantage of using e^-e^- scattering is given by the higher polarization degree reachable for electrons (80%) compared to positrons (60%). To realize a photon collider one uses backscattered laser light discussed in the next section. The influence of brems- and beamstrahlung at a $\gamma\gamma$ collider is discussed in Section 3.3.

3.2   Laserbackscattering

As mentioned before, using Compton backscattering of laser light of high energy electrons, it is possible to build a photon collider for $e\gamma$ and $\gamma\gamma$ collisions (for a review of collider setup and physics potential see [26, 117] and references therein). A simple scheme to realize a photon-photon collider is shown in Fig. 3.1. At the conversion point (CP) the electron beam with energy E_0 and polarization $|\lambda_e| \leq 1/2$ collides at a small
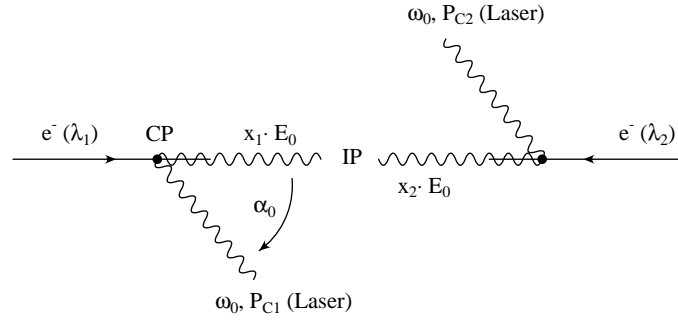
Figure 3.1: Scheme of photon colliders for $\gamma\gamma$ scattering.

angle α_0 with the initial laser with energy ω_0 and polarization $|P_c| \leq 1$. The distance b between the CP and the interaction point (IP) is around 1-5mm. By Compton scattering a high energy photon beam will travel in the direction of the original electrons with a small angular spread $\sim 1/\gamma$, with $\gamma = E_0/m_e c^2$. Using a laser of several Joule almost all electrons will convert some of their energy into high energetic photons, leading to an energy distribution $\omega = \omega(\vartheta)$ of backscattered photons in dependence of their emission angle ϑ [28, 29]

$$\omega = \frac{\omega_m}{(1 + (\vartheta/\vartheta_0)^2)}, \qquad \text{with} \qquad \vartheta_0 = \frac{m_e c^2}{E_0}\sqrt{1 + X},$$

where
$$X = \frac{4E_0\omega_0}{m_e^2}\cos^2\frac{\alpha_0}{2} \simeq 15.3\left[\frac{E_0}{\text{TeV}}\right]\left[\frac{\omega_0}{\text{eV}}\right] = 19\left[\frac{E_0}{\text{TeV}}\right]\left[\frac{\mu\text{m}}{\lambda}\right]. \tag{3.1}$$

Here ω_m is the maximum backscattered photon energy (at $\vartheta = 0$):

$$\omega_m = \frac{X}{1 + X}E_0 . \tag{3.2}$$

Thus, in principle the energy ω_0 of the initial laser photons should be chosen as high as possible. However, the backscattered photons will also scatter with the laser photons. For to high energies ω_0 this would lead to e^+e^- pair creation. For example, for the current TESLA design a laser with $\omega_0 = 1.17$ eV ($\lambda = 1.06\mu$) is planned. For $E_0 = 250$ GeV this leads to $X = 4.5$ with $\omega_m/E_0 = 0.82$ and for $E_0 = 400$ GeV to $X = 7.2$ with $\omega_m/E_0 = 0.878$. For $X > 4.8$ it was shown [28, 29, 109, 110] that the luminosity will be reduced because of pair creations. But nonlinear effects in the conversion region effectively increase the threshold for e^+e^- production, so that e^+e^- production is reduced [26] and one can use a laser with $\lambda = 1.06\mu$ for all TESLA energies.

However, if one considers squark and gluino pair productions, one always has two heavy particles in the final state. Because of the mass constraints given in Section 2.4, there is not much room for measurements at a $2E_0 = 500$ GeV $\gamma\gamma$ collider. Thus, for this thesis, center-of-mass energies up to 3 TeV like in the Clic project will be taken in consideration. The Clic value $X = 6.5$, given by [25], with $\omega_m/E_0 = 0.867$ is chosen for all $\gamma\gamma$ energies.

As a simple approach, the energy spectrum of the backscattered photons $f_{\gamma/e}^{\text{laser}}(x)$ is defined by the Compton cross section. It depends on X and on the polarization of the initial electron $|\lambda_e| \leq 1/2$ and laser photon $|P_c| \leq 1$ as follows [108]

$$f_{\gamma/e}^{\text{laser}}(x) = \frac{1}{N_c + 2\lambda_e P_c N_c'} \left[1 - x + \frac{1}{1-x} - \frac{4x}{X(1-x)} + \frac{4x^2}{X^2(1-x)^2} \right.$$

$$\left. - 2\lambda_e P_c \frac{x(2-x)[x(X+2) - X]}{X(1-x)^2} \right], \qquad (3.3)$$

where

$$N_c = \left[1 - \frac{4}{X} - \frac{8}{X^2} \right] \ln(1+X) + \frac{1}{2} + \frac{8}{X} - \frac{1}{2(1+X)^2} ,$$

$$N_c' = \left(1 + \frac{2}{X} \right) \ln(1+X) - \frac{5}{2} + \frac{1}{1+X} - \frac{1}{2(1+X)^2} .$$

Here x is the ratio of the backscattered photon energy ω to the energy E_0 of the initial electron. Equation (3.3) shows that the spectrum depends on the polarization of the initial electron and photon only in the combination $2\lambda_e P_c$.

The distribution of the photon spectrum for $X = 6.5$ with $\omega_m = 0.867E_0$ is given in Fig. 3.2. By choosing the right polarization of the electrons and photons, the spectrum has a high energy peak. This means that the number of photons is double compared to the unpolarized case. The distribution is most peaked if the initial electrons are longitudinally polarized, the photons are circularly polarized and $2\lambda_e P_c = -1$. Unfortunately, in the experiments one will not reach a value of -1. The initial laser can be assumed to be 100% polarized, but for electrons a conservative polarization degree of 80% is assumed, leading to $2\lambda_e P_c = -0.8$. The corresponding energy spectrum is also given in Fig. 3.2 (solid line) and is used for all calculations of polarized cross sections.

The polarization type of the backscattered photons can be controlled by the polarization of the initial laser photons. Choosing a circular/linear polarization the backscattered photons are also circular/linear polarized. The polarization degree of the backscattered photons can be expressed by the Stokes parameter ξ_1, ξ_2, ξ_3. All calculations of this thesis use circular polarized photon beams. In case of circular polarization $\xi_1 = \xi_3 = 0$ and $\xi_2(x)$ is defined by

$$\xi_2^{\text{laser}}(x) = \frac{\Delta f_{\gamma/e}^{\text{laser}}(x)}{f_{\gamma/e}^{\text{laser}}(x)} , \qquad \text{with} \qquad \Delta f_{\gamma/e}(x) = f_{\gamma/e}^+(x) - f_{\gamma/e}^-(x), \qquad (3.4)$$

where $f_{\gamma/e}^+(x)$ $(f_{\gamma/e}^-(x))$ indicates the spectrum of the right (left) circularly polarized photons. $\Delta f_{\gamma/e}^{\text{laser}}(x)$ reads

$$\Delta f_{\gamma/e}^{\text{laser}}(x) = \frac{1}{N_c + 2\lambda_e P_c N_c'} \left\{ 2\lambda_e \frac{x}{1-x} \left[1 + (1-x)\left(1 - \frac{2x}{(1-x)X} \right)^2 \right] \right.$$

$$\left. + P_c \left(1 - \frac{2x}{(1-x)X} \right)\left(1 - x + \frac{1}{1-x} \right) \right\}. \quad (3.5)$$
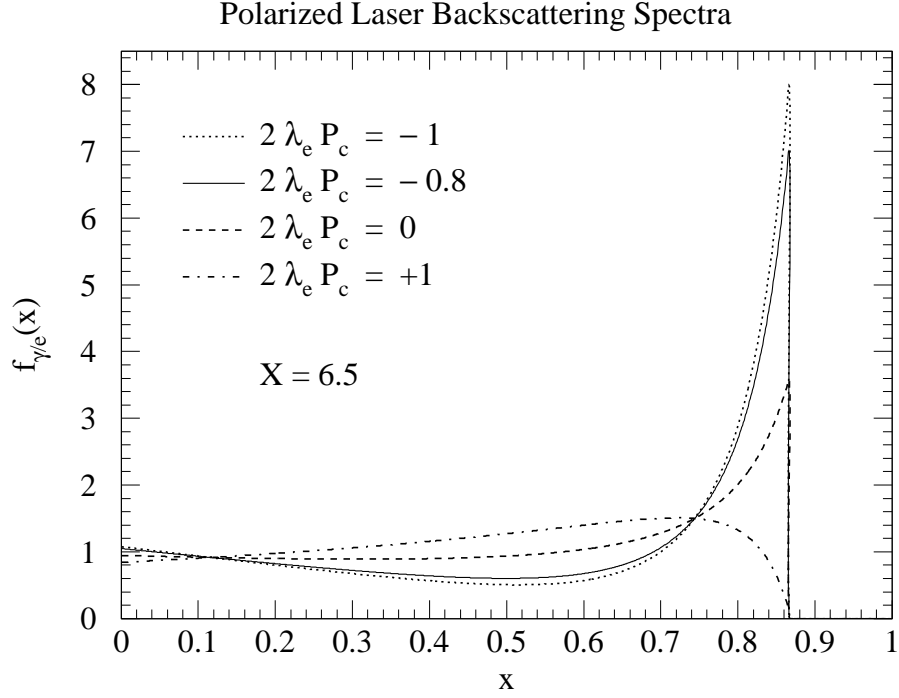
Figure 3.2: Laser backscattering spectra for different combinations of electron and laser photon polarization $2\lambda_e P_c$.

The polarization degree for $X = 6.5$ and different polarizations of the initial electrons and laser photons is shown in Fig. 3.3. The distribution depends separately on the electron and laser polarization. It is important to note that for the "unpolarized" spectrum ($2\lambda P_c = 0$) the photon distribution function $f_{\gamma/e}(x)$ in Fig. 3.2 has the same shape if λ or P_c is zero, but the spectrum of the polarization degree of the backscattered photons has a different behavior (Fig. 3.3). This would lead to different cross sections. As it can be seen in Fig. 3.2, the monochromaticity of the backscattered photons in the high energy peak ($x = 0.69 - 0.867$) can be improved considerably by choosing $2\lambda_e P_c = -1$ or in realistic experiments $2\lambda_e P_c = -0.8$. Thus, for all calculations $2\lambda_e P_c = -0.8$ is chosen leading to a photon spectrum with a high energy peak that is highly polarized.

Furthermore, it should be noted that by switching the signs of λ_e and P_c simultaneously, one can switch the helicity ξ_2 of the outgoing photons without changing the photon spectrum or spoiling its monochromaticity.

Polarization Degree of Backscattered Photons
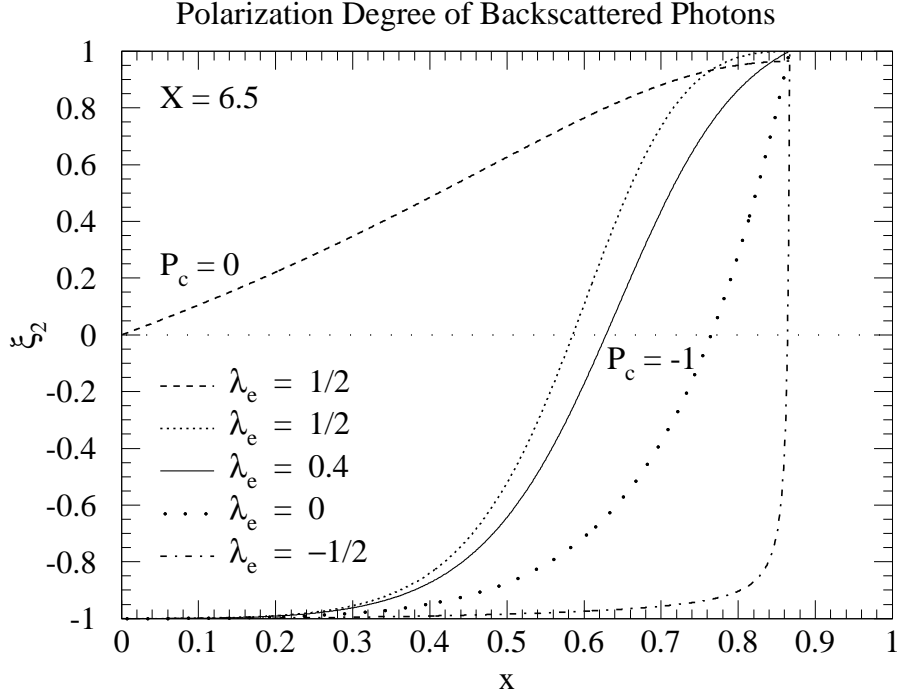
Figure 3.3: Degree of circular polarization for laser-backscattered photons. For the dashed line the initial laser polarization is $P_c = 0$, for all other lines $P_c = -1$.

3.3 Real Photon Spectrum and Luminosity

The laser spectrum of Fig. 3.2 is a highly idealistic spectrum. There are some effects that change the spectrum:

- **Nonlinear Effect:**
  Because of the very strong electro-magnetic field in the laser wave at the conversion point, the initial electron can interact simultaneously with several laser photons (see [118] and references therein). This effect can be interpreted as an effective increase of the electron mass $m_e^2 \to m_e^2(1 + \xi^2)$, where ξ^2 describes the nonlinear effect and is defined as[1]: $\xi^2 = n_\gamma(4\pi\alpha_e)/(m_e^2\omega_0)$. Here n_γ is the photon density in the wave and ω_0 the laser energy. $\xi^2 = 0$ is the ideal case. When the value of ξ^2 is increased, the high energy peak is shifted to lower energies and the sharp edge becomes "smeared". Therefore, ξ^2 should not be much larger than 0.3.

- **Angular correlations:[119]**
  The electron bunches collide at the conversion point with the initial laser photons

---

[1]This ξ should not be confused with the polarization degree of the last section.

at a distance of 1-5mm from the interaction point. The angular spread of the backscattered photons is proportional to $1/\gamma$, and the photons with lower energy have a wider production angle. Therefore, with the growth of the distance b the low energy photons are spread more and more. The result is a suppression of interactions with low energy photons.

- **Electron re-scattering:**
  The initial electrons convert a part of their energy in a high energetic photon. However, due to the Compton spectrum, some of them still have sufficient energy to interact with another initial laser photon (see [29, 119]). This leads to an additional contribution to the photon spectrum, where this "second generation" of photons have in principle lower energies, their polarization is practically zero, and there is no definite relation between energy and production angle of the backscattered photons.

All these three effects are included in the program CompaZ [120] and can be used to simulate photon and luminosity spectra for a photon collider of 500 GeV at TESLA.

Fig. 3.4 shows a simulation of the normalized luminosity spectrum of the backscattered photons, assuming that both initial electron beams have the same polarization and $2\lambda_e P_c = -0.85$. The distribution is plotted over $z = W_{\gamma\gamma}/2E_0$, where $W_{\gamma\gamma}$ is
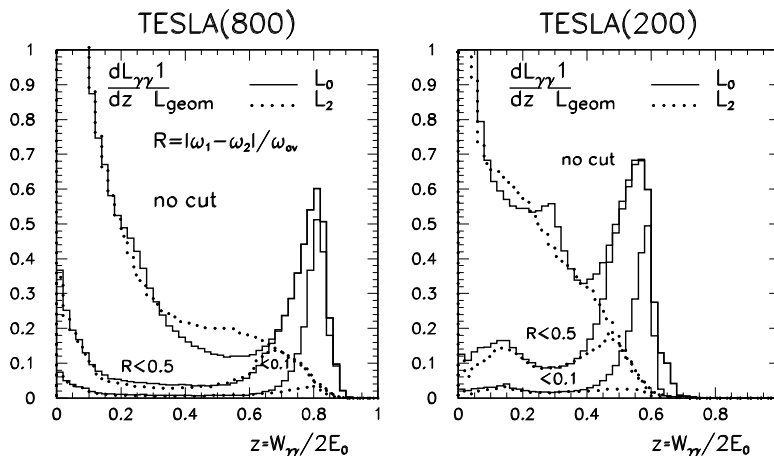
Figure 3.4: The $\gamma\gamma$ luminosity spectra at TESLA for $2E_0 = 800$ and 200 GeV with various cuts on longitudinal momentum. The solid line is for the total helicity of the two photons 0 and the dotted line for total helicity 2. The initial electron polarization is 85%. The plot was taken from [121].

the $\gamma\gamma$-center-of-mass energy. The spectrum consists of two types of curves, one for total $\gamma\gamma$ helicity equal to 0 (solid line) and one for $L = 2$ (dotted line). The spectrum of $L = 0$ has a high energy peak with a width at half maximum of about 15% originated by the peak of the laser photon density function, Fig. 3.2. There is also a large contribution to the spectrum at low energies. This is due to the collision of

beamstrahlung and multiple Compton scattering photons of one bunch with laser photons which are backscattered from the opposite bunch. Therefore, they have large longitudinal momenta. Contributions due to bremsstrahlung are negligible because of the beam repulsion the e^-e^- luminosity is only 10^{-2} of the geometric luminosity. For measurements one will always use the high energy peak with $z > 0.8\,z_{max}$ where $z_{max} = W_{\gamma\gamma}^{max}/2E_0$ and $W_{\gamma\gamma}^{max} = 2\omega_m = \frac{X}{1+X}2E_0$ (equation (3.2)) is the maximum available $\gamma\gamma$-center-of-mass energy. The distribution of this peak, that is well known, is not affected by beamstrahlung and multiple Compton scattering and has a high monochromaticy (Fig. 3.3). The luminosity of this peak is

$$\mathcal{L}_{\gamma\gamma}(z > 0.8z_m) \approx 0.1\,\mathcal{L}_{geom}\;. \tag{3.6}$$

Events of the low energy part of the spectrum in Fig. 3.4 can be suppressed by imposing cuts on the longitudinal momentum of the produced system. Normally, one restricts the longitudinal momentum using the acollinearity angle between jets (e.g. H $\rightarrow$ $b\bar{b}, \tau\bar{\tau}$)[117]. For production processes of supersymmetric particles this will be more complicated. Assuming R-parity conservation, the supersymmetric particles decay into a lightest supersymmetric particle, usually the lightest neutralino, that is invisible. Since in this case, supersymmetric particles can only be produced in pairs, the missing energy originates from at least two invisible particles.

A possible solution to this problem could be to choose the center-of-mass energy of the electron system in such a way that the production threshold of the scattering process is 0.8 of the maximum energy of the photon-photon system $W_{\gamma\gamma}^{max}$:

$$\sum_i m_i \;=\; 0.8\,W_{\gamma\gamma}^{max}\;, \quad \text{with} \quad W_{\gamma\gamma}^{max} \;=\; 2\,\omega_m\;,$$

and the electron center-of-mass energy is

$$S_{ee} \;=\; (2E_0)^2 \;=\; \left(\frac{X+1}{X}\frac{\sum_i m_i}{0.8}\right)^2\;, \tag{3.7}$$

where i runs over all particles of the final state and X is defined in equation (3.1). This procedure suppresses the low energy part of the spectrum. For the plots in this thesis equation (3.7) is used. If the electron center-of-mass energy is chosen independently of the final masses, the photon energy is integrated from $z_{min} = 0.8\,z_{max}$ to z_{max}, provided that the cuts introduced above are possible.

To calculate electron-electron cross sections one has to integrate over the photon structure function defined in equations (3.3) and (3.5). This density function is normalized to 1 for $0 \le x \le 1$. Whereas the $\gamma\gamma$-luminosity is given only for the high energy peak $z \ge 0.8\,z_{max}$ (equation (3.6)). If one wants to calculate the number of events by simple multiplication of the cross section with the luminosity defined as in (3.6), one has to renormalize the density function to the high energy peak or, equivalently, divide the cross section by N_f with

$$N_f = \int_0^{x_{max}} \mathrm{d}x_1 \int_0^{x_{max}} \mathrm{d}x_2\, f(x_1)f(x_2)\,\Theta(x_1x_2 - z_{min}^2)\;,$$

where $x_{max} = \omega_m/E_0$, Θ is the step function and f is either the polarized or unpolarized photon density function.

For an easy comparison, in this thesis the Compton spectrum defined in equation (3.3) and (3.5) is always used. Furthermore, the following values are chosen

$$
\begin{aligned}
X &= 6.5 \ , & 2\lambda_e P_c &= -0.8 \ , \\
z_{min} &= 0.8\,z_{max} \ , & \lambda_e^{\{-,0,+\}} &= \{-0.4,\ 0,\ 0.4\} \ , \\
z_{min} &= 0.693 \ , & x_{max} = z_{max} &= 0.867 \ , \\
f_{Norm}^{\pm} &= 0.291 \ , & f_{Norm}^{unpol} &= 0.184 \ .
\end{aligned}
$$

The sign of the initial laser polarization with $|P_c| = 1$ depends on the electron polarization in order that $2\lambda_e P_c = -0.8$ is fulfilled. Thus, the polarized cross section labels "++, −−, +−, −+" refer to the sign of the initial electron polarization. For unpolarized cross sections one has $\lambda_e = 0$ and $P_c = 0$ is used for both beams and the unpolarized photon spectrum.

Eventually, it should be noted that at a $\gamma\gamma$ collider there are no limitations to the geometric luminosity because of beamstrahlung or beam-instabilities. Therefore, one can decrease the beam size to increase the luminosity of the backscattered photons. For TESLA [26], it was shown that one could in principle decrease the horizontal beam size from 500nm to 10nm. Also the vertical beam size could be decreased by a factor two. Thus, in principle the $\gamma\gamma$ luminosity can be higher than the e^+e^- luminosity.

3.4   Hadronic Cross Sections

A general scattering process at a future linear electron collider is given by

$$
e^-(p_1, \lambda_1) + e^\pm(p_2, \lambda_2) \ \rightarrow \ \ldots \ \rightarrow \ X_1(k_1) + X_2(k_2) + \ldots + X_n(k_n) \ ,
$$

where p_i and λ_i are the momentum and polarization of the initial electrons and positrons, and X_i stands for an arbitrary particle in the final state with momentum k_j. Polarization indices of the final state are suppressed. The intermediate dots indicate the possibility that one or two of the initial electrons/positrons might be "converted" to a photon.

To calculate the cross section of the initial electron-electron/positron system one has to integrate over a possible photon density function:

$$
\sigma_{e^-e^\pm}^{\lambda_1\lambda_2}(S) \ = \ \int_0^1 \mathrm{d}x_1 \mathrm{d}x_2 \ \sum_{P_i P_j} f_{i/e}^{P_i}(x_1, \lambda_1) f_{j/e}^{P_j}(x_2, \lambda_2) \ \hat{\sigma}_{ij}(\hat{s}, P_i, P_j) \ , \qquad (3.8)
$$

where S is the center-of-mass energy of the initial electron/positron system, $\hat{s} = (x_1 p_1 + x_2 p_2)^2$ the center-of-mass energy of the partonic subsystem and $\hat{\sigma}_{ij}$ the partonic cross section with initial particles i and j. The sum runs over all possible polarization states $P_{i/j}$ of the intermediate particles and, in case of photon-photon scattering ($i = \gamma_1, j =$

γ_2), over the 4 polarization combination of γ_1 and γ_2. The momentum fraction of the intermediate particles with respect to the initial electron/positron are denoted by x_1 and x_2. The parton density functions in the electron or positron for different scattering processes can be described as follows:

$$\text{Direct e}^-\text{e}^\pm \text{ collision}: \quad f_{i/e}(x) = \delta_{ie}\delta(1-x),$$

$$\text{Direct photon}: \quad f_{\gamma/e}^P(x, \lambda), \quad [\text{photon energy spectrum, e.g. (3.3)}],$$

$$\text{Resolved photon}: \quad f_{a/e}(x) = \int_x^1 \frac{\mathrm{d}y}{y} f_{\gamma/e}\left(\frac{x}{y}\right) f_{a/\gamma}(y).$$

There is an additional integration for resolved processes. In these the photons emitted by the initial electrons/positrons fluctuate into virtual quark-antiquark pairs. Thus, the photon beams present a hadronic structure of quarks, antiquarks and also gluons radiated by quarks and antiquarks. These particles can scatter with the opposite beam. This is an effective description of a multi-particle final state process, where it is possible to calculate e.g. $q\bar{q} \to \tilde{g}\tilde{g}$ instead of $\gamma\gamma \to q\bar{q}\tilde{g}\tilde{g}$. Thus, one has to integrate over all possible momentum fraction y of the quarks/antiquarks inside the initial photon.

For the laser-backscattering, it is assumed that the initial electrons are longitudinal polarized and the initial laser is circular polarized. The total electron cross section can be written with the Stokes parameter $\xi_2(x_i)$ as

$$\sigma_{e^-e^-}^{\lambda_1\lambda_2}(S) = \int_0^1 \mathrm{d}x_1 \mathrm{d}x_2 \; f_{i/e}(x_1, \lambda_1) f_{j/e}(x_2, \lambda_2) \; \times \Bigg\{$$

$$+ \frac{1}{4}\left(1 + \xi_2^{\lambda_1}\right)\left(1 + \xi_2^{\lambda_2}\right)\hat{\sigma}_{ij}(\hat{s}, +, +) + \frac{1}{4}\left(1 + \xi_2^{\lambda_1}\right)\left(1 - \xi_2^{\lambda_2}\right)\hat{\sigma}_{ij}(\hat{s}, +, -)$$

$$+ \frac{1}{4}\left(1 - \xi_2^{\lambda_1}\right)\left(1 + \xi_2^{\lambda_2}\right)\hat{\sigma}_{ij}(\hat{s}, -, +) + \frac{1}{4}\left(1 - \xi_2^{\lambda_1}\right)\left(1 - \xi_2^{\lambda_2}\right)\hat{\sigma}_{ij}(\hat{s}, -, -)\Bigg\},$$

where $f_{(i,j)/e}$ is the unpolarized laser spectrum of equation (3.3) and the dependence of $\xi_2^{\lambda_i}$ on x_i (equation (3.4)) has been omitted. The "-" and "+" refer to left and right polarization of the backscattered photons, respectively.

The integral over the total cross section defined in equation (3.8) contains 2 numerical integration over x_1, x_2. The numerical evaluation of the cross section, especially for higher order corrections or multi-particle final states, requires a large amount of computing time. To reduce this time one can rewrite equation (3.8) in a more convenient way. In the following, as an example unpolarized initial states are assumed. The partonic center-of-mass energy $\hat{s}$ is given in terms of the electron center-of-mass energy $S = (p_1 + p_2)^2$ as

$$\hat{s} = (x_1 p_1 + x_2 p_2)^2 = x_1 x_2 S + x_1(x_1 - x_2)p_1^2 + x_2(x_2 - x_1)p_2^2 \approx x_1 x_2 S \; .$$

The last relation is always fulfilled in high energy electron-electron scattering processes because $x_{1,2} \leq 1$ and $S \gg p_{1,2}^2 = m_e^2$. If τ_0 is the production threshold $\tau_0 = \hat{s}_{min}/S$

of the considered scattering process with k final particles and $\tau_0 = (\sum_k m_k)^2/S$, the total electron cross section (3.8) can be rewritten as follows

$$\sigma_{e_1 e_2}(S) = \sum_{\{i,j\}} \int_{\tau_0}^1 \mathrm{d}x_1 \int_{\frac{\tau_0}{x_1}}^1 \mathrm{d}x_2 \frac{1}{1+\delta_{ij}} \Big(f_{i/e_1}(x_1) f_{j/e_2}(x_2) + f_{j/e_1}(x_1) f_{i/e_2}(x_2) \Big) \hat{\sigma}_{ij}(\hat{s}) \ ,$$

where the sum over the ordered pairs (i,j) was replaced by a sum of unordered pairs $\{i,j\}$. The factor $1/(1+\delta_{ij})$ is introduced to avoid double counting. With the substitution $x_1 = x$ and $x_1 x_2 = \tau = \hat{s}/S$, the total cross section is given by

$$\sigma_{ee}(S) = \sum_{\{i,j\}} \int_{\tau_0}^1 \mathrm{d}\tau \, \frac{\mathrm{d}\mathcal{L}_{ij}^{ee}}{\mathrm{d}\tau} \, \hat{\sigma}_{ij}(\hat{s}),$$

with $d\mathcal{L}_{ij}^{ee}/d\tau$ defined as

$$\frac{d\mathcal{L}_{ij}^{ee}}{d\tau} = \int_\tau^1 \frac{\mathrm{d}x}{x} \frac{1}{1+\delta_{ij}} \Big(f_{i/e_1}(x) f_{j/e_2}(\frac{\tau}{x}) + f_{j/e_1}(x) f_{i/e_2}(\frac{\tau}{x}) \Big) \ .$$

The integration of the last equation is usually much faster than the one with an additional integration over the partonic cross section.

3.4.1 Rapidity and Transversal Momentum distribution for $2 \to 2$

The hadronic cross section of a $2 \to 2$ scattering process is given in equation (3.8). Suppressing again initial polarization indices and neglecting the initial particle masses, the electron-electron cross section in terms of the squared matrix element reads

$$\sigma_{e^- e^-} = \int \mathrm{d}x_1 \mathrm{d}x_2 \, f(x_1) f(x_2) \, \frac{\mathrm{d}^3 k_1}{(2\pi)^3 2k_1^0} \frac{\mathrm{d}^3 k_2}{(2\pi)^3 2k_2^0} (2\pi)^4 \delta^4(p_1 + p_2 - k_1 - k_2) \frac{1}{2\hat{s}} |M|^2 \ , \tag{3.9}$$

with $\hat{s} = x_1 x_2 S$ and k_1, k_2 are the momenta of the final particles in the partonic center-of-mass system, k_1^0, k_2^0 their energy and m_1, m_2 their masses. Equation (3.9) can be expressed in terms of the transversal momentum k_T and rapidity $y_i = \frac{1}{2} \ln \frac{k_i^0 + k_i^z}{k_i^0 - k_i^z}$. With $d^3 k = k^0 \, k_T dk_T \, d\phi \, dy$ equation (3.9) becomes [122]

$$\sigma_{e^- e^-} = \int \mathrm{d}k_T^2 \, \mathrm{d}y_1 \mathrm{d}y_2 \, x_1 f(x_1) \, x_2 f(x_2) \frac{\mathrm{d}\hat{\sigma}_{2 \to 2}}{\mathrm{d}t} \ , \tag{3.10}$$

where the differential partonic $2 \to 2$ cross section is

$$\frac{\mathrm{d}\hat{\sigma}_{2 \to 2}}{\mathrm{d}t} = \frac{1}{16\pi \hat{s}^2} |M|^2 \ , \tag{3.11}$$

and

$$x_1 = \frac{1}{\sqrt{S}} \left(m_{T_1} e^{y_1} + m_{T_2} e^{y_2} \right) \ , \qquad x_2 = \frac{1}{\sqrt{S}} \left(m_{T_1} e^{-y_1} + m_{T_2} e^{-y_2} \right) \ .$$

The "transverse mass" is defined as $m_T = \sqrt{k_T^2 + m^2}$. The integration boundaries of equation (3.10) are

$$0 \leq k_T \leq \frac{1}{2\sqrt{S}}\sqrt{(S - m_1^2 - m_2^2)^2 - 4m_1^2 m_2^2}, \qquad |y_1| \leq \mathrm{arcosh}\frac{S + m_1^2 - m_2^2}{2\sqrt{S}m_{T_1}} \ ,$$

and

$$-\ln\frac{\sqrt{S} - m_{T_1}e^{-y_1}}{k_T} \leq |y_2| \leq \ln\frac{\sqrt{S} - m_{T_1}e^{y_1}}{k_T} \ .$$

3.4.2 Partonic $2 \to 3$ Cross Section

To calculate the real photon and gluon emission one has to compute the partonic cross section for $2 \to 3$ scattering processes. The initial momenta are denoted as p_i, the final momenta as k_j and the partonic center-of-mass energy is $\hat{s} = (p_1 + p_2)^2$. The total cross section is defined as

$$\hat{\sigma}_{2\to3}(\hat{s}) = \int \frac{\mathrm{d}^3 k_1}{(2\pi)^3 2k_1^0} \frac{\mathrm{d}^3 k_2}{(2\pi)^3 2k_2^0} \frac{\mathrm{d}^3 k_3}{(2\pi)^3 2k_3^0} (2\pi)^4 \delta^4(p_1 + p_2 - k_1 - k_2 - k_3)\frac{1}{2\hat{s}}|M|^2.$$

(3.12)

Equation (3.12) can be rewritten [123] as a four dimensional integral in terms of the final particle energies k_1^0 and k_3^0 and the angles θ and η. Neglecting the masses of the initial particles the cross section becomes

$$\hat{\sigma}_{2\to3}(\hat{s}) = \int_\lambda^{(k_3^0)^{\max}} \mathrm{d}k_3^0 \int_{(k_1^0)^{\min}}^{(k_1^0)^{\max}} \mathrm{d}k_1^0 \int_{-1}^{1} \mathrm{d}\cos\theta \int_0^{2\pi} \mathrm{d}\eta \ \frac{1}{8(2\pi)^4} \frac{1}{2\hat{s}} |M|^2,$$

(3.13)

with $\lambda = max\{m_3, E_{\mathrm{cut}}\}$. The integration boundaries are

$$(k_3^0)^{\max} = \frac{1}{2\sqrt{\hat{s}}}\left(\hat{s} - (m_{k_1} + m_{k_2})^2 + m_{k_3}^2\right),$$

$$(k_1^0)^{\max}_{\min} = \frac{1}{2\tau}\left[a(\tau + m_+ m_-) \pm |\vec{k}_3|\sqrt{(\tau - m_+^2)(\tau - m_-^2)}\right],$$

$$\tau = a^2 - |\vec{k}_3|^2 \ , \qquad a = \sqrt{\hat{s}} - k_3^0 \ , \qquad m_\pm = m_{k_1} \pm m_{k_2}$$

3.5 Calculation Methods

To calculate the cross sections of the considered scattering processes with perturbative methods the following way is used:

- Draw all Feynman diagrams

- Write down the corresponding matrix elements

- Square and simplify the matrix elements

- Integrate numerically over the phase space

Because of the large number of different diagrams in loop calculations, computer programs have to be used. Moreover, a very important reason for an automatized computation is the prevention of calculation errors that frequently appear. Therefore, to create the Feynman diagrams and the matrix elements, the Mathematica package FeynArts [102, 103] version 3.2 combined with the MSSM model-file [101] was used.

In order to square matrix elements, a Mathematica package has been expressly developed. This uses at some points the algebraic program FORM [124]. It is written in a generic way like FormCalc [123] and FeynCalc [125]. It calculate the square of one-loop matrix elements and is described in detail in the next section.

For the integration over the phase space a generic Fortran program was developed, which performs also integrations over the structure functions if required (Section 3.5.2).

3.5.1 Analytical Calculation of Matrix Elements

Fig. 3.5 shows a road-map for the analytic calculation of squared matrix elements using Mathematica and FORM. The FeynArts generated matrix elements are given in Mathematica code. The amplitudes are simplified with different Mathematica functions (introduce abbreviations, reduce tensor structures, contract Lorentz indices, calculate traces, perform the helicity and color amplitude). Some of them use the computer program FORM. Therefore, it has been necessary to write a Mathematica package called "FormInt", that transforms an arbitrary Mathematica expression into FORM code, run FORM and transforms the result back into Mathematica code. The result is given back to the called function. Thus, every Mathematica function is independent and the intermediate result can be controlled in Mathematica by the user. This is different from FormCalc [123] that calculates everything in FORM at once. The procedure used here allows to control the calculation step by step and to insert or change Mathematica functions at any stage of the calculation.

Furthermore, a Mathematica package, called MathTeX was developed in order to make the intermediate and final results visible in a human readable way. The expressions are transformed into LaTeX code, that can be compiled to a postscript file. Here, a non-trivial task was to include automatically LaTeX-line-breaks in the expressions to end up with A4-postscript file that can be printed. However, matrix elements can become huge and for more than around 1000 A4-sheet MathTeX breaks down. Anyway, one easily can check the calculation of the few possibly problematic diagrams.

The resulting amplitude can be transformed by two further functions into Fortran code. In particular the Fortran functions are written in the convention of FormCalc. In particular the main function "SquaredME(...)" and the parameter definition file "model.h" are used. In this way, these results can be easily compared with those of FormCalc, if the same Fortran program for the numerical integration is used.

The developed program calculates polarized matrix elements with polarized external particles. The tensor integrals are decomposed using the Passarino-Veltman [126] (Appendix A.4) reduction and Dimensional Regularization [82–84] as well as Dimensional Reduction [87–89]. Traces over Dirac chains are simplified by appropriate routines

of FORM. The color-algebra is performed by a Mathematica function as described in Appendix A.5.

3.5.2 Numerical Calculation of Cross Sections

Fig. 3.6 shows a schematic configuration to calculate numerically cross sections using the program language Fortran. The program was written so that it can calculate differential and total cross sections for arbitrary scattering processes, restricted up to now to $2 \rightarrow 2$ and $2 \rightarrow 3$ reactions. The used formula were given in Section 3.4.

The program works as follow:
First of all, the parameters (scattering type, MSSM parameter etc.) are read from a data file. Then, one has to calculate for the chosen varying parameters (E_{cms}, M_S, ...) all masses and mixing angles of the SM and MSSM, coupling constants etc. To compute the MSSM variables, the routines of the "mssm_ini.F" file of FormCalc [123] version 3.0 has been used. To calculate the strong coupling constant, the function of the PDFLIB [73] was adopted. Moreover, for comparison, a routine of the fourth order formula given in [74] was implemented.
Then, the cross section is calculated using different integration routines. For the convoluted cross section, the density functions of the PDFLIB [73] are linked and laser-backscattering spectra are included. The squared matrix elements can be provided by the program described in the last section, FormCalc or "hand" implemented. This has been done for instance for the $e^+e^- \rightarrow \tilde{g}\tilde{g}$ scattering process. The evaluation of tensor integrals is done with the computer package LoopTools [123] based on FF [127, 128]. With the help of another function, it is possible to search for maximum values of the cross section and finally the results are printed with all used parameters into data files.
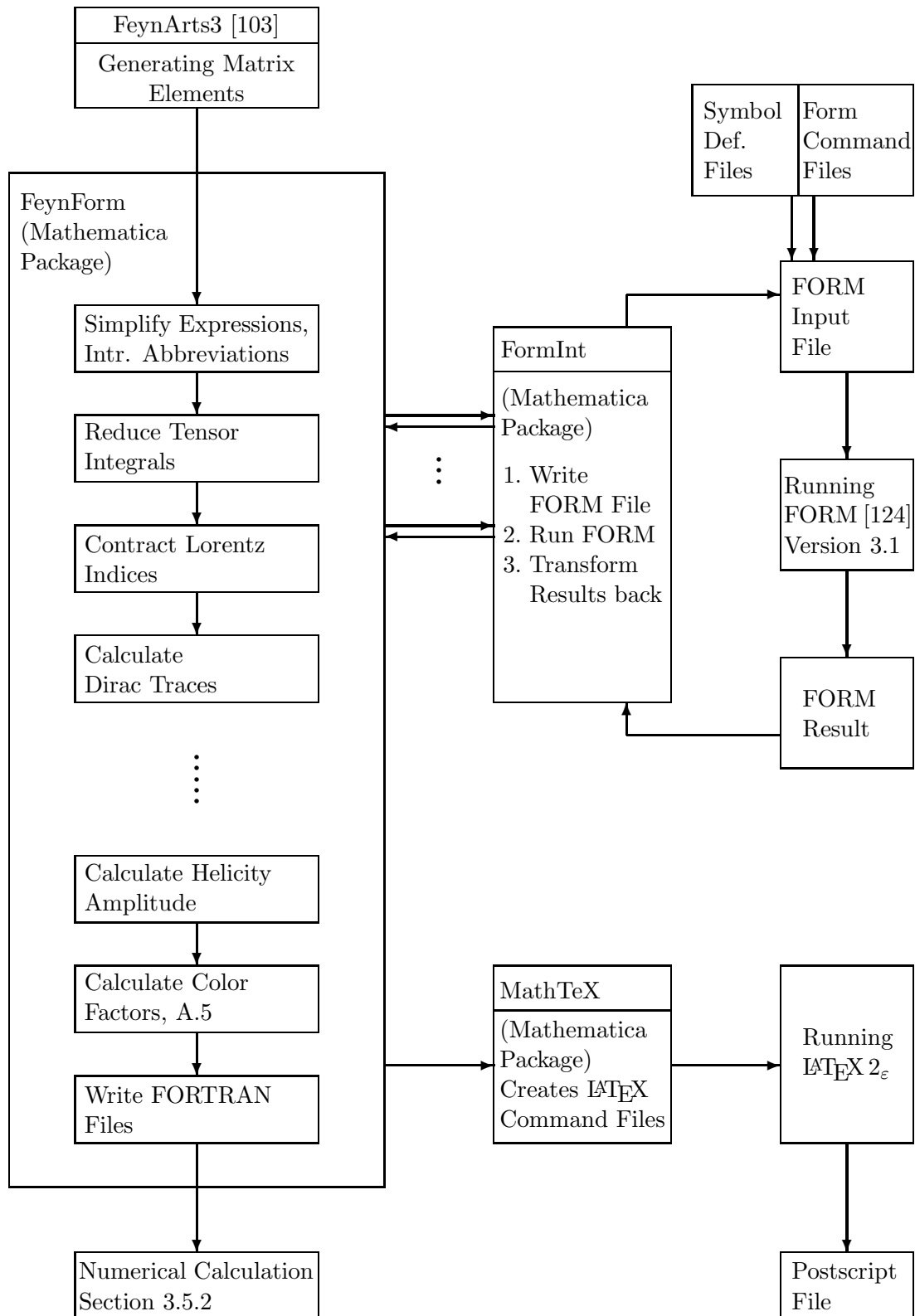
Figure 3.5: Schematic description of the analytic calculation of the FeynArts generated matrix elements using Mathematica and FORM.

Start

Numerics
(Main
Fortran
Program)

Read Parameter
to Fortran
Common Block

Parameter-
File of
Scattering
Process

Calculate SM and
MSSM Parameter

Density
Functions

Vary
the specified
Parameters
(Masses,
Energy, etc.)

Integration
Routines

Vegas[129]

qGauss[130]

Multigauss

⋮

Calculate
Differential
Coss
Section

PDFLIB[73]
Nucleon
Photon

Laser

Resolved

Polarization

⋯

Matrix
Elements

$e^+e^- \rightarrow \tilde{g}\tilde{g}$
$\gamma\gamma \rightarrow \tilde{g}\tilde{g}$
$q\bar{q} \rightarrow \tilde{g}\tilde{g}$
$\gamma\gamma \rightarrow \tilde{q}\tilde{q}^*$
$\gamma\gamma \rightarrow g\tilde{q}\tilde{q}^*$
⋮

Searching
for
Maxima

Create Result
File including
all used
Parameters

LoopTools
[123, 127,
128]

Resulting Data Files

Figure 3.6: Schematic description of the numeric calculation with Fortran.

Chapter 4

Gluino Pair Production in e^+e^- Annihilation

The Gluino pair production process in electron-positron annihilation and the Z^0-boson decay into gluino pairs have been considered by several groups [16–20]. Nevertheless, these calculations differ by a relative sign between the contributions given by the one-loop-vertex diagrams with two squarks and one quark and those given by the one-loop-diagram with one squark and two quarks. To get rid of this discrepancy, the complete process was recomputed in this thesis with three independent calculations and an agreement among them was found. The analytical results are given in Section 4.1 while the numerical ones are discussed in Section 4.2. The complete results have been published in [131].

4.1 Analytical Results

The symbolic gluino pair production process in electron positron annihilation is given by

$$e^-(p_1, \lambda_1)\, e^+(p_2, \lambda_2) \;\to \tilde{g}(k_1)\, \tilde{g}(k_2) \;,$$

where $p_{1,2}$ are momenta, $\lambda_{1,2} = \pm 1/2$ helicities of the incoming electrons/positrons, and $k_{1,2}$ the outgoing gluino momenta. The outgoing gluino helicity and color states are always summed up. Since the gluino as the superpartner of the gauge boson of the strong interaction couples neither directly to leptons nor to electroweak gauge bosons, the process occurs only at the one-loop level. The Feynman diagrams with s-channel photon or Z^0-boson exchange and triangular quark and squark loops are given in Fig. 4.1 . Higgs boson exchange is not considered due to the negligible small electron Yukawa coupling, but it would be relevant at muon colliders. Using the Feynman rules of [131], one can decompose the corresponding scattering amplitude into the lepton current L_μ^V, the propagator $iD_V^{\mu\nu}$ and the gluino current G_ν^V

$$\mathcal{M} = \sum_{V=\gamma, Z^0} L_\mu^V\, iD_V^{\mu\nu}(s)\, G_\nu^V \;, \tag{4.1}$$
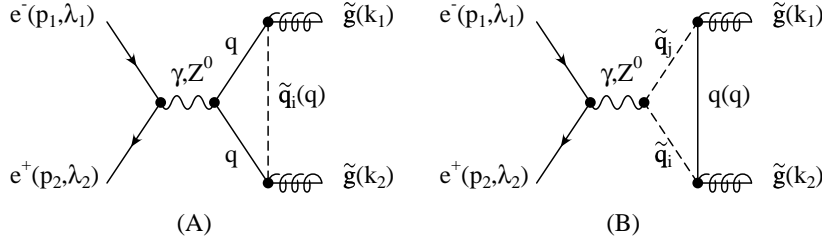
Figure 4.1: Feynman diagrams for gluino pair production in electron-positron annihilation. The exchanged photons and Z^0-bosons couple to the produced gluinos through triangular $qq\tilde{q}_i$ (A) and $\tilde{q}_i\tilde{q}_j q$ (B) loops with flavor flow in both directions.

where the connector V stands either for s-channel photon or Z^0-boson exchange. The lepton current is given by

$$L_\mu^V = \bar{v}(p_2, \lambda_2) \left[-ie\gamma_\mu(v_e^V - a_e^V \gamma_5)\right] u(p_1, \lambda_1),$$

where $-ie\gamma_\mu(v_f^V - a_f^V \gamma_5)$ is the gauge-boson-fermion-fermion coupling and

$$
\begin{aligned}
v_f^\gamma &= e_f , & a_f^\gamma &= 0 , \\
v_f^Z &= \frac{1}{2s_W c_W}\left(T_f^3 - 2e_f s_W^2\right) , & a_f^Z &= \frac{1}{2s_W c_W}T_f^3.
\end{aligned}
\tag{4.2}
$$

The photon and Z^0-boson propagators $iD_V^{\mu\nu}$ are defined as

$$iD_V^{\mu\nu}(s) = \frac{-ig^{\mu\nu}}{s - m_V^2 + i\eta} , \quad \text{with} \quad V = \gamma, Z^0 ,$$

which depend on the squared center-of-mass energy $s = (p_1 + p_2)^2 = (k_1 + k_2)^2$ and the gauge boson masses $m_{\{\gamma, Z^0\}} = \{0, m_{Z^0}\}$. The gluino current of both flavor flow direction of the diagrams (A) and (B) can be written in a compact form

$$
\begin{aligned}
G_\nu^V = -e\, \bar{u}^a(k_2) \sum_q &\left[\sum_{i=1}^2 \left(i\Gamma_{i,1}^a \hat{A}_\nu^{i,V} i\Gamma_{i,2}^b + i\Gamma'^{\,a}_{i,2}\tilde{A}_\nu^{i,V} i\Gamma'^{\,b}_{i,1}\right) \right. \\
&\left. + \sum_{i,j=1}^2 \left(i\Gamma_{i,1}^a \Gamma^{ij,V}\hat{B}_\nu^{ij,V} i\Gamma_{j,2}^b + i\Gamma'^{\,a}_{i,2}\Gamma^{ji,V}\tilde{B}_\nu^{ij,V} i\Gamma'^{b}_{j,1}\right) \right] v^b(k_1) .
\end{aligned}
\tag{4.3}
$$

Here $\{i, j\}$ indicates the squark mass eigenstates, $\{a, b\}$ are the color indices of the SU(3) that have to be summed up (Section A.5), and $\Gamma' = C\Gamma^T C^{-1}$ (A.5), with C charge conjugation matrix (A.4). The $\sum_q$ runs over all flavors q={u, d, c, s, t, b}, whereby the dependence of Γ, $\hat{A}$, $\tilde{A}$, $\hat{B}$, $\tilde{B}$ on q was suppressed for better readability. $\Gamma^{ij,V}$ is determined by the gauge-boson-squark-squark coupling $-ie(p-p')_\nu \Gamma^{ij,V}$ where

$$\Gamma^{ij,\gamma} = e_q \delta_{ij} \quad \text{and} \quad \Gamma^{ij,Z^0} = \frac{1}{s_W c_W}\left((T_q^3 - e_q s_W^2)U_{j1}U_{i1}^* - e_q s_W^2\, U_{j2}U_{i2}^*\right). \tag{4.4}$$

Squark mixing is always allowed and given by the mixing matrices U_{ij} (2.6). The quark-squark-gluino coupling in equation (4.3) is

$$i\Gamma_{i,1}^a = -i\sqrt{2}g_s\, T^a(U_{i1}\,\omega_L - U_{i2}\,\omega_R) \quad \text{and} \quad i\Gamma_{i,2}^a = -i\sqrt{2}g_s\, T^a(U_{i1}^*\,\omega_R - U_{i2}^*\,\omega_L) ,$$

with $\omega_{L,R}$ projectors (A.2), and T^a SU(3) generators (Section A.5).
In equation (4.3) the tensors $\hat{A}$ and $\tilde{A}$ refer to the diagram (A) of Fig. 4.1. $\hat{A}$ is given by

$$\hat{A}_\nu^{i,V} = \int \frac{\mathrm{d}^D q}{(2\pi)^D} \mu^{4-D} \frac{(\slashed{q} + \slashed{k}_2 + m_q)\,\gamma_\nu\,(v_q^V - a_q^V \gamma_5)\,(\slashed{q} - \slashed{k}_1 + m_q)}{(q^2 - m_{\tilde{q}_i}^2 + i\eta)[(q-k_1)^2 - m_q^2 + i\eta][(q+k_2)^2 - m_q^2 + i\eta]},$$

while one obtains $\tilde{A}$ from the diagram with reversed flavor flow replacing v_q^V with $-v_q^V$, symbolically $\tilde{A}_\nu^{i,V} = \hat{A}_\nu^{i,V}(v_q^V \to -v_q^V)$, v_q^V, a_q^V being defined in equation (4.2).
The contribution from diagram (B) in Fig. 4.1 is

$$\hat{B}_\nu^{ij,V} = \int \frac{\mathrm{d}^D q}{(2\pi)^D} \mu^{4-D} \frac{(\slashed{q} - m_q)\,(2q - k_1 + k_2)_\nu}{(q^2 - m_q^2 + i\eta)[(q-k_1)^2 - m_{\tilde{q}_j}^2 + i\eta][(q+k_2)^2 - m_{\tilde{q}_i}^2 + i\eta]}$$

and $\tilde{B}_\nu^{ij,V}$ is determined from the diagram with reversed flavor flow identifying $\tilde{B}_\nu^{ij,V} = -\hat{B}_\nu^{ij,V}$.

The matrix element (4.1) can be simplified using the Dirac equation (A.3), the anti-commutation relations for Dirac matrices (A.1), and the tensor loop integrals of Section A.4. Then, the gluino current (4.3) reduces to

$$G_\nu^V = ie\frac{\alpha_s}{2\pi}\frac{\delta^{ab}}{2}\,\bar{u}^a(k_2)\,\gamma_\nu\gamma_5\,v^b(k_1)\sum_q (A_q^V + B_q^V)\,. \tag{4.5}$$

The sum of the contributions of the diagrams (A) and (B) with both flavor flows can be expressed as follows

$$A_q^V = \sum_{i=1}^2 \Big[C_0^{qi}(m_q^2 a_{qiV}^- - m_{\tilde{g}}^2 a_{qiV}^+ + 2m_q m_{\tilde{g}} \hat{a}_{qiV}) + C_1^{qi}4m_{\tilde{g}}(m_q \hat{a}_{qiV} - m_{\tilde{g}} a_{qiV}^+)$$
$$+ C_{00}^{qi}(2-D)\,a_{qiV}^+ - C_{11}^{qi}2m_{\tilde{g}}^2 a_{qiV}^+ + C_{12}^{qi}\left(s - 2m_{\tilde{g}}^2\right)a_{qiV}^+\Big]\,,$$
$$B_q^V = \sum_{i,j=1}^2 C_{00}^{qij}2b_{qijV}\,, \tag{4.6}$$

where the indices i, j again specify the squark mass eigenstates and the arguments of the infrared finite three-point tensor integrals are $C_{k(l)}^{qi} = C_{k(l)}(m_{\tilde{g}}^2, s, m_{\tilde{g}}^2, m_{\tilde{q}_i}^2, m_q^2, m_q^2)$ and $C_{00}^{qij} = C_{00}(m_{\tilde{g}}^2, s, m_{\tilde{g}}^2, m_q^2, m_{\tilde{q}_j}^2, m_{\tilde{q}_i}^2)$. Note that for diagram (A) holds the relations $C_1^{qi} = C_2^{qi}$ and $C_{11}^{qi} = C_{22}^{qi}$ due to the two equal squark masses in the loop.
The coefficients $a^\pm$, $\hat{a}$, b in equation (4.6) depend on the squark mixing matrix U_{ij}^q, v_q^V and a_q^V (4.2), and $\Gamma^{ij,V}$ (4.4) being defined as

$$a_{qiV}^\pm = v_q^V\left(U_{i1}^q U_{i1}^{q*} - U_{i2}^q U_{i2}^{q*}\right) \pm a_q^V\,,$$
$$\hat{a}_{qiV} = a_q^V\left(U_{i1}^q U_{i2}^{q*} + U_{i2}^q U_{i1}^{q*}\right)\,,$$
$$b_{qijV} = U_{i1}^q U_{j1}^{q*}\,\Gamma^{ij,V} - U_{i2}^{q*} U_{j2}^q\,\Gamma^{ji,V}\,. \tag{4.7}$$

By adding A_q^V and B_q^V in (4.5), the ultraviolet singularities contained in the C_{00}-functions cancel for each flavor separately in $D = 4 - 2\varepsilon$ dimensions. This was checked explicitly for arbitrary unitary complex mixing matrices U.

In order to determine which contributions are more relevant for the cross section, Equation (4.7) can be rewritten using the properties of the 2×2 unitary matrix U (2.6). It can additionally be rewritten for real mixing matrices (2.7). Eventually one has

$$
\begin{aligned}
a_{qiV}^{\pm} &= (-1)^i \, v_q^V \left(U_{12}^q U_{12}^{q*} - U_{11}^q U_{11}^{q*} \right) \pm a_q^V = (-1)^i \, v_q^V \left(s_{\theta_{\tilde q}}^2 - c_{\theta_{\tilde q}}^2 \right) \pm a_q^V \;, \\
\hat{a}_{qiV} &= (-1)^{i-1} \, a_q^V \, 2\mathrm{Re}\{ U_{11}^q U_{12}^{q*} \} = (-1)^{i-1} \, a_q^V \, 2 s_{\theta_{\tilde q}} c_{\theta_{\tilde q}} \;, \\
b_{qiiV} &= (-1)^i \left(U_{12}^q U_{12}^{q*} - U_{11}^q U_{11}^{q*} \right) \Gamma^{ii,V} = (-1)^i \left(s_{\theta_{\tilde q}}^2 - c_{\theta_{\tilde q}}^2 \right) \Gamma^{ii,V} \;, \\
b_{q12V} = b_{q21V} &= U_{11}^q U_{21}^{q*} \Gamma^{12,V} + U_{11}^{q*} U_{21}^q \Gamma^{21,V} = -2 s_{\theta_{\tilde q}} c_{\theta_{\tilde q}} \Gamma^{12,V} \;.
\end{aligned}
\tag{4.8}
$$

In case of photon exchange, from equation (4.8) with the help of equation (4.4), one can read of the following relations for squark mass eigenstates 1 and 2 :

$$
a_{q1\gamma}^{\pm} = -a_{q2\gamma}^{\pm} \;, \qquad \hat{a}_{qi\gamma} = 0 \;, \qquad b_{q11\gamma} = -b_{q22\gamma} \;, \qquad b_{q12\gamma} = b_{q21\gamma} = 0 \;.
$$

This even holds in the case of complex mixing matrices U. Summing over the squark mass eigenstates 1 and 2 in equation (4.6), the gluino current given in equation (4.5) will vanish for each flavor separately if the squark mass eigenstates 1 and 2 are degenerated $m_{\tilde q_1} = m_{\tilde q_2}$. In many unification scenarios, this condition is nearly fulfilled for the first and second generation of quarks. Thus, only the third generation gives large contributions to the cross section. In addition, one can have large squark mixing with mixing angle around $45°$. In this case as well, the factors $a_{qiV}^{\pm}$ and b_{qiiV} will vanish because $\left(s_{\theta_{\tilde q}}^2 - c_{\theta_{\tilde q}}^2 \right) \to 0$. Therefore, the contribution from photon exchange is suppressed in most cases and will be significant only for moderate mixing angles and for $|M_{\tilde f_L}^2 - M_{\tilde f_R}^2| \gg 0$ (see equation (2.8)), that means $|m_{\tilde f_L}^2 - m_{\tilde f_R}^2| \gg 0$.

For the Z^0-boson exchange similar relations hold for real mixing matrices:

$$
\begin{aligned}
a_{q1Z^0}^{\pm} &= -a_{q2Z^0}^{\pm} \pm 2 a_q^{Z^0} \;, & \hat{a}_{q1Z^0} &= -\hat{a}_{q2Z^0} \;, \\
b_{\{q11Z^0, q22Z^0\}} &= \{ c_{\theta_{\tilde q}}^2, s_{\theta_{\tilde q}}^2 \} a_q^{Z^0} - e_q \frac{s_W}{c_W} \;, & b_{q12Z^0} = b_{q21Z^0} &= -2 s_{\theta_{\tilde q}} c_{\theta_{\tilde q}} \, a_q^{Z^0} \;,
\end{aligned}
$$

where this bracket notation relates $c_{\theta_{\tilde q}}^2$ to b_{q11Z^0} and $s_{\theta_{\tilde q}}^2$ to b_{q22Z^0}. If the squark masses of a given flavor are degenerated only the terms proportional to $a_q^{Z^0}$ and e_q contribute to the cross section. Furthermore, for up and down type quarks of the same generation yields $a_u^{Z^0} = -a_d^{Z^0}$ and for the charge $e_u = -2e_d$. Thus, the up and down contributions of one generation add destructively and become very small if the quark masses are equal: $m_u \approx m_d$. Since these conditions are fulfilled for the first two generations of quarks, only the third generation with top and bottom quarks will dominate the cross section in the scenario with $M_{\tilde f_L}^2 \approx M_{\tilde f_R}^2$.

Squaring the matrix element (4.1) and integrating it over the phase space[1], one obtains the total cross section for electron-positron annihilation into gluino pairs, given by

$$\sigma_{\lambda_1\lambda_2}(s) = \frac{\alpha_e^2\alpha_s^2(N_C^2-1)\beta^3 s}{24\pi} \sum_{V_1,V_2}\left[\frac{Q_{\lambda_1\lambda_2}^{V_1V_2}}{(s-m_{V_1}^2)(s-m_{V_2}^2)}\sum_q(A_q^{V_1}+B_q^{V_1})(A_q^{V_2}+B_q^{V_2})^*\right],$$

(4.9)

where V_1, V_2 runs over the intermediate bosons γ and Z^0, and the color factor is $N_C = 3$. From the expression of the lepton tensor $L_{\mu\nu}^{V_1V_2} = L_\mu^{V_1}L_\nu^{V_2}$, one can derive the factor

$$Q_{\lambda_1\lambda_2}^{V_1V_2} = (v_e^{V_1}v_e^{V_2}+a_e^{V_1}a_e^{V_2})(1-4\lambda_1\lambda_2)-(v_e^{V_1}a_e^{V_2}+v_e^{V_2}a_e^{V_1})(2\lambda_1-2\lambda_2),$$

that contains the cross section dependence on the helicities of the initial electron and positron. The total cross section (4.9) presents the expected factor β^3, $\beta = \sqrt{1-4m_{\tilde{g}}^2/s}$ being the gluino velocity for a P-wave production from two spin-1/2 fermions with an intermediate spin-1 boson [16].

The angular distribution in the center-of-mass system with scattering angle θ is given by

$$\frac{d\sigma_{\lambda_1\lambda_2}}{d\Omega}(s) = \frac{3}{8\pi}(1+\cos^2\theta)\sigma_{\lambda_1\lambda_2}(s) \ .$$

It is important to note that the angular distribution is independent of the gluino mass as in the case of massless fermions [16]. This is due to the Majorana nature of the two final states that must be odd under exchange. Thus, if one is able to measure the angular distribution, one can determine the spin and Majorana nature of the gluinos.

The above mentioned result was calculated analytically by hand and implemented into the Fortran program described in Section 3.5.2. The obtained cross sections were compared numerically with the results of the automatic calculation described in Section 3.5.1. In addition, a numerical comparison with the results of FormCalc [123] version 3.2 has be performed. The numerical results of the three different calculations agreed up to 15 digits. The only possible error source could be the fact that in all calculations the Feynman diagrams have been generated with the package FeynArts [103] version 3.2 with the MSSM model-file [101] and that the gluino Majorana nature has always been treated as given in [132]. However, the consistency of the Feynman rules were compared with [65] and the treatment of the Majorana nature studied carefully.

In literature one finds different results for the gluino pair production process. The most detailed calculation is given in [17] for the case of real squark mixing matrices. The unpolarized cross section is given through the averaged sum over all helicity combinations ($\lambda_{1,2} = \pm 1/2$) of the initial electron and positron as $\sigma(s) = \frac{1}{4}\sum\sigma_{\lambda_1\lambda_2}(s)$. The result for diagram A agrees with Eq. (4.5) in [17], if one identifies

$$\begin{aligned}
C_0^{qi} &= -F_{qqi}^{00}\ , & C_1^{qi} &= +F_{qqi}^{01}\ , \\
C_{00}^{qi} &= -G_{qqi}/2\ , & C_{11}^{qi} &= -F_{qqi}^{02}\ , & C_{12}^{qi} &= -F_{qqi}^{11}
\end{aligned}$$

---

[1]Note that the scattering angle θ has to be integrated only from 0 to $\frac{\pi}{2}$ because of the identical particles in the final state. Alternatively one can integrate as usual from 0 to π and multiply by 1/2.

and reverses the sign of $\hat{b}_q$ to account for the opposite conventions of the squark mixing matrix

$$U_{\tilde{q}} = \begin{pmatrix} \cos\theta_{\tilde{q}} & -\sin\theta_{\tilde{q}} \\ \sin\theta_{\tilde{q}} & \cos\theta_{\tilde{q}} \end{pmatrix} .$$

If for the result of diagram B one identifies

$$C_{00}^{qij} = -G_{ijq}/2 ,$$

the μ dependence of the G integrals in Eq. (4.5) of [17] cancels for each flavor. However, the result would disagree with Eq. (4.5) of [17] by a relative minus sign between diagram A and B. If the sign of diagram B is as in [17], the ultraviolet singularities cancel only after adding the contributions from the two weak isospin partners with opposite sign of T_q^3.

The reason of this discrepancy seams to be the Feynman rules given in [17]. The Z^0-boson coupling to quarks differs by a relative minus sign to the Feynman rules of this thesis and those of [65] in the limit of no squark mixing. On the other hand, the Feynman rules agree for Z^0-boson coupling to squarks. Thus, writing down the gluino current in the notation of [17] but using the Feynman rules of this thesis, one obtains the gluino current for diagram A given in equation (2.4) of [17] but with a relative minus sign to equation (2.10) of [17], that represents diagram B.

Furthermore, the results of this thesis agree with [18], who found that the ultraviolet singularities cancel separately for each weak isospin partner, so that there is no anomaly. This had also been claimed previously by [19]. Eventually, the results of this thesis disagree by a relative minus sign between diagram A and B with [20], who has performed the calculation in the limit of vanishing gluino mass.

4.2 Numerical Results

The analytical results presented in the previous Section have been evaluated with the Fortran programs described in Section 3.5.2. Numerical agreement with the computer algebra program FormCalc [101] version 3.2 was found up to 15 digits. The calculations were performed using the parameters in Section 2.4 and the effective electromagnetic coupling $\alpha = 1/127.934$.

The cross section of $e^+e^- \to \tilde{g}\tilde{g}$ scattering process depends on the gluino mass, the fermion masses and the sfermion sector (Section 2.3.6). As discussed in the previous Section, to obtain a large cross section one needs a large splitting between the squark mass eigenstates $\tilde{q}_1$ and $\tilde{q}_2$. Thus, in the following discussion two cases are considered:

1. An universal mass parameter $M_S = M_{\tilde{f}_L} = M_{\tilde{d}_R}$ is used for all flavor f. A large splitting of the mass eigenstates is reached only in the third generation by large mixing angles of the top and bottom squarks.

2. One sets $M_S \neq M_{\tilde{f}_L} \neq M_{\tilde{d}_R}$. In this case the mixing angle of the squark is of minor importance.

In the first case the parameter M_S and the mixing angle have been varied looking for the largest value of the cross section. $\tan\beta$ was set to 10 because the direct dependence of the squark masses on $\tan\beta$ is small.

A gluino mass limit of $m_{\tilde{g}} \geq 200$ GeV and squark mass limit of $M_S \gtrsim 325$ GeV were taken from CDF [75] and D0 [76]. As the loops in the Feynman diagrams contain squarks and quarks, σ becomes larger for smaller squark masses. However, the top squark mass has a lower limit (see Section 2.4). The value $\theta_{\tilde{t}} = 45.195°$ was chosen leading to $m_{\tilde{t}_1} = 110.52$ GeV and $m_{\tilde{t}_2} = 505.69$ GeV. Fig. 4.2 shows the cross section
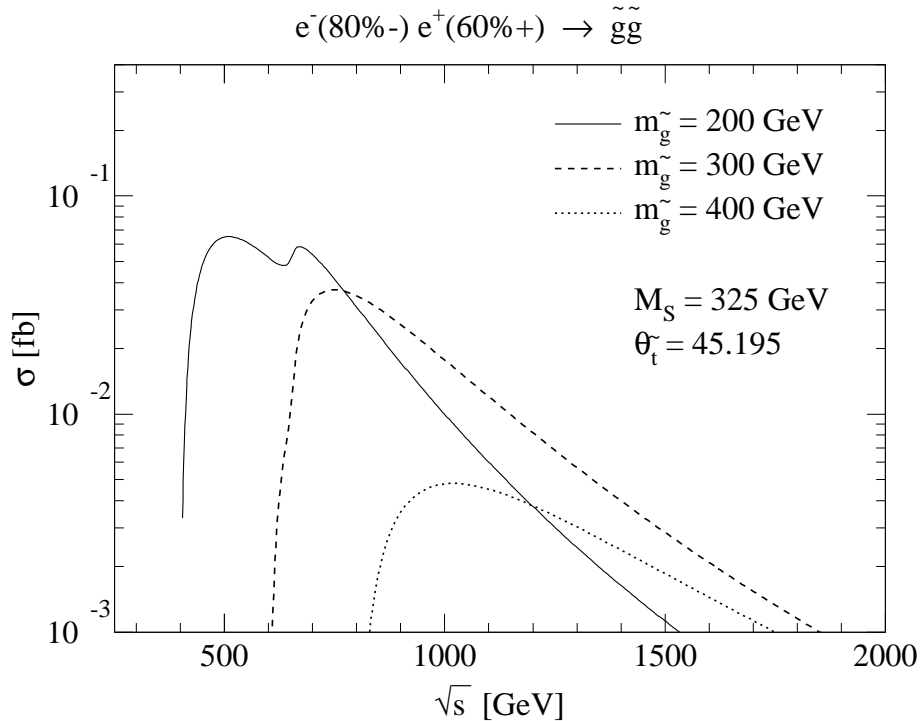
Figure 4.2: Center-of-mass energy dependence of the polarized $e^+e^- \rightarrow \tilde{g}\tilde{g}$ cross section for various gluino masses and maximal top squark mixing ($\tan\beta = 10$, $\theta_{\tilde{b}} = 0°$).

dependence on the center-of-mass energy for various gluino masses. The polarization of the initial electron and positron is 80%(-) and 60%(+), respectively. The cross section rises proportionally to β^3 (equation (4.9)) for a P-wave production of the gluino pairs and after reaching a maximum it drops off like $1/s$ because of the intermediate photon and Z^0-boson propagator. The local minima at 630 GeV of the solid line ($m_{\tilde{g}} = 200$ GeV) arises for loops including top squarks. Due to the large top squark mixing angle, the $\tilde{t}_1$-squark is very light and $\tilde{t}_2$ relatively heavy. The cross section rises faster for diagrams with two internal $\tilde{t}_1$ than for diagrams with a $\tilde{t}_1$-$\tilde{t}_2$ pair and faster for diagrams with two internal $\tilde{t}_2$-squarks. For all three contributions exists a maxima after that the cross section drops down. Because of the destructive interference of the different Feynman diagrams the local minima arises. The maximum cross section that
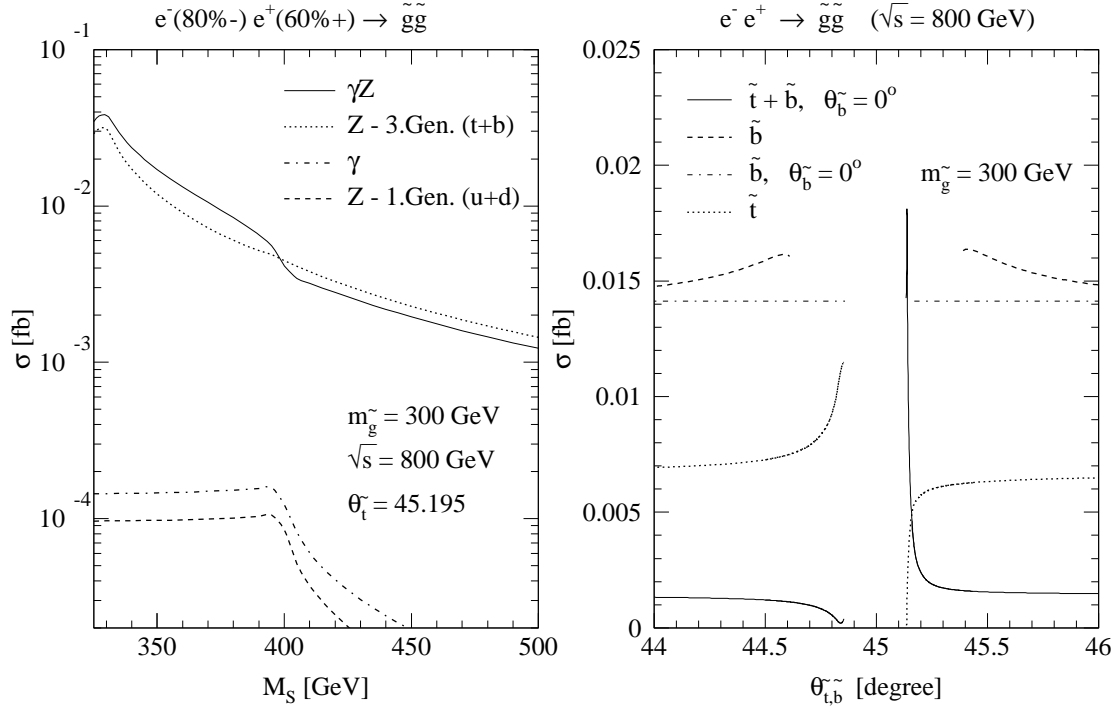
Figure 4.3: $(\tan\beta = 10)$; Left: Contribution of diagrams with virtual γ and Z^0-boson exchange to the unpolarized $e^+e^- \to \tilde{g}\tilde{g}$ cross section for non mixing squarks. Right: $(M_S = 400 \text{ GeV})$ Large mixing effects of top and bottom quark loops to the unpolarized cross section, $\sigma \approx \sigma(Z^0-\text{exchange})$. The central region with maximal top/bottom squark mixing is excluded by the mass limits.

can be reached with the given mass bounds is around 0.065 fb for light gluino masses of 200 GeV and a light top squark mass with large stop splitting. With a luminosity of $1000\,fb^{-1}$ per year only 65 events are expected, which is quite small. For a gluino mass of 300 GeV only 30 events of gluino pairs will be produced. The following discussion for $m_{\tilde{g}} = 300$ GeV shows that the cross section become invisible for the most ranges of MSSM parameter space (The case of $m_{\tilde{g}} = 200$ GeV is discussed in [131]). Therefore, a measurement of gluino pairs seems impossible in electron positron annihilation.

The reason of the cross section smallness is principally the fact that the process takes place only at one-loop level. However, the destructive interference of the different loop contributions discussed in the last Section is important as well. The M_S dependence of the polarized cross section for for large top squark mixing is shown in the left panel of Fig. 4.3. For $M_S = M_{\tilde{f}_L} = M_{\tilde{f}_R}$ the contribution from photon-exchange (dot-dashed line) is strongly suppressed, since the loop contributions of squark 1 and squark 2 of each flavor cancel each other. This suppression is of two orders of magnitude. The same happens for the first two generations in case of Z^0-exchange (dashed line) because $m_{\tilde{f}_L} \approx m_{\tilde{f}_R}$. Only in the top squark sector one has a larger difference between $m_{\tilde{t}_L}$ and $m_{\tilde{t}_R}$, also in the case of no mixing, due to the large top quark mass (dotted line).
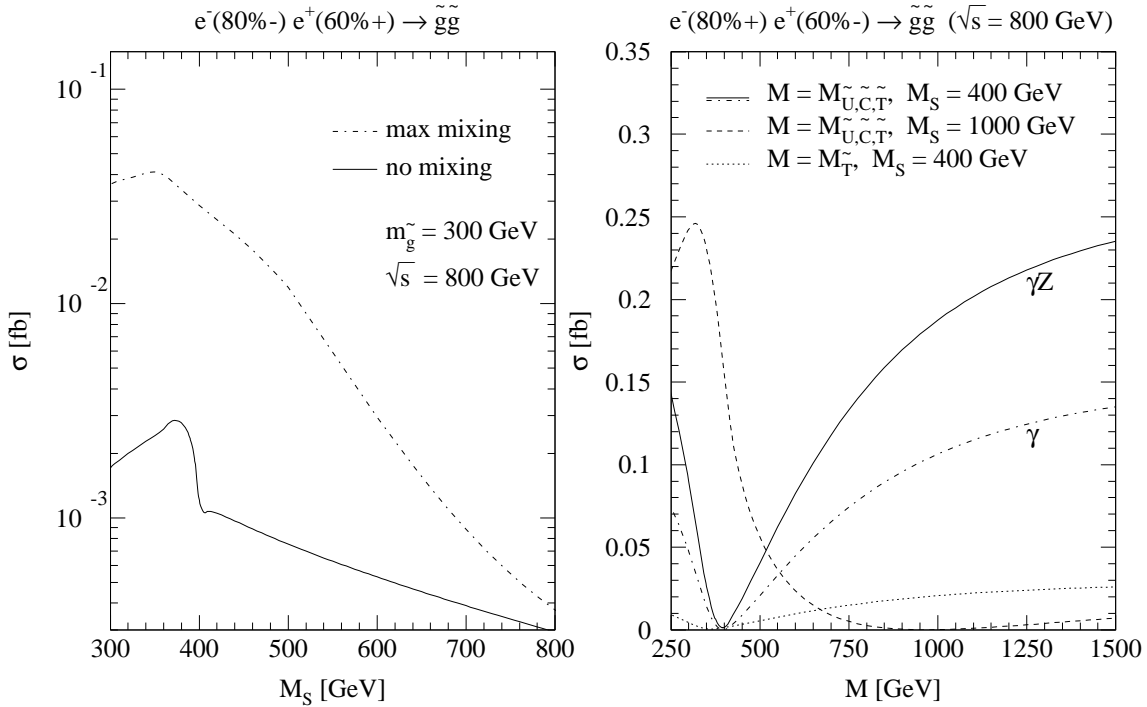
Figure 4.4: ($m_{\tilde{g}} = 300\,\text{GeV}$, $\tan\beta = 10$, f stands for all quark flavor, u for all up quarks, d for all down quarks); Left: Total $e^+e^- \to \tilde{g}\tilde{g}$ cross section in dependence of a universal $M_S = M_{\tilde{f}_L} = M_{\tilde{f}_R}$ for no mixing and maximal squark mixing. Right: Total cross section for $M_S = M_{\tilde{f}_L} = M_{\tilde{d}_R} \neq M_{\tilde{u}_R}$. For the dotted curve only the top squark parameter $M_{\tilde{t}_R}$ is not equal M_S. Apart from the dot-dashed line (only $\gamma-$exchange) all Feynman diagrams (γZ^0) contribute.

In supersymmetric theories many normal and anomalous thresholds can occur due to the large number of particles (see e.g. [133] and reference therein). The dot-dashed line (γ) and dashed line ($Z - u, d$) have a normal threshold around $M_S = 400$ GeV. This threshold arises for vertex diagrams with two internal squarks (Fig. 4.1) where the squark masses of the five light flavors are about M_S. The squark pairs can not be produced on-shell for larger M_S than 400 GeV leading to the strong decrease of the cross section.

The destructive interference of the contributions from up and down quark of each generation is displayed in the right panel of Fig. 4.3. Here, the cross section dependence on the top and bottom squark mixing is shown. Choosing a stop mixing angle near 45 degree the stop mixing becomes large, leading to a light stop 1 of $\mathcal{O}(100\,\text{GeV})$. The bottom contribution (dashed line) is larger than the top contribution (dotted line) and both of them vary strongly for large mixing angle. As a consequence of the destructive interference, the sum of both contributions (solid line) rises if the top contribution decreases and can be even higher than the bottom contribution due to large imaginary parts in the matrix element. Although the distribution shown here is the complicated

sum in equation (4.6) with the coefficients (4.7), the destructive interference in the small mixing case is always obvious.

The cross section in Fig. 4.3 (right plot) rises steeply close to 45 degree. The reason is the choice of MSSM parameters, for which only in this region large stop mass splitting occur. This becomes evident in equation (2.9). If $M_{\tilde{q}_L} = M_{\tilde{q}_R}$ large mass splitting can be obtained only if the non-diagonal entries of the mixing matrix, $(A_q - \mu^* \{\cot\beta, \tan\beta\})$, become large (equation (2.8)). However, in that case the numerator of equation (2.9) is large too, while the denominator is small. To fulfill equation (2.9) mixing angles near 45 degrees are required.

Because of the squarks inside the loop diagrams, the cross section depends on the squark masses and drops off for large squark masses as shown in the left plot of Fig. 4.4. Varying M_S from 325 GeV to 800 GeV the cross section for non mixing squarks (solid line) decreases from $2 \cdot 10^{-3}$fb to $3 \cdot 10^{-4}$ fb. Again the normal threshold for loops containing two squarks of the light flavors around $M_S = 400$ GeV for $\sqrt{s} = 800$ GeV is visible. For the dot-dashed line of maximal mixing the bottom squark mixing angle was kept fixed to $\theta_{\tilde{b}} = 0°$ and the top squarks mixing angle varied to search for large cross section. As shown, σ depends strongly on the top squarks mixing for $M_S \leq 800$ GeV.

If $\theta_{\tilde{t}} \leq 45°$ the cross section can also be much smaller than in the non-mixing case, as plotted in the right panel of Fig. 4.3. This means, that "large" cross sections as in Fig. 4.2 and the number of 65 events per year are highly optimistic values, which can be reached only in a very small parameter space. With high probability the gluino pair production in e^+e^- scattering can not be observed for $M_S = M_{\tilde{f}_L} = M_{\tilde{f}_R}$.

In case of $M_S \neq M_{\tilde{f}_L} \neq M_{\tilde{f}_R}$ the contributions of squark mass eigenstate 1 and 2 do not cancel each other to zero, even for γ-exchange. The cross section becomes considerably larger for each flavor. The up and down quark contributions of each generation still interfere destructively. This happens also for the γ-exchange because of the opposite sign of the quark charges. Thus, in order to reach a large difference, one should vary the mass parameter of only one flavor in each generation ($M_{\tilde{u}_L} \neq M_{\tilde{u}_R}$) and keep the other one fixed ($M_{\tilde{d}_L} = M_{\tilde{d}_R}$) or vice versa. Since the squared matrix elements are proportional to e_q^2, the left and right mass parameters of the down type quarks are kept fixed and those of the up type quarks are varied.

The resulting cross sections for non-mixing squarks are shown in the right plot of Fig. 4.4. For the solid line the parameters $M_{\tilde{u}_R}$, $M_{\tilde{c}_R}$, $M_{\tilde{u}_R}$ are varied simultaneously while all other mass parameters M are equal to 400 GeV. As already discussed, the cross section vanishes for all flavors if $M_{\tilde{f}_L} = M_{\tilde{f}_R} = 400$ GeV, and the cross section rises for increasing differences $|M_{\tilde{f}_L} - M_{\tilde{f}_R}| \gg 0$. This is also visible for $M_S = 1000$ GeV (dashed line). Since for such large mass differences the top quark mass plays a minor role, all three generation contribute equally. If only $M_{\tilde{t}_R}$ is varied (dotted line), the cross section is much smaller for the same parameters. In conclusion, the photon exchange and the γZ^0 interference term contributes mainly to the cross section (dot-dashed line) while the Z^0-boson contribution remains small.

Chapter 5

Gluino Pair Production in Photon-Photon Collisions

In this chapter the gluino pair production process in photon-photon collisions is discussed. For the scattering process high energetic photons are produced by laser-backscattering (Chapter 3). Since gluinos interact only strongly and photons only electro-magnetically, the $2 \to 2$ scattering process starts at one loop level. The process is described in the next section. Furthermore, gluino pairs can be produced at resolved processes, which are an effective description for multi-particle final states, where only the gluino pairs are visible in the detector. This scattering type is discussed in Section 5.2, and the complete process has been published in [134].

The gluino pair production in photon-photon collision was considered in [135]. However, they neglected diagrams with two and three internal squarks. For very light gluinos of mass $m_{\tilde{g}} = 5...25$ GeV, squarks of mass 50...150 GeV, the shapes and magnitudes (in pb, not nb) of the threshold behavior in Fig. 2 of Ref. [135] can roughly be reproduced. For a more detailed numerical comparison, more information on the quark charges and coupling constants used there would be needed.

5.1 Direct Pair Production Process

The generic gluino pair production process in photon-photon scattering is given as

$$\gamma(p_1, \lambda_1)\, \gamma(p_2, \lambda_2) \ \to \tilde{g}(k_1)\, \tilde{g}(k_2)$$

where $p_{1,2}$ are momenta and $\lambda_{1,2} = \pm 1$ helicities[1] of the incoming photons, and $k_{1,2}$ the outgoing gluino momenta. The outgoing gluino helicities and color states are always summed up. As mentioned above, the process can not occur at tree level. The Feynman diagrams at one-loop level are all of box-type and they are displayed in Fig. 5.1. The loops contain quarks of all flavors and their corresponding supersymmetric partners,

---

[1]The polarization is chosen to be circular because large gluino masses are considered. In this case one needs large center-of-mass energies of the backscattered photons.
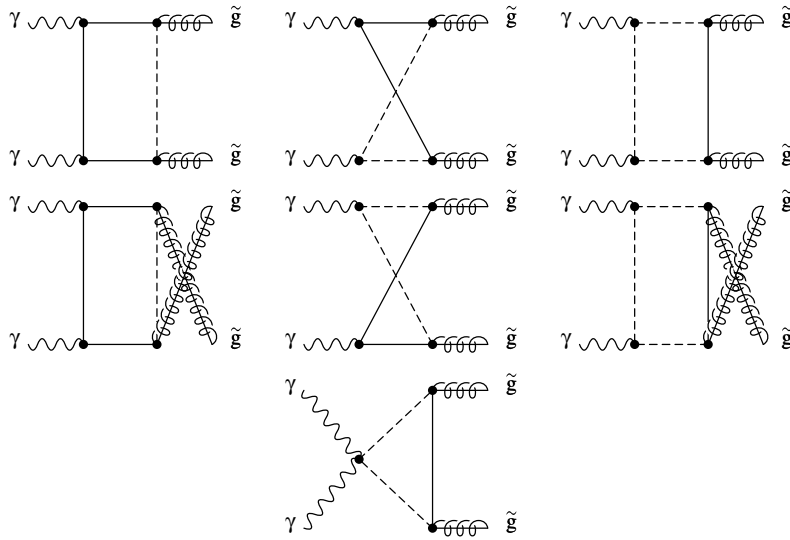
Figure 5.1: Feynman diagrams for gluino pair production in direct photon-photon collisions. The solid lines indicate quarks and the dashed lines the corresponding squarks 1 or 2. Inside the loops the flavor flows in both directions.

where the solid lines indicates the quarks and the dashed lines the squarks. The fermionic flavor inside the loops can be clock- and anti-clockwise. Mixing between the squark eigenstates $\tilde{q}_L$ and $\tilde{q}_R$ to the mass eigenstates $\tilde{q}_1$ and $\tilde{q}_2$ is always allowed. Thus, to calculate the scattering matrix element one has to sum over the 6 flavors $q = \{u, c, t, d, s, b\}$, the two squark mass eigenstates $i = 1, 2$ and the two flavor flow directions:

$$\mathcal{M}_{\gamma\gamma} = \sum_q \sum_{i=1}^{2} \left(\mathcal{M}_{t1} + \mathcal{M}_{u1} + \mathcal{M}_{t2} + \mathcal{M}_{u2} + \mathcal{M}_{x2} + \mathcal{M}_{t3} + \mathcal{M}_{u3} \right)$$
$$+ \left(\omega_+ \leftrightarrow \omega_- , \, S_{ij}^{\tilde{q}} \leftrightarrow S_{ij}^{\tilde{q}\,\dagger} \right). \tag{5.1}$$

Polarizations of the external particles were suppressed, and the indices 1-3 in $\mathcal{M}_{t1}$, $\mathcal{M}_{t2}$, etc. refer to the number of internal squark lines. The analytical form of the matrix elements can be generated with help of the computer package FeynArts [103], version 3.2 and the MSSM model file [101]. A compact form of the seven generic matrix elements is given in [134]. The second term in equation (5.1) denotes the corresponding diagrams with opposite flavor flow. They are obtained by interchanging the projectors $\omega_+ \leftrightarrow \omega_-$ (A.2) and the mixing matrix entries $U_{ij}^{\tilde{q}} \leftrightarrow U_{ij}^{\tilde{q}\,*}$ (2.6).

The matrix elements (5.1) are simplified using the Dirac equation (A.3) and the anti-commutation relations for Dirac matrices (A.1). Due to the three quarks inside the loops, tensor integrals up to $D^{\mu\nu\rho}$ (A.8) occur that have to be reduced to scalar integrals as given in Section A.4. All the tensor integrals are free of ultraviolet divergences and, since there are only massive particles inside the loops, they are also IR finite.

If one writes the matrix elements of Fig. 5.1 as given in [134] one has 7 different generic matrix elements plus seven for the flavor reversed ones. Due to the maximal number of

3 internal quarks, these matrix elements contain long fermion chains and expressions from the tensor reduction. Since no tree level diagram exists, to square the matrix element one has to calculate $14 \times 14 = 196$ long and complicated terms. Therefore, reasonable analytical calculations have to be performed by computer programs, and the Mathematica program that was applied is discussed in Section 3.5.1.

The polarized differential cross section is obtained by squaring the matrix elements and summing over color and spin of the final gluinos

$$\frac{\mathrm{d}\sigma_{\gamma\gamma}^{\lambda_1\lambda_2}}{\mathrm{d}\hat{t}} = \frac{1}{16\pi\hat{s}^2} \sum |\mathcal{M}_{\gamma\gamma}^{\lambda_1\lambda_2}|^2,$$

where $\hat{s} = (p_1 + p_2)^2$ and $\hat{t} = (p_1 - k_1)^2$ are the Mandelstam variables of the $\gamma\gamma$ scattering process. It should be noted that the two final gluinos form a color singlet state since the initial photons are color singlets. To calculate the total cross section one has to integrate over the allowed region of $\hat{t}$ and multiply by symmetry factor $1/2$ since there are two identical particles in the final state.

As described in Chapter 3, high energetic photons arise by the backscattering of laser light on high energy electrons. The energy spectrum of the backscattered photons can only be described by a probability distribution. Thus, for comparison with experimental measurements one has to convolute the photon cross section with the photon density function (Section 3.2) using the formula given in Section 3.4. This numerical evaluation has been done with the help of the Fortran program described in Section 3.5.2.

For comparison, the photon matrix elements were calculated analytically with the Mathematica package FormCalc [123], version 3.2, and the total partonic cross section was evaluated numerically with an enclosed Fortran program. The numerical values for the total partonic cross sections of the two calculations agree up to 14 digits.

Numerical Results

The photon-photon center-of-mass energy distribution of the unpolarized total partonic cross section is plotted in the left diagram of Fig. 5.2. As input parameter for the supersymmetric particles the SPS1 point given in Appendix B.1 of the 2001 Snowmass workshop [136] has been used, except for the value of the gluino mass. The latter was set to 350 GeV, well below the squark masses of ≈ 500 GeV, in order to clearly distinguish between the contributions of loop diagrams with different number of internal squarks. The different threshold behavior of the diagrams with one, two or three squarks is clearly demonstrated. Especially for the diagrams with two internal squarks there are two maxima in correspondence to the production thresholds of the squarks 1 and 2 of the first 2 generations, which are above 1050 GeV and 1100 GeV, respectively. The shapes are smeared out by the top quark contribution because of a lighter stop 1 squark. This threshold behavior is more distinctive if all squark mass parameter are equal to $M_S = M_{\tilde{q}_L} = M_{\tilde{q}_R}$ as shown in [134].
At the gluino pair production threshold the diagrams with one internal squark are the most important and become the dominant contribution for $M_S = M_{\tilde{q}_L} = M_{\tilde{q}_R}$. The diagrams with 3 internal squarks are suppressed due to the heavy squark masses.
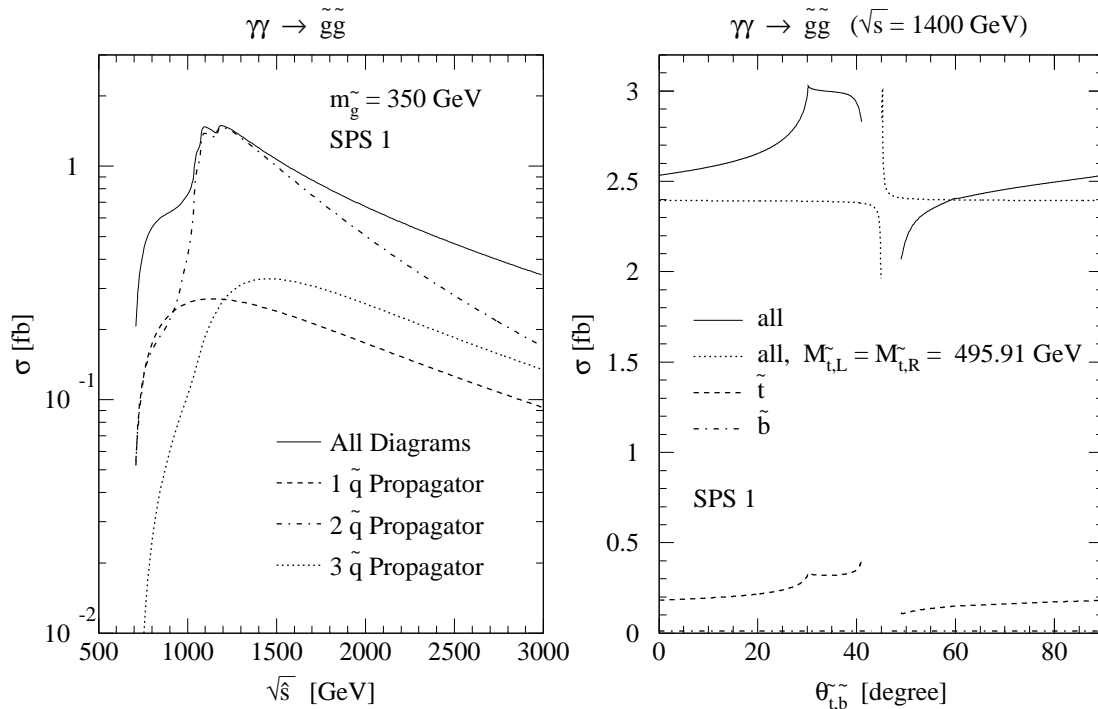
Figure 5.2: Unpolarized $\gamma\gamma$ cross section for SPS1. Left: Contributions of the various Feynman diagrams shown in Fig. 5.1, with one, two or three internal squarks. Right: Dependence of $\sigma_{\gamma\gamma}$ on the top and bottom squark mixing (leads to different squark masses). The curves show the cross section of the bottom loop diagrams (dot dashed, $\theta_{\tilde{b}}$ varied), the top loop diagrams (dashed line, $\theta_{\tilde{t}}$ varied) and the sum of all diagrams (solid and dotted line; $\theta_{\tilde{t}}$ varied, $\theta_{\tilde{b}} = 0°$). The central region is excluded by the mass bounds (Section 2.4)

But with contributions of 20% and more they are not negligible at intermediate ($\hat{s} \approx 1500$ GeV) or large (≈ 3000 GeV) center-of-mass energies.

It is important to notice that the photon-photon cross section in Fig. 5.2 (left) decreases much slower than in the e^+e^- annihilation, which typically decreases with $1/S$. Therefore, large numbers of events can be expected far above the production threshold.

The right plot of Fig. 5.2 shows the contributions of different quark flavors and the influence of the top squark mixing for a center-of-mass energy $\hat{s} = 1400$ GeV. Gluino and squark mass parameters $M_{\tilde{q}_L}$, $M_{\tilde{q}_R}$ are taken from SPS1, Appendix B.1, but the top and bottom squark mixing angle is varied between 0 and 90 degrees. Equation (2.8) for the squark mass eigenstates 1 and 2 leads to different top and bottom squark masses when the mixing angle is varied.

Due to the presence of the two initial photons the squared matrix element is proportional to the fourth power of the quark charges. Thus, the down-quark contribution is suppressed by a factor of 16 relatively to the up-quark ones. The cross section of the diagrams with bottom quarks inside the loops (dot-dashed line) is $\sigma_b \approx 0.0120$ fb

for $\theta_{\tilde{b}} = 0°$ that is equal to the down and strange quark contribution. The top quark contribution (dashed line) for $\theta_{\tilde{t}} = 0°$ is $\sigma_t = 0.183$ fb and is equal to the up and charm quark contribution, a factor of 15.25 bigger than the down quark one.

Furthermore, the contributions of all quark flavor add constructively since the number of couplings in the loops are even. Thus, the cross section is determined by the sum of u, c, t quark loops and is affected only by the top squark mixing. For SPS1 scenario this leads to a variation in $\hat{\sigma}$ of $\pm 25\%$ (solid line). The dotted line shows the total cross section for $M_{\tilde{t}_L} = M_{\tilde{t}_R}$. In this case, only for mixing angles close to 45 degrees, one has large top squark mixing and therefore small stop 1 masses, as described in the last chapter.

For light gluinos of 200 GeV and for equal left and right handed squark mass parameters ($M_{\tilde{q}_L} = M_{\tilde{q}_R} = 500$ GeV), it is possible to increment the cross section up to a factor of 10 with respect to the non-mixing case (see Fig. 5.3). This happens because the top squark 1 becomes light, near to the lower mass bound of 100 GeV.

In the right plot of Fig. 5.2, the singularity in the top quark contribution and therefore in the total cross section at $\theta_{\tilde{t}} = 30.16°$ arises because for the top squark-quark-gluino vertex the relation $m_{\tilde{t}_2} + m_t = m_{\tilde{g}}$ ($420.89 \ GeV + 174.3 \ GeV = 595.19 \ GeV$) is fulfilled. That means that the mass of the gluino would be equal to its decay products (discussed in equation (6.2) and text).

As mentioned above the photon cross section has to be convoluted with the photon density functions to obtain a measurable quantity (Section 3). This cross section is plotted in Fig. 5.3 as a function of the gluino mass. The initial electron polarisation is chosen to be 80% such that the number of initial $\gamma\gamma$ states with $L = 0$ is increased. The other setup values concerning the photon spectra are given in Section 3.2. The inclusive e^-e^- center-of-mass energy is varied with the gluino mass as $\sqrt{S} = 2m_{\tilde{g}}/0.8/0.867$, that means the production threshold of the gluino pairs is 0.8 of the maximum available $\gamma\gamma$ center-of-mass energy ($\sqrt{\hat{s}_{\gamma\gamma}^{max}} = 0.867\sqrt{S}$). Therefore, the unknown low energy photon spectrum is truncated in a natural way. The laser photon spectrum is normalized to the high energy peak (Section 3.2), thus the numbers of events per year can be obtained by multiplying the cross section with the luminosity of the high energy photon peak:

$$\# \frac{events}{year} \ = \ \sigma \cdot \mathcal{L}_{\gamma\gamma}(z > 0.8z_{max}) \ = \ \sigma \cdot 0.1 \mathcal{L}_{e^-e^-}^{geom} \ \approx \ \sigma \cdot \frac{1}{3}\mathcal{L}_{e^+e^-}$$

Fig. 5.3 shows cross sections for different values of $M_S = M_{\tilde{q}_L} = M_{\tilde{q}_R}$. Thick lines denote non-mixing squarks. The thin lines show the maximum possible cross section reached by varying the top squark mixing angle $\theta_{\tilde{t}}$. This variation leads to different values for the top squark masses. As one expects, the cross section is larger for small squark masses and reaches a maximum value of around 17 fb for light gluino masses of 300 GeV which means around 6000 events/year for a luminosity of $\mathcal{L}_{e^+e^-} = 1000 \ fb^{-1}$. Increasing the gluino mass up to 1700 GeV the cross section decreases very slowly. A cross section of $\sigma = 1$ fb (330 events/a) is obtained for small gluino masses and $M_S \approx 600$ GeV; and for heavy gluinos with masses of 1700 GeV squark masses up to $M_S \approx 800$ GeV are required. For larger $M_S \approx 1500$ GeV the cross section drops down to 0.1 fb. Contrary to e^+e^- annihilation, the gluino pair production process in photon-photon scattering is visible in a large range of MSSM parameter space.
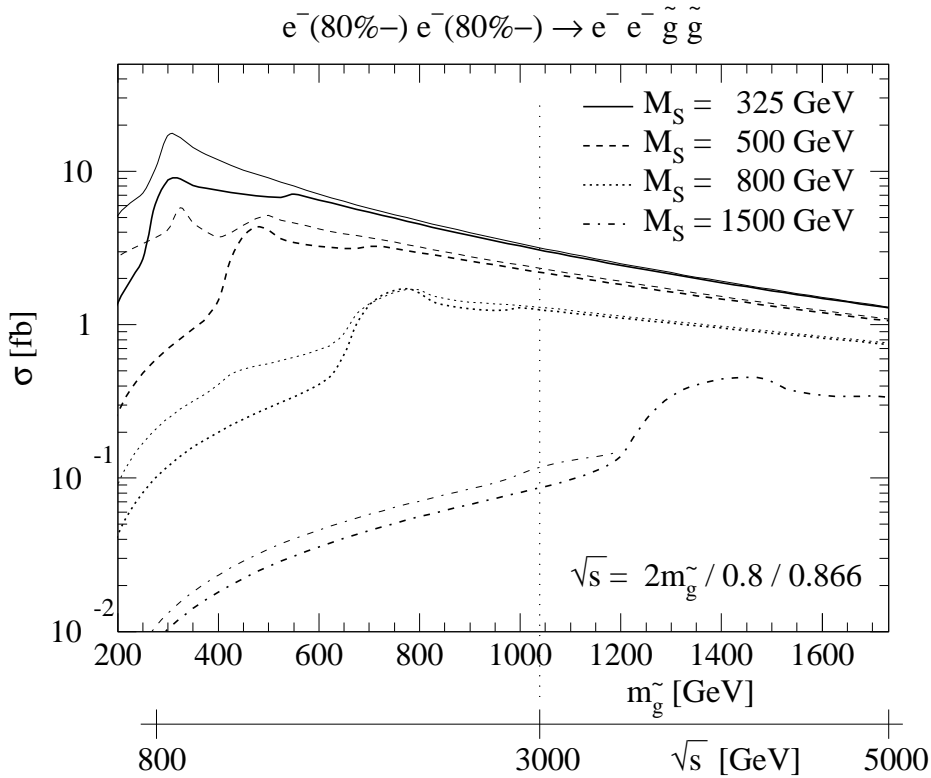
Figure 5.3: Center-of-mass distribution for polarized $e^- e^-$ cross section as a function of the gluino mass and various M_S with $M_S = M_{\tilde{q}_L} = M_{\tilde{q}_R}$. The electron energy depends on the gluino mass and is chosen in such a way that only the high energy peak of the photon spectrum contributes to the cross section: $\sqrt{S} = 2m_{\tilde{g}}/0.8/0.867$. Thick lines denote the non-mixing case, while thin lines the maximal top squark mixing. The photon spectrum is normalized to the high energy peak (see Section 3.3 and text).

The polarization of the initial electrons is important for the size of the cross section. At the gluino production threshold, the cross section rises as a S-wave if $L = 0$ for polarization $++ = --$ and is much steeper then $L = 2$ for polarization $-+ = +-$. Far above the production threshold the $-+ = +-$ can produce reasonable cross section [134]. Choosing the energy as in Fig. 5.3 the $++$ polarization increases the cross section considerably as shown in Table 5.1.

The transverse momentum and the rapidity distributions determine the direction of the final gluinos inside the detector. Fig. 5.4 indicates the corresponding plots for SPS1. Again, the partonic cross section was convoluted over the photon structure function for different polarization degrees. The photon density functions are appropriately normalized for the polarized and unpolarized case (Section 3.2). The center-of-mass energy of the initial electrons is $\sqrt{S} = 2m_{\tilde{g}}/0.8/0.867 = 1716.91$ GeV. The diagrams show that the gluinos have large transverse momenta and are localized around

$e^- e^-$ Polarization	SPS1	SPS5
$+\,+$ 80%	3.0196	2.2864
unpolarized	1.8397	1.4136
$-\,+$ 80%	0.9663	0.7564

Table 5.1: Influence of the polarization degree of the initial electrons on the cross section $\sigma_{e^-e^-}[fb]$. The energy is $\sqrt{S} = 2m_{\tilde{g}}/0.8/0.867$ and $\sigma_{++} = \sigma_{--}$, $\sigma_{+-} = \sigma_{-+}$.

$y_1 = 0$. Choosing the $+\,+$ polarization with a polarization degree of 80% for the initial electrons, the maximum of transverse momentum is considerably shifted to the value of $k_T^{max} = \frac{\sqrt{S}}{2}\sqrt{1 - \frac{4m_{\tilde{g}}}{S}}$. Due to the larger total cross section the transverse momentum and rapidity distribution also become larger for the $+\,+$ polarization.

A further uncertainty is induced by the dependence on the scale of the strong coupling constant. Because of two vertices in the Feynman diagrams (Fig. 5.1) that couple strongly, the cross section is proportional to $\alpha_s^2(\mu)$. The scale μ of the process was fixed to be equal to the mass of the gluino. A variation of the scale μ from $\frac{1}{4}m_{\tilde{g}}$ to $4m_{\tilde{g}}$ results in a cross section uncertainty of about $+40\%$ to -20%.

5.2 Resolved Contribution

In high energy photon scattering processes the photons can undergo a transition into virtual hadronic states of quarks and gluons. The quarks and gluons carry parts of photon momentum leading to a complicated density distribution. If the photon beams of both sides are "resolved" in the sense discussed above, gluino pairs can be produced via tree level Feynman diagrams.

Fig. 5.5 shows the Feynman diagrams of the double resolved gluino pair production process with an initial quark-antiquark pair. The s-channel diagram only depends on the gluino mass while the t- and u-channel diagrams depend additionally on the squark masses and, in principle, on the mixing angles. Because of its heavy mass there is almost no top quark inside the photon, and for the same reason the bottom distribution is strongly suppressed with respect to the light flavors. As the mixing of the squarks of the first two generations can be neglected, the cross section becomes independent of mixing effects.

For the numerical calculation the parton density functions of the quarks and the gluon inside the photon are taken from a leading-order, five-flavor fit to the photon structure function [137] that is implemented in the PDFLIB 8.0 [73]. Since there is no polarized density function available, the discussion here is restricted to the unpolarized case.
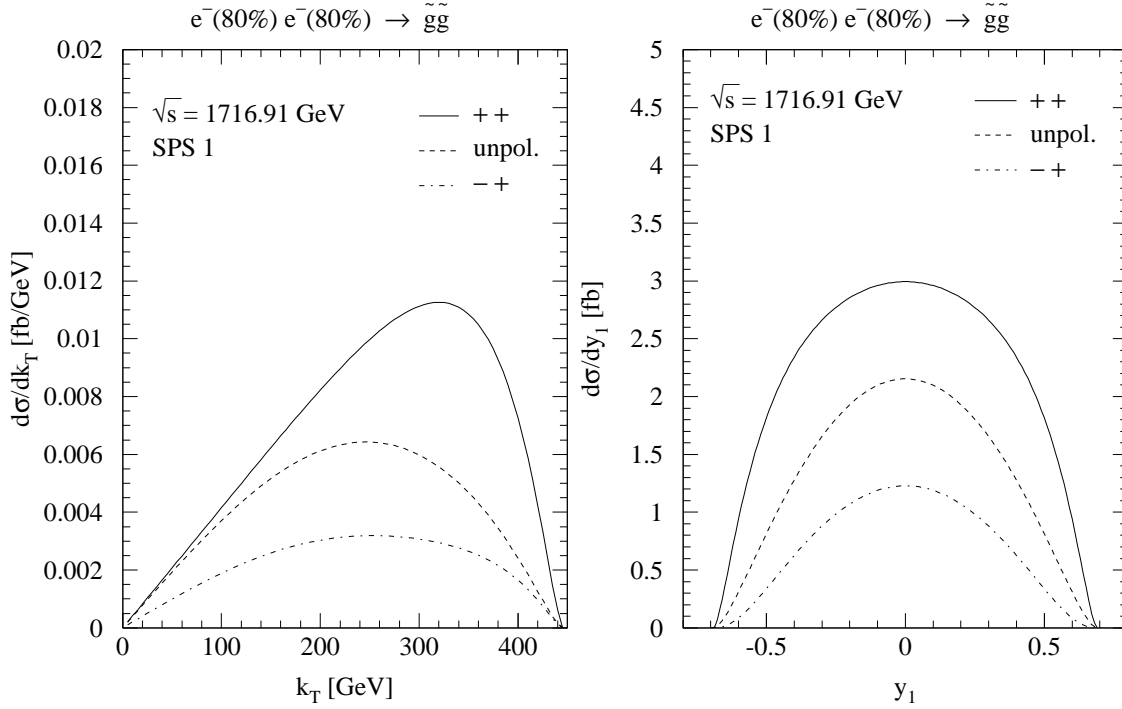
Figure 5.4: Distribution of the transverse gluino momentum k_T and the rapidity for different polarization degrees and SPS1 point. Left: It is integrated over the whole range of y_1 and y_2. Right: It is integrated over y_2 and the whole range of k_T.
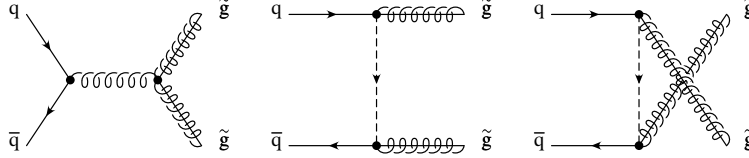
Figure 5.5: Resolved Feynman diagrams with initial quark-antiquark pair.

The spin- and color-averaged squared matrix element for one flavor is [138]

$$\overline{|\mathcal{M}_{q\bar{q}}|}^2 = 8\pi^2\alpha_s^2\frac{(N_C^2-1)}{N_C}\left(2\frac{2m_{\tilde{g}}^2\check{s}+(\check{t}-m_{\tilde{g}}^2)^2+(\check{u}-m_{\tilde{g}}^2)^2}{\check{s}^2}+2\frac{m_{\tilde{g}}^2\check{s}+(\check{t}-m_{\tilde{g}}^2)^2}{\check{s}(\check{t}-m_{\tilde{q}}^2)}\right.$$

$$+2\frac{m_{\tilde{g}}^2\check{s}+(\check{u}-m_{\tilde{g}}^2)^2}{\check{s}(\check{u}-m_{\tilde{q}}^2)}+\frac{(\check{t}-m_{\tilde{g}}^2)^2}{(\check{t}-m_{\tilde{q}}^2)^2}+\frac{(\check{u}-m_{\tilde{g}}^2)^2}{(\check{u}-m_{\tilde{q}}^2)^2}\right)$$

$$+8\pi^2\alpha_s^2\frac{(N_C^2-1)}{N_C^3}\left(2\frac{m_{\tilde{g}}^2\check{s}}{(\check{t}-m_{\tilde{q}}^2)(\check{u}-m_{\tilde{q}}^2)}-\frac{(\check{t}-m_{\tilde{g}}^2)^2}{(\check{t}-m_{\tilde{q}}^2)^2}-\frac{(\check{u}-m_{\tilde{g}}^2)^2}{(\check{u}-m_{\tilde{q}}^2)^2}\right),\quad(5.2)$$

where $N_C = 3$ denotes the number of colors and $\check{s}$, $\check{u}$, $\check{t}$, are the Mandelstam variables of the $2 \rightarrow 2$ scattering process.

There are also double resolved processes possible with two gluons in the initial state.

The Feynman diagrams are at tree level and shown in Fig. 5.6. The process at lowest
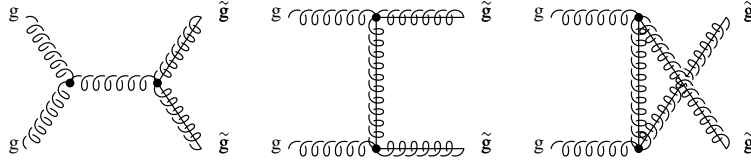
Figure 5.6: Resolved Feynman diagrams with two initial gluons.

order depends only on the gluino mass. The corresponding spin- and color-averaged squared matrix element is [138]

$$\overline{|\mathcal{M}_{gg}|}^2 = \frac{32\pi^2\alpha_s^2 N_C^2}{(N_C^2 - 1)} \left(\frac{1}{(\check{t} - m_{\tilde{g}}^2)(\check{u} - m_{\tilde{g}}^2)} - \frac{1}{\check{s}^2} \right)$$
$$\times \left((\check{t} - m_{\tilde{g}}^2)^2 + (\check{u} - m_{\tilde{g}}^2)^2 + 4m_{\tilde{g}}^2\check{s} - \frac{4m_{\tilde{g}}^4\check{s}^2}{(\check{t} - m_{\tilde{g}}^2)(\check{u} - m_{\tilde{g}}^2)} \right).$$

The third class would be the single resolved process with one initial photon and one initial gluon. The process starts at one loop level with squarks and quarks inside the loops. The contributions were calculated but are to small to appear in the figures given below.

Numerical Results

The resolved photon-photon cross section $\sigma_{\gamma\gamma}$ is calculated by summing over the contributions of the five light quark flavors and the gluon and integrating over the appropriate density function $f_{i/\gamma}(x, M^2)$ of the quark ($i = u, d, c, s, b$) and gluon ($i = g$) as denoted in Section 3.4. The structure functions depend on a factorization scale M which is identified with the gluino mass. The variation of this scale by a factor of four leads to a variation for the double-resolved photon cross section of $\pm 35\%$. The masses of the five initial quark and antiquark flavors are neglected because the collinear limit at high center-of-mass energies is considered.

In Fig. 5.7 the dependence of the unpolarized photon-photon cross sections on the $\gamma\gamma$ center-of-mass energy is plotted. The gluino mass is $m_{\tilde{q}} = 200$ GeV and the squark mass parameter $M_S = M_{\tilde{q}_L} = M_{\tilde{q}_R}$ in the left panel is $M_S = 325$ GeV and in the right panel $M_S = 1500$ GeV.
Both resolved contributions, the $q\overline{q}$ annihilation and the gg fusion, are in principle large because of the large number of color states of the final gluinos. Thus, the gluon contribution becomes huge at large center-of-mass energies, because gluino pairs can be produced at small x, where the gluon density function is very large. The cross section of the resolved diagrams with initial quark-antiquark (dotted line) is larger for $M_S = 1500$ GeV than for 325 GeV. The reason is a destructive interference between the s-channel diagram of Fig. 5.5 and the t-, u-channel diagrams, see equation (5.2). While the s-channel depends only on the gluino mass, the t- and u-channels decrease for larger squark masses and therefore the cross section rises.
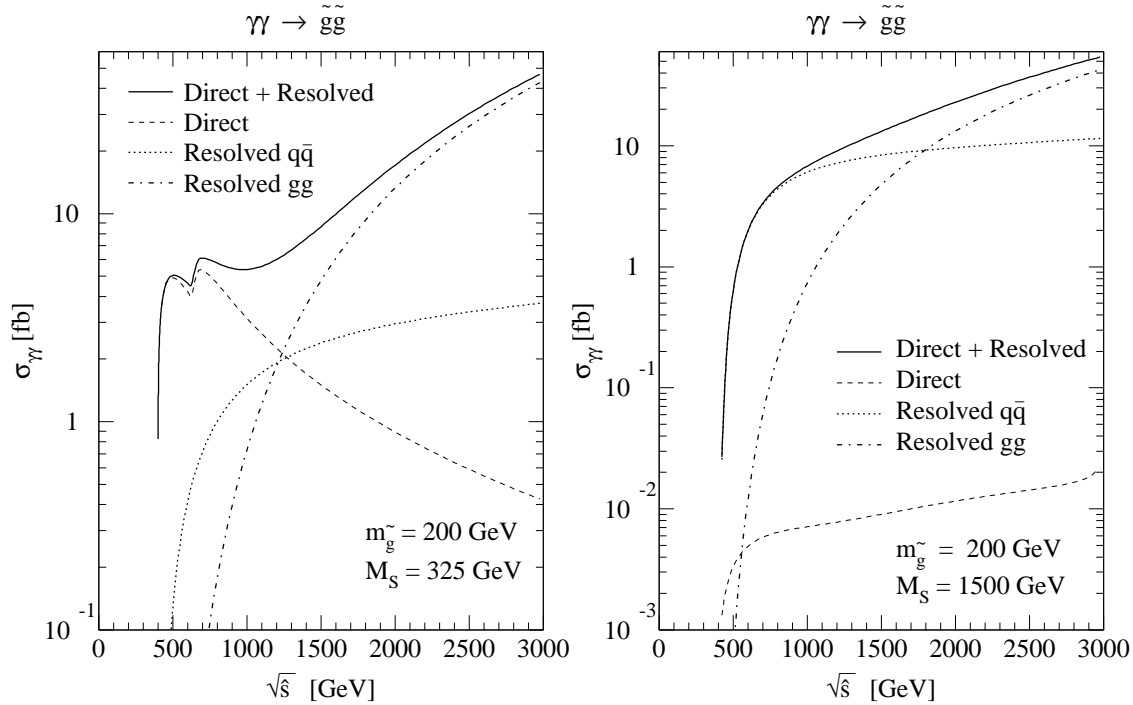
Figure 5.7: Dependence of the unpolarized photon-photon cross section on the center-of-mass energy $\hat{s}$ for light gluino mass of 200 GeV and light squark masses 325 GeV (left panel) and heavy squark masses 1500 GeV (right panel). The resolved contributions are convoluted with the parton densities inside the photon.

The gluon density function of the photon is small for large gluon momentum fraction x but increases steeply at small x. Therefore, in Fig. 5.7 one can see the gluon contribution (dot-dashed line) is negligible near the gluino pair production threshold $\sqrt{\hat{s}} = 400$ GeV, but will be important and much larger than the $q\bar{q}$ resolved cross section for large center-of-mass energies, i.e. $\sqrt{\hat{s}} = 3000$ GeV.

With respect to the direct one-loop pair production the complete resolved cross section is negligible for small squark masses $M_S = 325$ GeV near the gluino production threshold, Fig. 5.7 (left panel). Whereas, for large squark masses $M_S = 1500$ GeV the resolved contribution is three orders of magnitude larger than the direct contribution Fig. 5.7 (right panel). This only holds for very small gluino masses like $m_{\tilde{q}} = 200$ GeV. For larger gluino masses the resolved cross section decreases rapidly to a minimum at $m_{\tilde{q}} \approx m_{\tilde{g}}$ and becomes almost constant (Fig. 5.8).

Fig. 5.8 shows the dependence of the total unpolarized electron-electron cross section on the gluino mass. As in Fig. 5.3 the electron center-of-mass energy is varied simultaneously with the gluino mass. Note that Fig. 5.3 shows polarized cross sections, the unpolarized ones would be roughly two times smaller. Moreover, the y-scales of the two figures are different.

Choosing the electron center-of-mass energy in this way, only the high energy peak
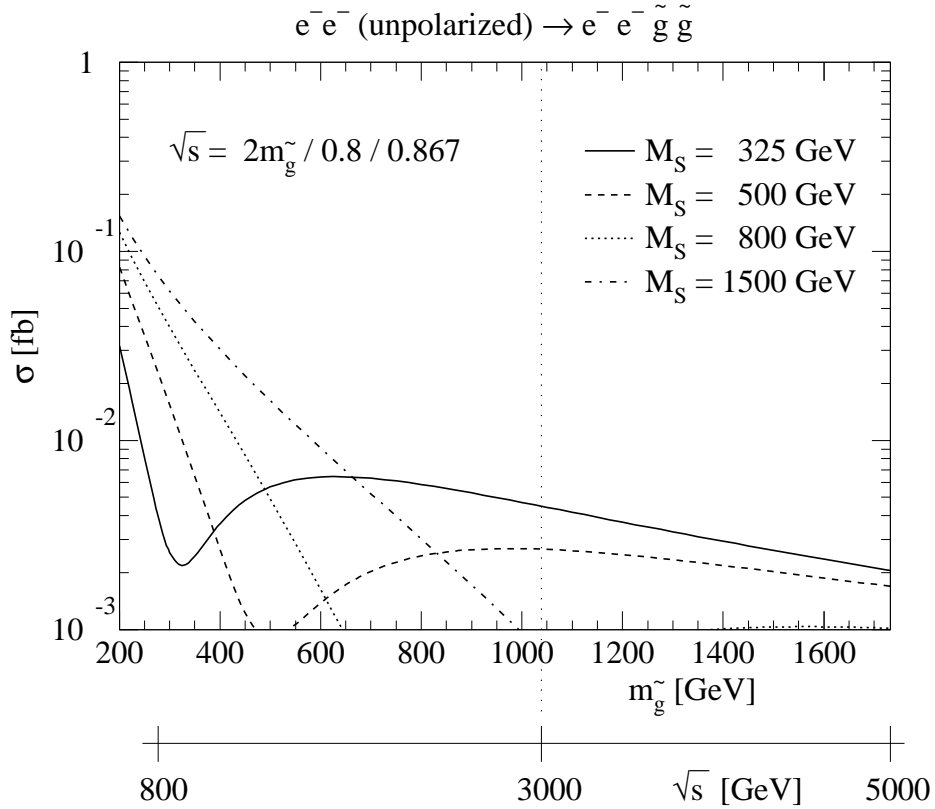
Figure 5.8: Dependence of the unpolarized e^-e^- cross section $[fb]$ on the gluino mass, with non-mixing squarks and $M_S = M_{\tilde{q}_L} = M_{\tilde{q}_R}$. The electron energy depends on the gluino mass and is chosen so that only the high energy peak of the photon spectrum contributes to the cross section: $\sqrt{S} = 2m_{\tilde{g}}/0.8/0.867$. The photon spectrum is normalized to the high energy peak (see Section 3.3 and text).

of the laser photon spectrum Fig. 3.2 contributes and the $\gamma\gamma$ center-of-mass energy is maximally 20% higher than the pair production threshold. Thus, the resolved contribution is suppressed for large ranges of the gluino mass due to the quark and gluon density function. Only for a small gluino mass, up to 400 GeV, and large squark masses, $M_S = 1500$ GeV, the resolved cross section is $0.03 - 0.15$ fb, thus comparable or larger than the direct photon cross section.

The same suppression of the resolved contribution can be reached far above the pair production threshold. Imposing a minimal total energy for the final gluino pair to be larger than $0.8 \cdot 0.867 \cdot \sqrt{S_{ee}}$, resolved contributions are negligible as well.

$e^- e^-$ (unpolarized) $\rightarrow e^- e^- \tilde{g} \tilde{g}$

all flavors

u

u: s-channel

u: t-channel

σ [fb]

$m_{\tilde{g}}$ [GeV]

$\sqrt{s}$ [GeV]

Fig. 5.9 shows the contributions of the different Feynman diagrams for the resolved $q\overline{q} \rightarrow \tilde{g}\tilde{g}$ production. The solid line represents the cross section of the $u\overline{u} \rightarrow \tilde{g}\tilde{g}$ production channel. Since the s-channel (dashed line) and the t-channel (dot-dashed line, t stands for both: t- and u-channel) interfere destructive, the total cross section is smaller. S-channel diagrams typicaly decreases with $1/\hat{s}$ for increasing center-of-mass energies $\hat{s}$, whereas the t-channel diagrams decreases much slower. A similar behavior can be seen in Fig. 5.9. Therefore the curves intersect each other leading to a local minimum of the total cross section.

Figure 5.9: Contributions of the s- and t,u-channel Feynman diagrams of Fig. 5.5 to the resolved $q\overline{q}$ cross section.

Chapter 6

Squark Pair Production in Photon-Photon Collisions

In this chapter, the squark pair production process in photon-photon collisions is discussed. The high energy incoming photons are generated by laser-backscattering (Chapter 3). The Feynman diagrams for the $\gamma\gamma$ scattering process are three tree level diagrams, thus large cross sections are expected.

The lowest order behavior for polarized laser-backscattered photons is analyzed in the next section. The one loop corrections (Section 6.2) are of two types: the ones mediated by massless bosons (photon and gluon, Section 6.2.1), and the remaining MSSM ones (Section 6.2.2). The resulting total corrections for SPS1 and SPS5 are displayed in Section 6.2.3.

Furthermore, the production of squark pairs in resolved processes for the case of unpolarized laser-photons is discussed in Section 6.3. The squark pair production at tree level in direct scattering and the resolved process have been published in [139].

Squark pair production in $\gamma\gamma$-collisions at tree level has been considered previously either with bremsstrahlung photons [140, 141] or with unpolarized backscattered laser photons in [35, 142]. The pair production process in collisions of polarized backscattered laser photons was calculated at leading order in [143, 144]. The QCD and supersymmetric QCD one-loop corrections to squark pair production were calculated in [35] but no agreement to those calculation could be found.

6.1   Tree level cross section

The generic squark pair production process in photon-photon scattering is given as

$$\gamma(p_1, \lambda_1)\, \gamma(p_2, \lambda_2)\ \rightarrow \tilde{q}_i(k_1)\, \tilde{q}_i^*(k_2)$$

where $p_{1,2}$ are momenta and $\lambda_{1,2} = \pm 1$ are the polarization of the incoming photons, and $k_{1,2}$ are the momenta of the outgoing squark $\tilde{q}_i$ and anti-squark $\tilde{q}_i^*$. The initial photon polarization is again restricted to be circular. The outgoing squark color states
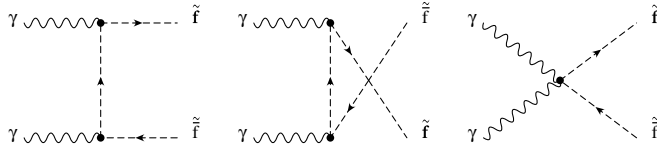
Figure 6.1: Leading order Feynman diagrams for direct squark production in photon-photon collisions.

are always summed up. The index i denotes the squark mass eigenstates 1 or 2. Throughout this chapter an electromagnetic fine structure constant with $\alpha = 1/137.036$ is used. Contrary to e^+e^- annihilation, at tree level no mixed final states $\tilde{q}_1\tilde{q}_2^*$ or $\tilde{q}_1^*\tilde{q}_2$ are allowed. The Feynman diagrams are the three graphs displayed in Fig. 6.1. Using the Feynman rules of [101] the polarized matrix element for one flavor q and one squark mass eigenstate i with $i = \{1,\, 2\}$ is

$$|M_{\gamma\gamma}^{\lambda_1\lambda_2}|^2 \;=\; \frac{64\,\pi^2\,\alpha_e^2\,e_q^4\,N_c}{(\hat{t} - m_{\tilde{q}_i}^2)^2(\hat{u} - m_{\tilde{q}_i}^2)^2} \tag{6.1}$$

$$\times \left(\hat{s}m_{\tilde{q}_i}^4 + (1 - \delta_{\lambda_1\lambda_2})\big[(\hat{t} - m_{\tilde{q}_i}^2)^2(\hat{u} - m_{\tilde{q}_i}^2)^2 - 2m_{\tilde{q}_i}^2\,\hat{s}\,(\hat{t} - m_{\tilde{q}_i}^2)(\hat{u} - m_{\tilde{q}_i}^2)\big] \right),$$

where $N_C = 3$ denotes the number of colors and $\hat{s}$, $\hat{u}$, $\hat{t}$, are the Mandelstam variables of the $\gamma\gamma \to \tilde{q}_i\tilde{q}_i^*$ scattering process. The differential cross section is defined through equation (3.11) and the total cross section is obtained by integrating over $\hat{t}$. The matrix element of slepton pair production is obtained from equation (6.1) by replacing $N_c \to 1$ and inserting the appropriate charges and masses.

In Fig. 6.2 the unpolarized cross section of the scattering process $\gamma\gamma \to \tilde{q}_i\tilde{q}_i^*$ compared to $e^+e^- \to \tilde{q}_i\tilde{q}_i^*$ is plotted as a function of the center-of-mass energy. In the left panel, σ is displayed for final up-type squarks and in the right panel for final down-type squarks with masses $m_{\tilde{q}} = 200$ GeV. The $\gamma\gamma$ matrix element given in equation (6.1) depends only on the fourth power of the squark charges and masses. Therefore, the cross sections (solid line) of final up-type squarks are four times larger than those of down-type squarks. Also the cross sections of left and right squark eigenstates are equal and would be equal for the mixed eigenstates q_1 and q_2 too, if their masses were be degenerated. Thus, the $\gamma\gamma$ cross section at tree level is for fixed masses independent of the squark mixing angle. This fact is important for the top- and bottom-squark production.

On the other hand, the e^+e^- cross section[1] depends additionally on the weak isospin and in particular on the squark mixing angle through the Z-boson exchange. Because of the different coupling of the Z-boson to left and right squark states, the cross sections, Fig. 6.2, for left- and right-handed final squarks are not equal anymore. The cross section could vary between the two curves for $\theta_{\tilde{q}} \neq 0$ (keeping the squark masses fixed). The different distance between the $\tilde{q}_L\tilde{q}_L^*$ and $\tilde{q}_R\tilde{q}_R^*$ cross sections for up- (left panel) and down-type (right panel) squark is due to the value of the weak isospins $(I_{u,d}^3 = \pm 1/2)$.

---

[1]Unpolarized and polarized tree level cross sections of the $e^+e^- \to \tilde{q}\tilde{q}^*$ scattering process can be found in [145].
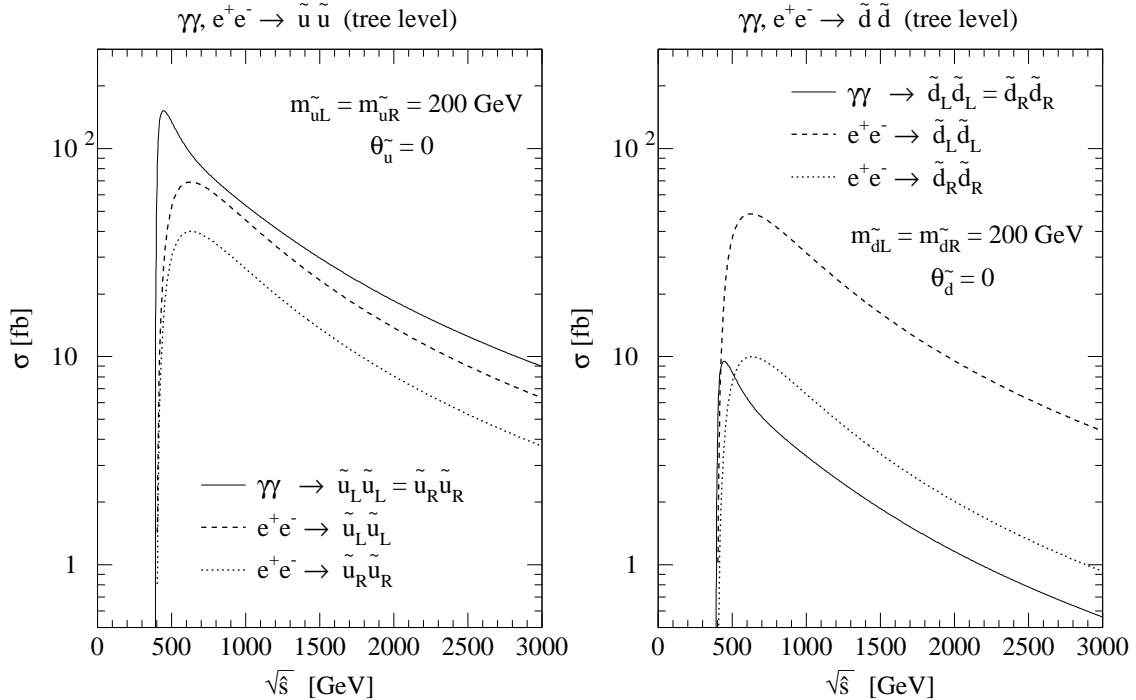
Figure 6.2: Unpolarized cross section of $\gamma\gamma \rightarrow \tilde{q}_i\tilde{q}_i^*$ (solid line) compared with $e^+e^- \rightarrow \tilde{q}_i\tilde{q}_i^*$ (dashed and dotted line) as a function of $\sqrt{\hat{s}}$. Left: For final up-type squarks ($e_u = 2/3$). Right: For final up-type squarks ($e_d = -1/3$).

Moreover, the threshold behavior for $\gamma\gamma$ and e^+e^- is different. The e^+e^- cross section rises like β^3 where $\beta = \sqrt{1 - 4m_{\tilde{q}}^2/s}$, as a P-wave due to the spin-1 intermediate boson. However, the $\gamma\gamma$ cross section rises like β as an S-wave because of the $L = 0$ initial photon-photon states. This is shown in Fig. 6.2 and Fig. 6.3.

In Fig. 6.3 (left panel) one can see the analogous distributions for top squark pair production for parameters of SPS5, Appendix B.2, namely $m_{\tilde{t}_1} = 201$ GeV, $m_{\tilde{t}_2} = 658$ GeV and $\theta_{\tilde{t}} = 146°$. Because of the stop mixing angle, $\sigma_{e^+e^-}$ is much smaller than $\sigma_{\gamma\gamma}$. However, through Z-boson exchange in electron-positron annihilation, mixed squark pairs $\tilde{t}_1\tilde{t}_2$ could also be produced, allowing for a measurement of the $\tilde{t}_2$ mass if the $\tilde{t}_2\tilde{t}_2^*$ pair creation is kinematically forbidden.

The right plot of Fig. 6.3 displays the $\gamma\gamma$ cross section for various initial photon polarizations as a function of the center-of-mass energy. The $L = 0$ ($L = |\lambda_1 - \lambda_2|$) initial state rises like β much steeper than the $L = 2$ initial state, but after reaching a maximum it drops down rapidly. The $L = 2$ initial $\gamma\gamma$ state decreases much slower. Therefore, measurements at the production threshold prefers the $L = 0$ state, while far above the threshold the $L = 2$ initial $\gamma\gamma$ state becomes more advantageous.

To calculate a measurable quantity one has to integrate the photon-photon cross section over the photon density function. The result of this integration is given in Fig. 6.4 for the high energy peak of the photon spectrum (Fig. 3.2). The plot shows polarized cross sections as a function of the up-squark mass for $\theta_{\tilde{u}} = 0$, i.e. $\tilde{u}_1 = \tilde{u}_L$ and $\tilde{u}_2 = \tilde{u}_R$.
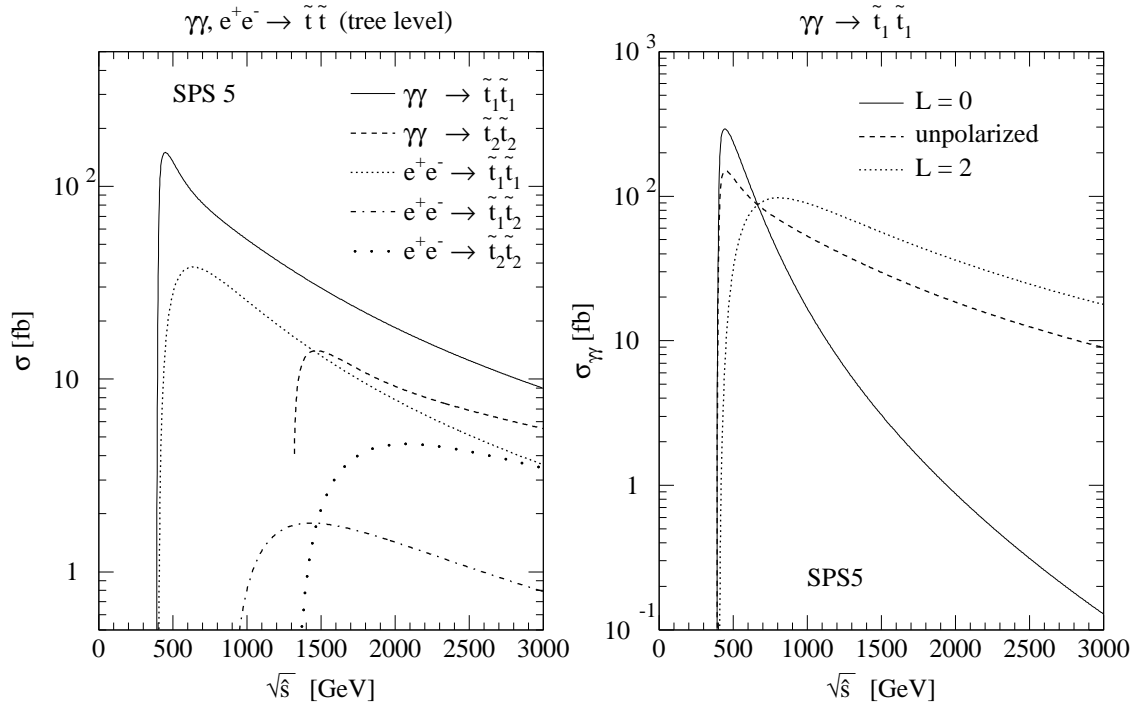
Figure 6.3: (Parameters of SPS5) Left: Unpolarized $\tilde{t}_i\tilde{t}_i^*$ cross section in $\gamma\gamma$ and e^+e^- scattering as a function of $\sqrt{\hat{s}}$. Right: Influence of the initial $\gamma\gamma$-polarization on the cross section ($L = |\lambda_1 - \lambda_2|$).

The varied squark mass $m_{\tilde{u}}$ stays either for $m_{\tilde{u}_L}$ or $m_{\tilde{u}_R}$. The solid line represents the integrated photon-photon cross section, where the photon density function was normalized as explained in Section 3.3. For comparison, the corresponding e^+e^- cross sections (dashed and dotted line) are plotted. The energy for both scatterings is varied with the squark mass as $\sqrt{S_{ee}} = 2m_{\tilde{g}}/0.8/0.867$.

The expected cross section is of $\mathcal{O}(500fb)$ for small squark masses $m_{\tilde{u}} = 100$ GeV, and drops down to $\mathcal{O}(1)fb$ for large squark masses $m_{\tilde{u}} = 1700$ GeV. The $\gamma\gamma$ cross section is always larger than that of e^+e^-, but one has to note that the luminosity of the e^+e^- process might be 3 times higher than the $\gamma\gamma$ luminosity. The $\gamma\gamma$ cross section, however, is given only for one final state of $\tilde{u}_L\tilde{u}_L^*$ and $\tilde{u}_R\tilde{u}_R^*$.

Fig. 6.5 shows the momentum and the rapidity distributions for the convoluted $\gamma\gamma$ cross section, for a realistic electron polarization and for SPS1. The electron center-of-mass energy is chosen to be $\sqrt{S} = 2m_{\tilde{t}_1}/0.8/0.867 = 580$ GeV, thus the production threshold corresponds to the high energy peak of the photon density function and the curves are normalized to this peak. Cross sections are shown for different initial electron polarization with $2\lambda_e P_c = 0.8$. The squarks have large transverse momenta and are localized around $y_1 = 0$. Choosing the $++$ polarization for the initial electrons, the maximum of transverse momentum is considerably shifted to its maximum kinematically allowed value. Due to the larger total cross section the transverse momentum and rapidity
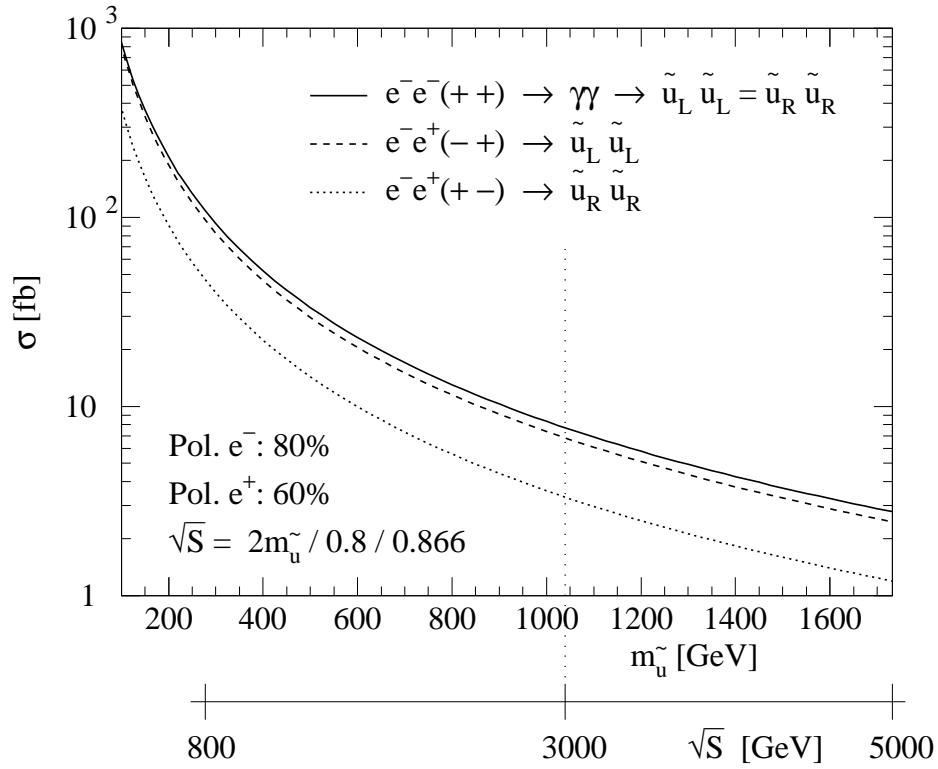
Figure 6.4: Polarized cross sections as a function of the up-squark mass for $e^- e^- \rightarrow \gamma\gamma \rightarrow \tilde{q}\tilde{q}^*$ and $e^+ e^- \rightarrow \tilde{q}\tilde{q}^*$ scattering. The energy for all curves is $\sqrt{S_{ee}} = 2m_{\tilde{g}}/0.8/0.867$. $\sigma_{\gamma\gamma}$ is normalized as discussed in Section 3.3. The polarization $(+-$ or $-+)$ of the $e^+ e^-$ scattering process is chosen to obtain the largest possible cross section.

distribution also become larger for the $++$ polarization.
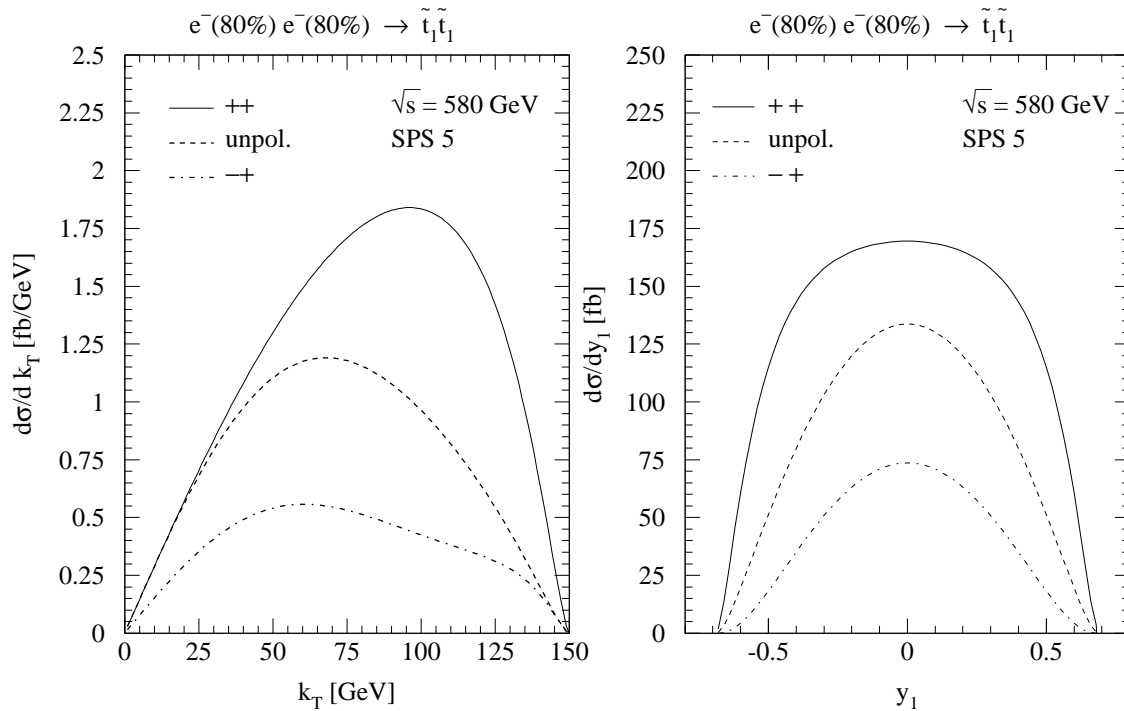
Figure 6.5: (Parameters of SPS5) Transverse momentum (left panel) and rapidity (right panel) distribution for the convoluted $\gamma\gamma$ cross section and realistic electron polarization. The electron center-of-mass energy is chosen to be $\sqrt{S} = 2m_{\tilde{t}_1}/0.8/0.867 = 580$ GeV and the curves were normalized to the high energy peak.

6.2 Full MSSM One-Loop Corrections

In this section, the next-to leading order corrections of the squark pair production are discussed. Quarks couple strongly and electroweakly. The corrections due to the strong interaction are larger than the electroweak ones. However, because of the large number of electroweak diagrams, these can not be neglected for precision measurements.

The $\mathcal{O}(\alpha_s)$ corrections consist of diagrams with gluon exchange, gluino exchange and that with squark exchange. The latter are not pure strong corrections since the 4 squarks couplings also contain an electroweak part. For this discussion, the corrections are divided into two parts:

- In Section 6.2.1, the one-loop corrections due to the gluon and photon exchange are considered. They are infrared (IR) and ultraviolet (UV) divergent. The diagrams contain only an additional gluon or photon and are, apart from the final squark mass, independent of any MSSM parameter and mixing angles.

- In Section 6.2.2 the remaining one-loop corrections are considered. They are subdivided into the gluino, the squark and the electroweak contributions. The electroweak corrections can not be distinguished in SM- and MSSM-like because many mixed graphs appear. They also depend on many MSSM parameters. In particular the gluino correction depends on the gluino mass and the final squark mixing angle, while the squark correction depends on the MSSM parameters of the squark sector.

The Feynman diagrams and matrix elements have been generated with the Mathematica package FeynArts [103] version 3.2 and the MSSM model file [101]. The FeynArts package is extensively proven to generate the full set of Feynman diagrams at each order. For practical calculations one uses the Feynman gauge, $\xi = 1$, to reduce the size of mathematical expressions. To verify the calculation, different programs and methods have been used.

To calculate the squared matrix elements, the Mathematica program displayed in Section 3.5.1 was used. The corrections were calculated additionally with the package FormCalc [123] and the results were numerically compared. The divergent integrals were regularized using DRED and DREG and an agreement among them was found. Additionally the FormCalc [123] method of constrained differential renormalization (CDR) [146] was applied. Differential renormalization(CD) [147] is a renormalization method using coordinate space leading to finite Green functions without intermediate regularization or explicit counterterms, whereas the result contains arbitrary dimensionful constants (like renormalization scales). Then, these constants have to be arranged that the renormalized Green functions fulfill the Ward identities. In CDR, introduced in [148] at the one loop level, a minimal set of consistent formal manipulations is used that automatically the renormalized Green functions preserves the Ward identities. It has been shown in [123] that at one-loop level the method of CDR is equivalent to DR. Also this method leads to the same results.
Since only gauge-boson-squark-squark couplings occur at tree level, no Supersymmetry

restoring counterterms were necessary.

Because of divergent tensor integrals that appear in the matrix elements one has to renormalize the theory. For this thesis the On-shell scheme for the squark sector has been used (Section 2.5.3).

The differential and total cross sections were numerically calculated using the fortran program of Section 3.5.2. The results are compared as far as possible with the numerical calculation of FormCalc [123] (in FormCalc no convolution of parton density functions is possible).

Unfortunately, it is not possible to vary all MSSM parameters because of their large number. Therefore, the one-loop corrections are demonstrated for the pair production of top-squarks 1 for the parameter points SPS1 and SPS5, Appendix B. The stop mass of SPS1 is $m_{\tilde{t}_1} = 375.9$ GeV and for SPS5 $m_{\tilde{t}_1} = 201.4$ GeV.

Furthermore, all figures of this section show unpolarized cross sections.

6.2.1 Photon and Gluon Corrections

There are 25 one-loop Feynman diagrams for virtual gluon and 25 for photon exchange. Fig.6.6 shows typical diagrams of the gluon virtual corrections. The virtual photon
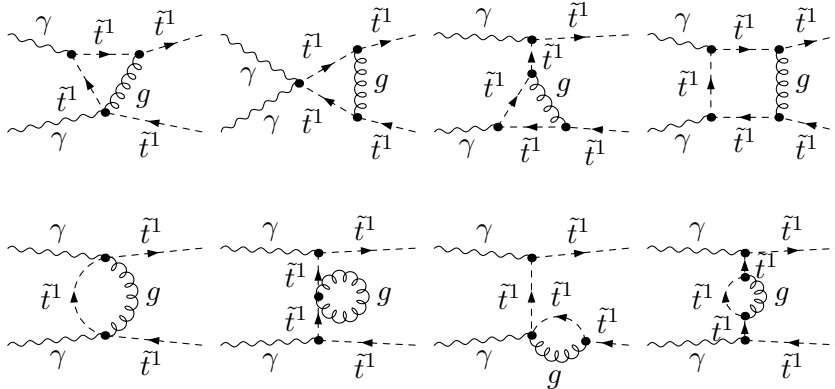
Figure 6.6: Typical Feynman diagrams for virtual gluon corrections.

Feynman diagrams are obtained by replacing the final gluons with photons. As already mentioned, besides the coupling constants they depend only on the final squark mass. The matrix elements are UV and IR divergent. By adding the corresponding on-shell counterterms (Section 2.5.4), the UV-divergences cancel. This has been checked analytically. Virtual IR-divergences arise for vanishing photon or gluon momenta. Since the particle masses are zero the corresponding propagator of the loop integral diverges. These divergences have to cancel against the divergences that appear because of real photon or gluon emission [149]. The IR-divergences of the real emission process arise because in case of small external gluon or photon momenta, the radiation process can not be distinguished experimentally from the one with no radiation.

Infinitesimal masses m_g and m_γ are assigned to the gluon and to the photon to regularize these IR-divergences.In case of QCD, gauge invariance is not spoiled by this

procedure because the non-abelian nature of QCD does not emerge at NLO. The introduction of the infinitesimal masses leads to a logarithmic dependence on m_g and m_γ, respectively, that must cancel when all NLO contributions are added together.

The real corrections consist of 12 Feynman diagrams for each gluon and photon bremsstrahlung. Fig. 6.7 shows typical diagrams for the gluon radiation. The photon
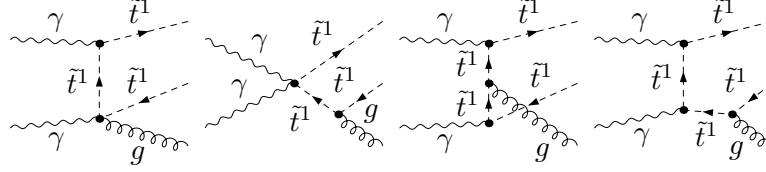
Figure 6.7: Typical Feynman diagrams for real gluon corrections.

radiation Feynman diagrams are obtained by replacing the final gluons with photons. It is convenient to introduce an unphysical cut-off energy E_{cut} to separate their phase spaces into two regions, a soft region with $m_{g,\gamma} \leq k^0 \leq E_{cut}$ and a hard region with $E_{cut} \leq k^0 \leq E_{max}$. k^0 is the energy of the gluon or photon and E_{max} the maximal allowed energy defined by kinematics. This has the advantage, that the hard process is free of IR-divergences and can be calculated with the formula equation (3.13). Furthermore, the soft part can be computed in the eikonal approximation leading to a multiplicative factor to the tree level cross section.
Summing up the virtual, soft and hard contributions the cross section must be independent of the small mass parameter $m_{g,\gamma}$ and of the cut-off energy.

As mentioned above the soft contribution can be written as

$$d\sigma_{\text{soft}} = d\sigma_{\text{Born}}\delta_{\text{soft}}(\lambda, E_{\text{cut}}) \, ,$$

where $\lambda = m_g$ for gluon bremsstrahlung and $\lambda = m_\gamma$ for photon bremsstrahlung. The soft photon factor is given as [150]

$$\delta_{\text{soft}}^\gamma(\lambda, E_{\text{cut}}) = -\frac{4\pi\alpha_e}{(2\pi)^3} \sum_{i,j=1}^n \frac{\pm Q_i Q_j}{2} \int_{|\mathbf{k}| \leq E_{\text{cut}}} \frac{d^3k}{k^0} \frac{p_i p_j}{(p_i k)(p_j k)}$$

where the sum runs over all n external particles with momentum p and particle charge Q, and k is the momentum of the soft photon. The "+" sign refers to the case that both charges of particles i and j flow into the diagram. If both charges flow out, one has the "-" sign.

The soft gluon factor for the two external squark pair production is

$$\delta_{\text{soft}}^g(\lambda, E_{\text{cut}}) = -\frac{4\pi\alpha_s}{(2\pi)^3} \sum_{i,j} \frac{\pm C_F}{2} \int_{|\mathbf{k}| \leq E_{\text{cut}}} \frac{d^3k}{k^0} \frac{p_i p_j}{(p_i k)(p_j k)}$$

where the sum runs over the two final squarks, $C_F = (N^2 - 1)/(2N) = 4/3$ and one has the "+" for $i = j$ and "-" otherwise. The integral $I_{ij} = \int_{|\mathbf{k}| \leq E_{\text{cut}}} \ldots$ has been

calculated in [151] and is given as [150]

$$I_{ij} = \frac{4\pi\,\alpha\,p_i p_j}{(\alpha p_i)^2 - p_j^2} \left\{ \frac{1}{2}\log\frac{(\alpha p_i)^2}{p_j^2}\log\frac{4E_{\text{cut}}^2}{\lambda^2} \right.$$

$$\left. + \left[\frac{1}{4}\log^2\frac{u_0 - |\mathbf{u}|}{u_0 + |\mathbf{u}|} + \text{Li}_2\left(1 - \frac{u_0 + |\mathbf{u}|}{v}\right) + \text{Li}_2\left(1 - \frac{u_0 - |\mathbf{u}|}{v}\right) \right]_{u=p_j}^{u=\alpha p_i} \right\},$$

with v and α definded like

$$v = \frac{(\alpha\,p_i)^2 - p_j^2}{2(\alpha\,p_{i0} - p_{j0})} \quad \text{and} \quad \alpha^2 p_i^2 - 2\alpha\,p_i p_j + p_j^2 = 0\ , \quad \frac{\alpha\,p_{i0} - p_{j0}}{p_{j0}} > 0\ .$$

To evaluate the soft factors in Fortran, a slightly modified routine was taken from FormCalc3.2 [123].

Fig. 6.8 shows the cancellation of the λ and E_{cut} dependence considering as an example the gluon correction to the $\gamma\gamma \to \tilde{t}_1 \tilde{t}_1^*$ scattering process. As parameters the SPS1 point
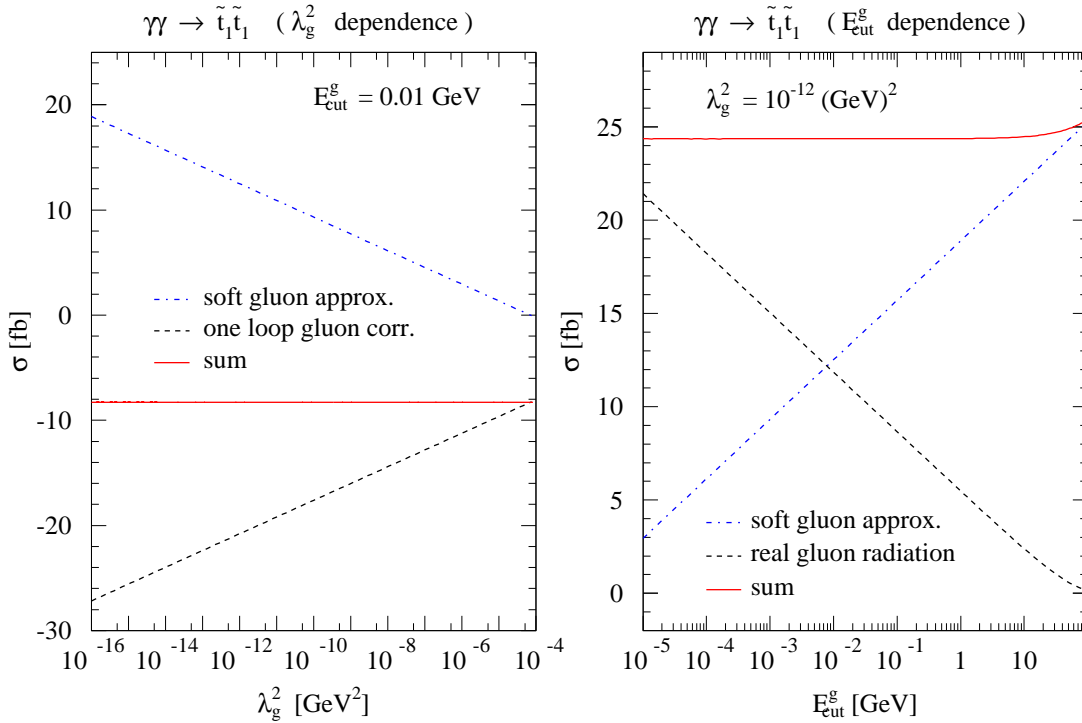
Figure 6.8: Dependence of the $\gamma\gamma$ cross section as a function of λ^2 (left panel) and as a function of E_{cut} (right panel). The SPS1 parameters are used and $\sqrt{s}_{\gamma\gamma} = 1000$ GeV.

and a center-of-mass energy of $\sqrt{s}_{\gamma\gamma} = 1000$ GeV has been chosen. The left plot shows the cross section as a function of λ^2 for a fixed E_{cut} while the right panel shows $\sigma_{\gamma\gamma}$

as a function of the cut-off energy for a fixed $\lambda = 10^{-6}$ GeV. The left plot of Fig. 6.8 shows that the sum of the virtual gluon corrections and the soft gluon factor (solid line) is almost stable and therefore independent of λ for a large range. The right plot shows the sum of the soft gluon factor and the hard gluon contribution (solid line) that is stable up to $E_{\rm cut} = 1$ GeV. For larger $E_{\rm cut}$ the soft photon approximation does not hold and a deviation is expected. For the further calculation $\lambda = 10^{-6}$ GeV and $E_{\rm cut} = 0.01$ GeV have been used.

The dependence of the photon and gluon one-loop correction is considered in Fig. 6.9 as a function of the $\gamma\gamma$ center-of-mass energy and the parameter points SPS1 and SPS5. The left panel shows the relative correction $\Delta\sigma = (\hat{\sigma} - \hat{\sigma}_0)/\hat{\sigma}_0$ of the one-
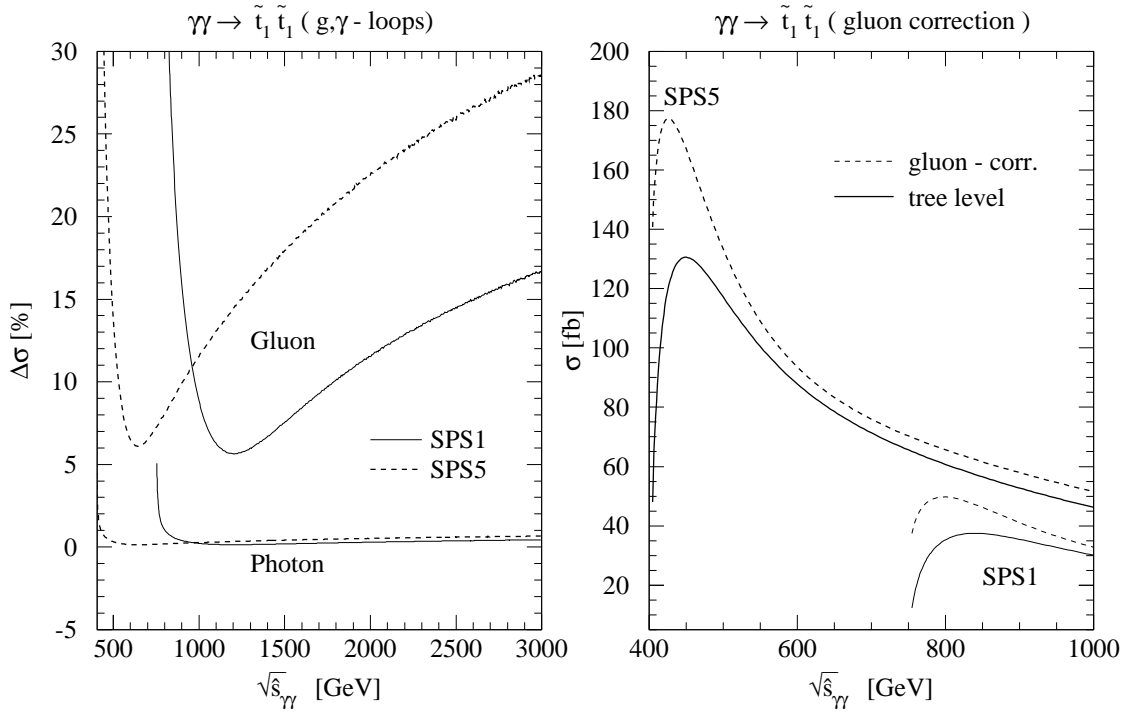
Figure 6.9: Dependence of the photon and gluon one-loop correction as a function of the $\gamma\gamma$ center-of-mass energy and the parameter points SPS1 and SPS5. Left: Relative correction $\Delta\sigma = (\hat{\sigma} - \hat{\sigma}_0)/\hat{\sigma}_0$ in %. Right: Gluon correction in fb as a function of the center-of-mass energy.

loop ($\hat{\sigma}$) and the tree level cross section ($\hat{\sigma}_0$) in %. As expected, the gluon radiative correction is much larger than the photon one. Except for a small region near the pair production threshold the photon correction is always below 1%. Whereas, the gluon corrections are always larger than 5% and reach 16.5% for large center-of-mass energies ($\sqrt{\hat{s}} = 3$ TeV) for the SPS1 point and 28.5% for the SPS5 point. At the squark pair production threshold the gluon and photon corrections grow up strongly, because of long-distance photon and gluon exchange between slowly moving final squarks. These Coulomb-singularities emerge in box diagrams with three internal squarks and one

photon/gluon. They are proportional to $\pi\alpha_s/\beta$ with $\beta = \sqrt{1 - 4m_{\tilde{t}}^2}$ and diverge at the production threshold since the perturbation expansion breaks down. However, because of the proportionality of the phase space to β the total cross section becomes finite at the threshold leading to a constant value [152]. This behavior would change if one would took into account the finite width of the squarks, but this is not included in this discussion.

For comparison with [35], in the right plot of Fig. 6.9 one can see again the NLO gluon correction and the leading order cross section for SPS1 and SPS5 as a function of the center-of-mass energy. The curve that is given for SPS5 with $m_{\tilde{t}_1} = 201.4$ GeV would not change much for $m_{\tilde{t}_1} = 200$ GeV, as used in Fig.2(a) of [35]. However, the shape is quite different because negative gluon corrections also occur in their figure. Moreover, their tree level cross section is much larger and can not be reproduced here. On the other hand, a very good agreement with the tree level cross sections of [143, 144] was found. One can conclude, no comparison with [35] can be performed.

6.2.2 One-Loop Corrections without Gluon and Photon

The one-loop Feynman diagrams without gluons and photons are box, vertex and self energy types. Fig. 6.10 shows some diagrams as examples for the full set of about
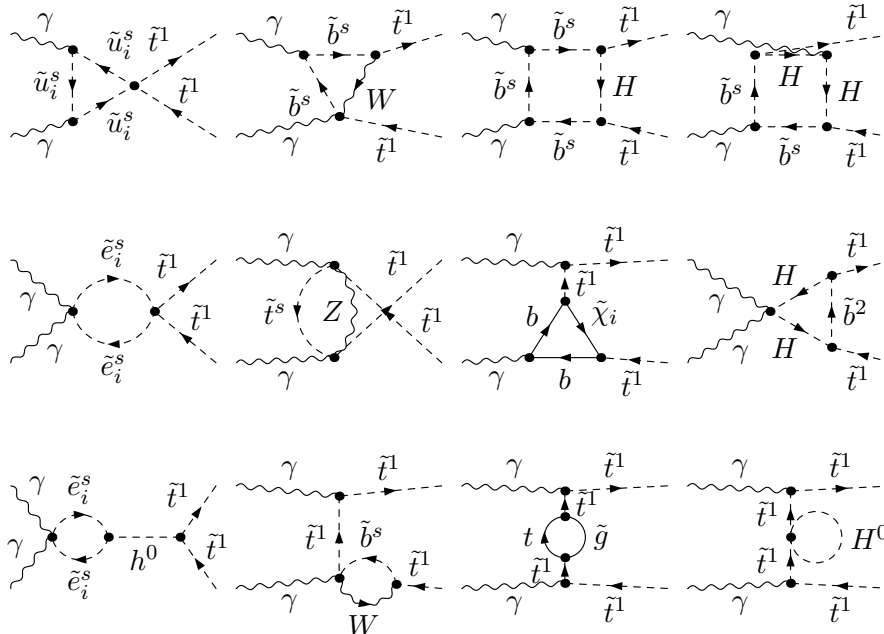
Figure 6.10: Typical Feynman diagrams for virtual gluon corrections.

400 classes of diagrams. A class means that e.g. $\tilde{u}_i$ in the first diagram of Fig. 6.10 is an abbreviation for all three up-type squarks and the squark mass eigenstates 1 and 2, together 6 Feynman diagrams (see FeynArts manual [102, 103]). Furthermore one has to calculate approximately 60 self-energy diagrams for the counterterms. Since all particles masses inside the loops are non-zero all loop integrals are IR-finite. To

obtain UV-finite matrix elements the counterterm diagrams have to be added with the renormalization factors defined in Section 2.5.4.

All Feynman diagrams and matrix elements have been generated with FeynArts and calculated with the programs described in Section 3.5.1 and Section 3.5.2. Further, the matrix elements were numerically compared with FormCalc and an agreement between 9 and 14 digits, depending on the type of diagram (box, self-energy, vertex), was found. Moreover, it was checked analytically and numerically that the UV-divergences cancel with the corresponding divergences of the counter-terms. This has been done separately for the box-, vertex- and self-energy diagrams.

In Fig. 6.11 the one-loop corrections are divided into the contributions with gluinos
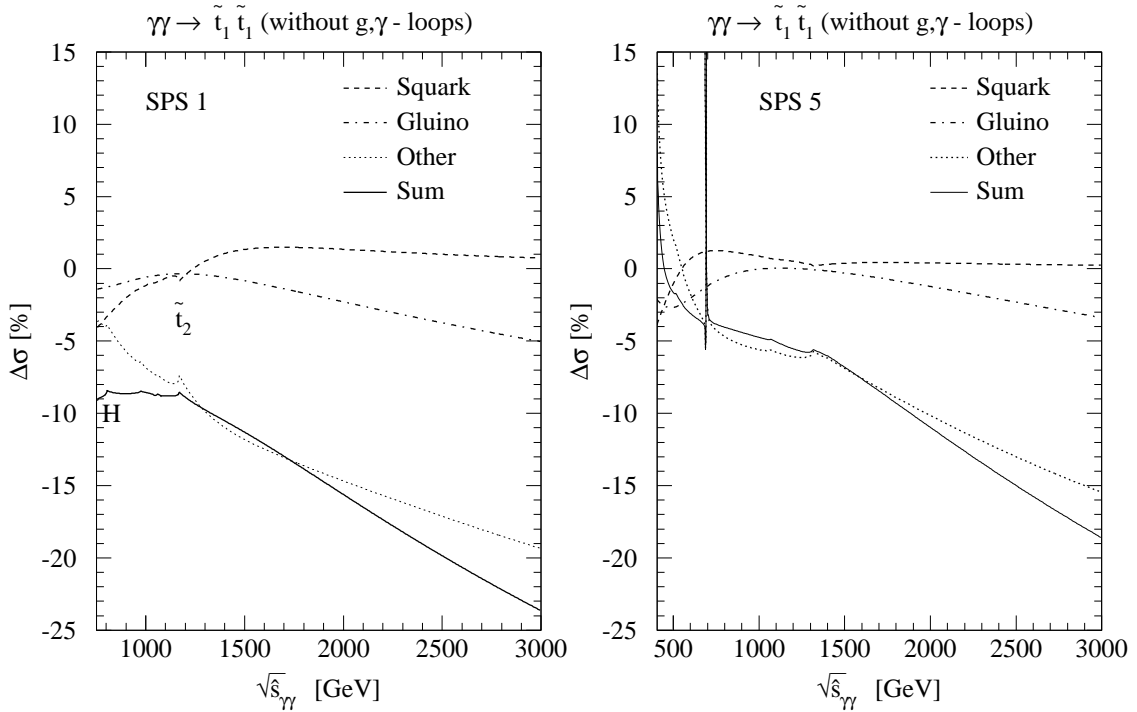
Figure 6.11: Dependence of the one-loop corrections due to diagrams with squark, gluino and weak interaction as a function of $\sqrt{\hat{s}}$. Left panel for parameter point SPS1, right panel for SPS5.

inside the loops, with only squarks and the weak corrections. There are only eight diagrams containing internal gluinos and only 18 containing squarks. Due to their proportionality to α_s, these corrections may become large. The figure shows the relative correction $\Delta\sigma = (\hat{\sigma} - \hat{\sigma}_0)/\hat{\sigma}_0$ for parameters of SPS1 (left panel) and SPS5 (right panel) as a function of the center-of-mass energy. The corrections due to gluino-loops are negative and reaches -5% for large $\sqrt{\hat{s}} = 3$ TeV. The corrections due to squark loops are of the same order, namely between -4 and $+1\%$. The remaining weak corrections become quite large, up to -20% for a large center-of-mass energy of $\sqrt{\hat{s}} = 3$ TeV, and in the case of SPS5 up to 10% near the threshold. This shows clearly that they can

not be neglected.

In Fig. 6.11 singularities and resonances occur. The singularities of the squark loop contribution (dashed line) arises from the first diagram of Fig. 6.12 if the center-of-
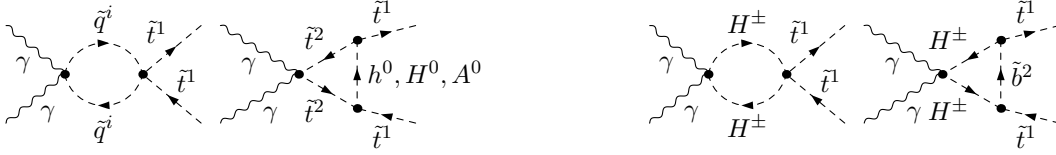
Figure 6.12: Normal threshold singularity Feynman graphs.

mass energy is equal the sum of the internal squark mass pair. In the left plot of Fig. 6.11 the singularity for $\tilde{q}_i = \tilde{t}_2$ with $m_{\tilde{t}_2} = 585$ GeV is indicated. The singularities for the down type squarks are shown as example in Fig. 6.12. They appear at 2 times $m_{\tilde{b}_1} = 486$ GeV, $m_{\tilde{d}_2,\tilde{s}_2} = 520$ GeV, $m_{\tilde{b}_2} = 530$ GeV, $m_{\tilde{d}_1,\tilde{s}_1} = 543$ GeV. The dotted line
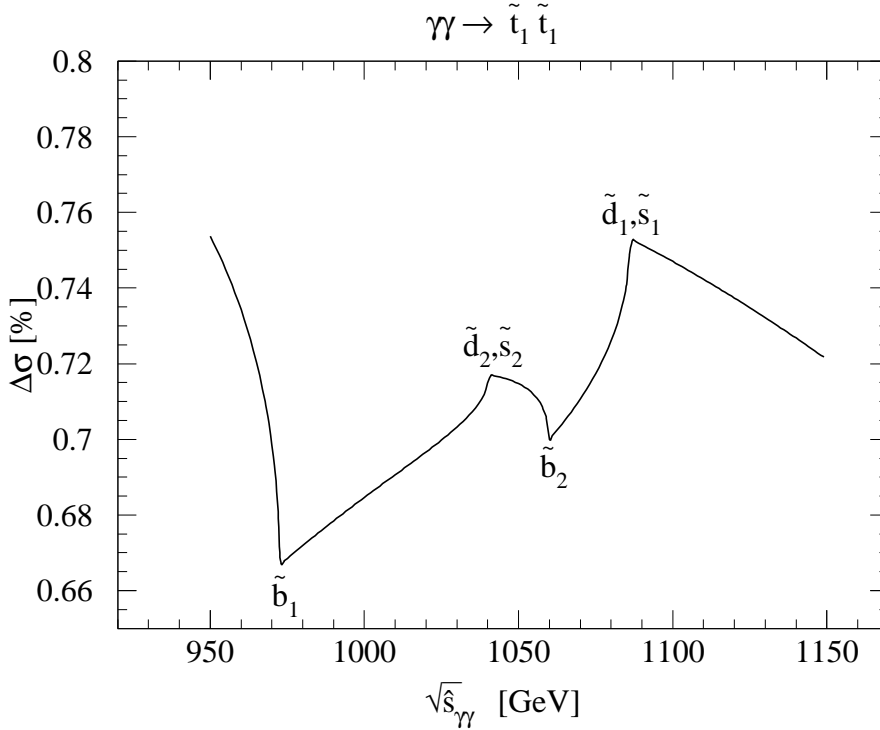
Figure 6.13: Normal threshold singularity of the first diagram in Fig. 6.12.

in the left plot of Fig. 6.11 shows also a threshold singularity at $2 \cdot m_{\tilde{t}_2} = 1179$ GeV. This threshold occurs due to the second Feynman diagram in Fig. 6.12 with two internal top squark 2 and a scalar Higgs boson, if the center-of-mass energy passes the $\tilde{t}_2\tilde{t}_2$ production threshold. The threshold at $\sqrt{s} = 803$ GeV (solid line) arises due to the third and fourth diagram in Fig. 6.12 where $\sqrt{s}$ becomes $2 \cdot m_{H^\pm}$.

The resonance shown in the right plot of Fig. 6.11 for SPS5 at 695 GeV arises due to the intermediate higgs bosons H^0 exchange in the s-channel diagram. The higgs bosons are produced on-shell leading to the shown divergence.
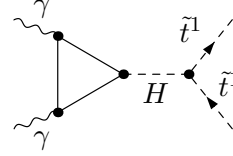
In Fig. 6.14 the center-of-mass energy was chosen at the point where the Born cross section is maximal. In the case of SPS1 this leads to $\sqrt{\hat{s}} = 850$ GeV and for SPS5 to $\sqrt{\hat{s}} = 450$ GeV. The figure shows $\Delta\sigma$ in percent as a function of the gluino mass (left
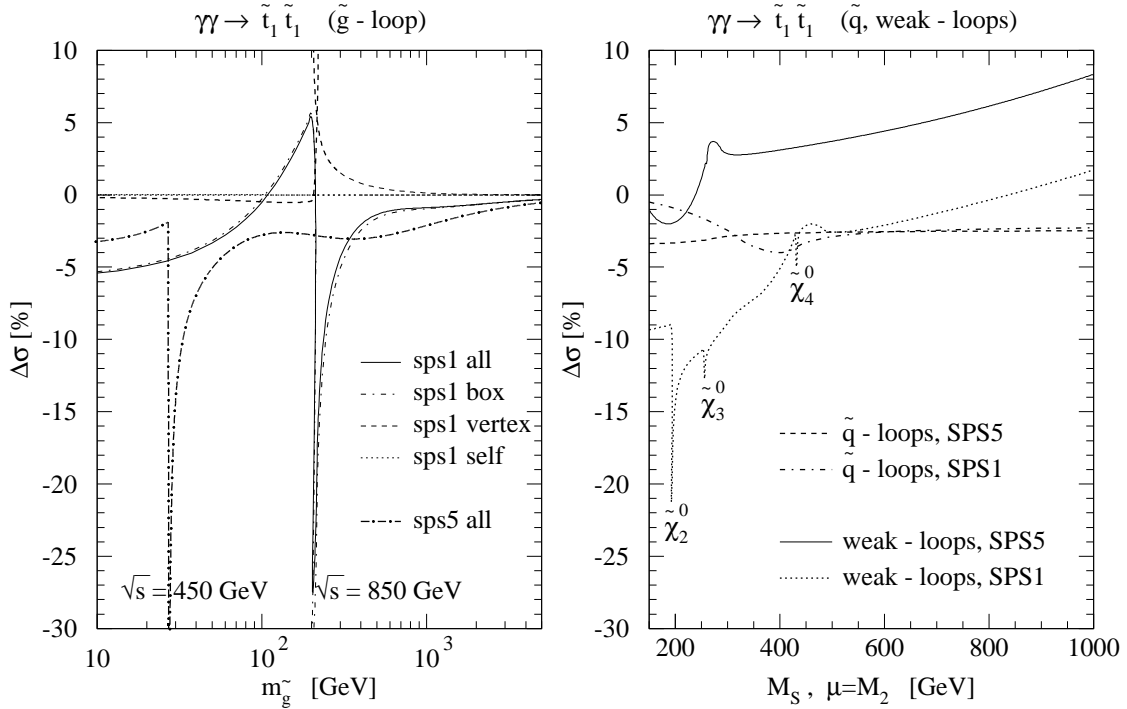
Figure 6.14: (SPS1: $\sqrt{s} = 450$ GeV, SPS5: $\sqrt{s} = 850$ GeV) Left: Dependence of the relative correction $\Delta\sigma$ as a function on the gluino mass. The dotted and dot-dashed lines show the contribution of the two box-diagrams, the other lines those from all 8 gluino diagrams. Right: The dashed and dot-dashed lines show the corrections of the squark-loop diagrams as a function of the squark mass parameter M_S. The solid and dotted lines represent the corrections of the weak-loop diagrams as a function of μ and M_2 with $\mu = M_2$.

figure) and as a function of either M_S or $\mu = M_2$ (right panel). The solid line and the thick dot-dashed line of the left plot show the gluino correction for SPS1 respectively SPS5, where all gluino diagrams are taken into account. The singularity occur if the mass relations

$$m_3 = m_1 + m_2 \tag{6.2}$$

for the diagrams like
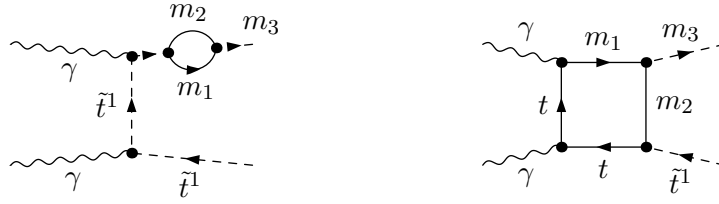
is fulfilled. The left diagram occurs due to the vertex counterterms. If the relation (6.2) holds the final on-shell particle, the stop squark 1, have the same mass as the sum of its decay particles. Experimentally one could not distinguish between the final squark and the decay products that would travel the same direction. For a consistent treatment one had to include the finite width of the final particles to handle the divergency. Furthermore, it should be noted that the one-loop correction might contain large errors if the particle mass spectrum nearly fulfills equation (6.2). The study of this effect should be an interesting future program.

For gluino masses of the remaining parameter space the corrections have a size of up to -3% and vanish for large gluino masses ($m_{\tilde{g}} = 5000$ GeV).

The dashed (SPS5) and dott-dashed (SPS1) lines in the right panel of Fig. 6.14 show the relative corrections as a function of the squark mass parameter M_S with $M_S = M_{\tilde{q}_L} = M_{\tilde{q}_R}$. Only the top-squark 1 mass was kept fixed. If $M_S \approx 300$ GeV is small, the corrections vary between -4% and 0%, they become stable at around -2.5% for large $M_S = 1000$ GeV due to the squark loops with a light top squark 1.

The figure also shows the dependence of the relative correction as a function of $\mu = M_2$ and it was set $M_1 = \frac{5}{3}\frac{s_W^2}{c_W^2} M_2$. Larger values of μ and M_2 lead to larger chargino and neutralino masses, and the variation of μ also leads to different mixing angles of the squarks. The corrections vary between -2% and 8% for SPS5, and between -12% and 2% for SPS1.

Furthermore, similar divergences as for the gluino corrections arises if $m_{\tilde{\chi}_i^0} + m_t = m_{\tilde{t}_1}$. That means, the corresponding loops contain the top quark and a neutralino. A singularity occur if the mass of the neutralino is $m_{\tilde{\chi}_i^0} = 201.67$ GeV. In the right plot of Fig. 6.14 is indicated which neutralino mass is equal to that value.

6.2.3 Total One-Loop Corrections

The sum of all corrections for the two parameter points are plotted in Fig. 6.15. The figure shows again the relative correction as a function of the photon center-of-mass energy. Closed to the threshold the corrections are dominated by the gluon exchange. The corrections for parameter point SPS5 are always larger than $+5\%$. For $\sqrt{\hat{s}} \geq 1200$ GeV they are stable at $+10\%$ because the gluon and weak corrections increase with opposite sign for increasing center-of-mass energies. The corrections for SPS1 are positive close to the production threshold and around -5% for larger $\sqrt{\hat{s}}$.
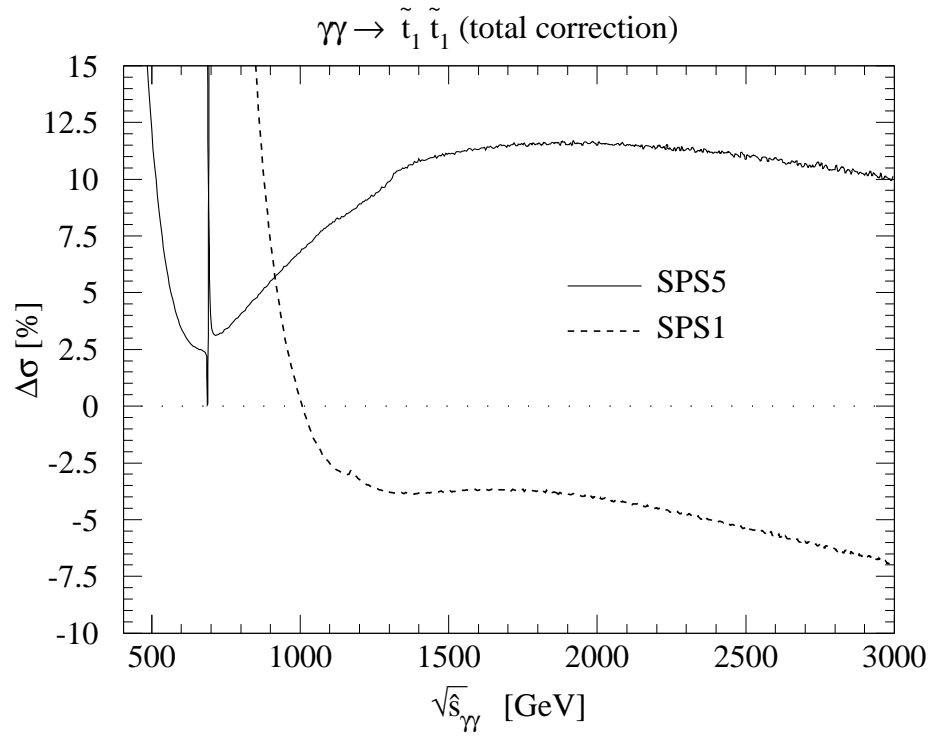
Figure 6.15: Full MSSM one-loop corrections as a function of the center-of-mass energy. The plot shows the relative correction $\Delta\sigma = (\hat{\sigma} - \hat{\sigma}_0)/\hat{\sigma}_0$ for SPS1(dashed line) and SPS5(solid line).

6.3 Resolved Contributions

Resolved processes contribute to the squark pair production in a similar manner like that discussed in Section 5.2 for gluino pair production. In case of squark pair production, both single resolved and double resolved diagrams occur already at tree level.

Fig. 6.16 shows the Feynman diagrams of the single resolved production channel. The
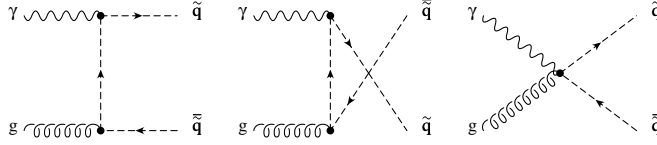
Figure 6.16: Leading order Feynman diagrams for single-resolved squark production in photon-photon collisions. Initial state quarks contribute only at next-to-leading order.

final squarks are either $\tilde{q}_1\tilde{q}_1^*$ or $\tilde{q}_2\tilde{q}_2^*$ states, no mixed states $\tilde{q}_1\tilde{q}_2^*$ are allowed. Apart from coupling constants the process depends at lowest order only on the final squark mass. The spin- and color-averaged squared matrix element is

$$\overline{|\mathcal{M}|}^2_{(\gamma g \to \tilde{q}_i \tilde{q}_i^*)} = 8\pi^2 e_q^2\, \alpha_e \alpha_s \frac{1}{N_c} \frac{(\breve{t} - m_{\tilde{q}_i}^2)^2(\breve{u} - m_{\tilde{q}_i}^2)^2 - 2m_{\tilde{q}_i}^2(\breve{t} - m_{\tilde{q}_i}^2)(\breve{u} - m_{\tilde{q}_i}^2)\breve{s} + m_{\tilde{q}_i}^4 \breve{s}^2}{(\breve{t} - m_{\tilde{q}_i}^2)^2(\breve{u} - m_{\tilde{q}_i}^2)^2},$$

where $i = \{1,2\}$, $N_C = 3$ denotes the number of colors and $\breve{s}$, $\breve{u}$, $\breve{t}$, are the Mandelstam variables of the $2 \to 2$ scattering process.

In Fig. 6.17 are shown the Feynman diagrams contributing at $\mathcal{O}(\alpha_s^2)$ when photons resolve into their hadronic content. As mentioned before, due to the heavy top mass,
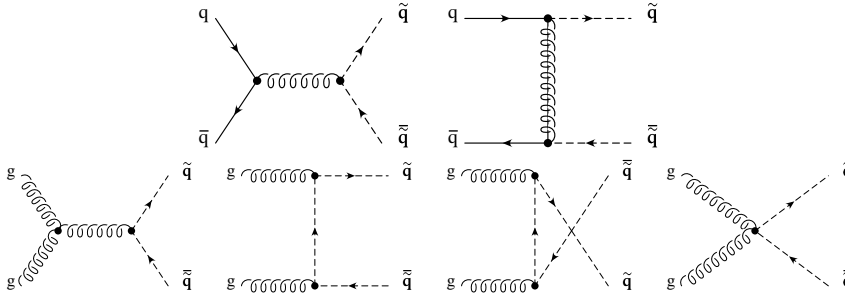
Figure 6.17: Leading order Feynman diagrams for double-resolved squark production in photon-photon collisions.

there is almost no top quark inside the photon, and for the same reason the bottom distribution is strongly suppressed with respect to the light flavors. Since mixing of the squarks of the first two generations can be neglected the process at tree level is independent of mixing effects. The diagram with gluino exchange is mostly important for production of up-type squarks because the density function of up-quarks in the photon is significantly larger than that for the other flavors. Furthermore, mixed final states $\tilde{q}_L\tilde{q}_R^*$ appear because of this diagram.

The spin- and color-averaged matrix elements squared for the process $q\bar{q} \to \tilde{q}_i \tilde{q}_j^*$ is for one flavor

$$\overline{|\mathcal{M}|}^2_{(q\bar{q} \to \tilde{q}_i \tilde{q}_j^*)} = 32\pi^2 \alpha_s^2 C_F \frac{\delta_{ij}}{N_C} \left[\frac{(\check{t} - m_{\tilde{q}_i}^2)(\check{u} - m_{\tilde{q}_i}^2) - m_{\tilde{q}_i}^2 \check{s}}{\check{s}^2} - \frac{(\check{t} - m_{\tilde{q}_i}^2)(\check{u} - m_{\tilde{q}_i}^2) - m_{\tilde{q}_i}^2 \check{s}}{N_C \check{s}(t - m_{\tilde{g}}^2)} \right]$$

$$+ 16\pi^2 \alpha_s^2 C_F \frac{1}{N_C} \left[\frac{(\check{t} - m_{\tilde{q}_i}^2)(\check{u} - m_{\tilde{q}_i}^2) - (m_{\tilde{q}_i}^2 - m_{\tilde{g}}^2)\check{s}}{(t - m_{\tilde{g}}^2)^2} \right],$$

where $C_F = (N_c^2 - 1)/(2N_c)$. The squared matrix element for the gluon fusion is

$$\overline{|\mathcal{M}|}^2_{(gg \to \tilde{q}_i \tilde{q}_i^*)} = \frac{8\pi^2 \alpha_s^2}{C_F} \left[1 - 2\frac{(\check{t} - m_{\tilde{q}_i}^2)(\check{u} - m_{\tilde{q}_i}^2)}{\check{s}^2} - \frac{1}{N_c^2} \right]$$

$$\times \left[1 - 2\frac{\check{s}m_{\tilde{q}_i}^2}{(\check{t} - m_{\tilde{q}_i}^2)(\check{u} - m_{\tilde{q}_i}^2)} \left(1 - \frac{\check{s}m_{\tilde{q}_i}^2}{(\check{t} - m_{\tilde{q}_i}^2)(\check{u} - m_{\tilde{q}_i}^2)} \right) \right].$$

Again, the quarks and gluon density functions [137] which are implemented in the PDFLIB 8.0 [73] were used for the numerical calculation. Fig. 6.18 shows the unpolarized $\gamma\gamma \to \tilde{u}_L \tilde{u}_L^*$ cross section as a function of the center-of-mass energy for a squark mass of 200 GeV (left panel) and a heavier squark mass of 500 GeV (right panel). Thus,
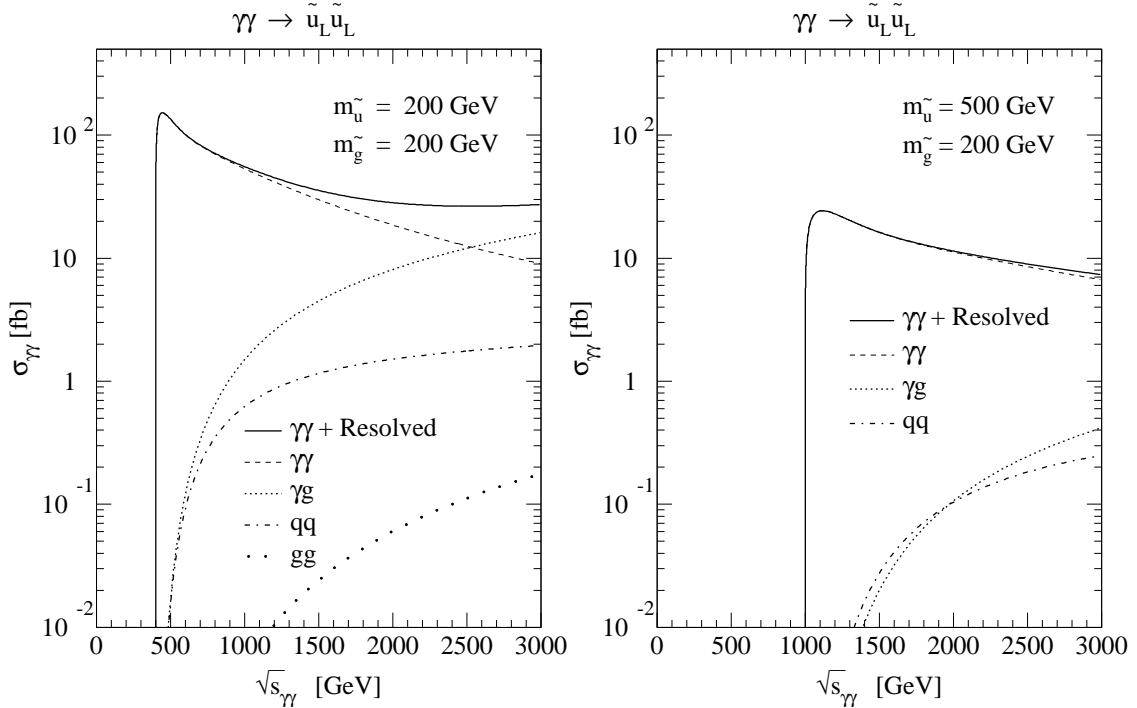
Figure 6.18: Unpolarized $\gamma\gamma$ cross section as a function of the photon center-of-mass energy for up-type squark masses of 200 GeV (left panel) and 500 GeV (right panel). The solid line shows the sum of the direct contribution and all resolved ones.

the σ was convoluted with quark and gluon densities inside the photon. Because of the shape of this density functions, the cross section at the production threshold is small and can be neglected. The resolved contribution becomes important and can be larger than the direct $\gamma\gamma$ production channel for small squark masses lower than 200 GeV and high energies above 2 TeV. As one would expect, the dominant resolved contribution is always the single resolved production process. The double resolved $q\bar{q}$ production (dot-dashed line) also contains the diagram with gluino exchange and therefore depends on the gluino mass. However, this diagrams contributes only significant for $\tilde{u}\tilde{u}^*$ production (see Fig. 6.17), because the dominant resolved $q\bar{q}$ contributions originates always from initial $u\bar{u}$ scattering due to the largest parton distribution function. The $q\bar{q}$-cross section for other final flavor is therefore smaller roughly by a factor of 2. It is also for the $\tilde{u}\tilde{u}^*$ production smaller by a factor of 2 if the gluino mass increases to about 500 GeV.

For larger squark masses (500 GeV) the resolved contributions are strongly suppressed and only reach a few percent, this is also true for larger center-of-mass energies. Furthermore, the gluon fusion channel is negligible in all cases.
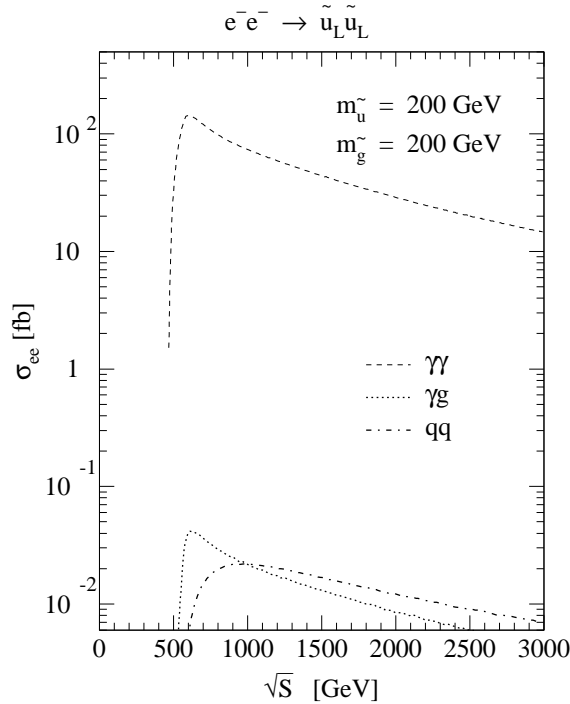
Figure 6.19: Total unpolarized electron-electron cross section as a function of the electron center-of-mass energy for pair production of left handed up-type squarks. The minimum required energy of the final state is $\sqrt{s}_{\gamma\gamma}^{min} = 0.8 \cdot 0.867 \cdot \sqrt{S}_{e^-e^-}$. The gluon fusion contribution is tiny. The curves are normalized to the high energy photon peak.

The total energy of the final squarks is mostly smaller for resolved processes than for

the direct process. This is caused by the density functions of the quarks and gluon that become large only for small $y = E_{q,g}/E_\gamma$. They have to be added together with the low energy part of the photon density function for the direct channel, which is badly known. Thus, a cut on the total final energy is assumed, and this will suppress the resolved pair production cross section further as shown in Fig. 6.19. The total unpolarized electron-electron cross section is shown as a function of the electron center-of-mass energy and squark masses of 200 GeV. The minimum required energy of the final state is chosen to be 0.8 of the maximum available $\gamma\gamma$ energy: $\sqrt{s_{\gamma\gamma}^{min}} = 0.8 \cdot 0.867 \cdot \sqrt{S_{e^-e^-}}$. Then the resolved contributions are negligible even in the case of center-of-mass energies far above the pair production threshold.

Chapter 7

Conclusion

In this thesis the gluino pair production in electron-positron annihilation and in photon-photon scattering were considered. Furthermore, the full MSSM-NLO corrections to squark pair production in photon-photon collisions were calculated. For this purpose a computer program, based on Mathematica and Form, was developed to perform the analytical calculations in an automatic way. For the numerical calculation a corresponding Fortran program has been written. Additionally, all results were compared with existing computer tools [123].

The gluino pair production in electron-positron annihilation, described in Chapter 4, occurs only at the one loop level. The contributions to the cross section of up- and down-quarks of each generation interfere destructively due to the opposite isospin and charge. Unfortunately, the contributions of the squark mass eigenstates 1 and 2 of each flavor also interfere destructively. Therefore, pair production become invisible for future linear colliders [21, 22, 105, 106] in nearly the whole parameter space. Only for gluino masses of 200 GeV and large top splitting with a light top squark 1 of around 100 GeV would one obtain a couple of events (up to 65/year). Therefore, a detection seams improbable.

The gluino pair production in photon-photon scattering, described in Chapter 5, also starts at the one loop level. The diagrams interfere constructively because of even numbers of couplings inside the loops. Assuming a photon-photon collider luminosity of $330\,fb^{-1}$, cross sections give up to 6000 events/year for light gluino masses of 300 GeV and small squark masses of 350 GeV. For larger squark masses up to 600 GeV still 330 events/year are expected. A similar number of 330 events per year is obtained if the gluino mass is increased to 1700 GeV and the squark masses up to 800 GeV. Therefore, if the necessary center-of-mass energy is available, gluino pair production in photon-photon collisions is visible in a large range of parameters space. Furthermore, at a photon collider it might be possible to increase the luminosity leading to a larger number of events.
In addition to the direct scattering channel, resolved gluino pair production processes were considered. These processes become important for light gluino masses around 200 GeV. If the masses of the squarks are around 350 GeV, the resolved cross section becomes of the same order as the direct channel for energies far above the production

threshold (1 TeV). If the squarks are heavy (1500 GeV), the cross section is up to 3 orders of magnitude larger than the direct process.

The squark pair production process in photon-photon collisions was discussed in Chapter 6. This scattering type already occurs at tree level, therefore large cross sections are obtained, comparable with those in electron-positron annihilation.
The MSSM one-loop corrections to this process were calculated and their influence on two benchmark points SPS1 and SPS5 was studied. The gluon corrections are dominant close to the production threshold due to the Coulomb singularity. Above the production threshold they are always larger than $+5\%$ and increase for higher center-of-mass energies, i.e. for 3 TeV, to $+16\%$ for SPS1 and to $+28\%$ for SPS5. The corrections from photon exchange are small. The contributions due to gluino and squark exchange are of a few percent and mostly smaller than the remaining electroweak corrections. The weak corrections near the production threshold contribute between $\pm10\%$. Increasing the center-of-mass energy to 3 TeV they become more than -20% for the two parameter points. The gluon and weak loop contributions cancel each other to a flat correction (for SPS1 -5%, for SPS5 $+10\%$) for a large energy range. Therefore, for precise measurements all one-loop diagrams have to be considered.
Furthermore, the resolved contributions to the squark pair production were calculated. They are only important for small squark masses of 200 GeV and center-of-mass energies far above the production threshold.

Outlook: The results of the gluino and squark pair production in photon-photon scattering can be used for further detailed studies. Using appropriate decay modes one can determine with which precision squarks and gluinos can be measured at a photon collider.

Appendix A

Conventions

Throughout this thesis natural units $\hbar = c = 1$ are used. Also the Einstein sum convention is applied, that means, it is summed over indices appearing twice. Greece indices run from 0 to 3, latin letters a,b,c,d,e are used for color algebra and run from 1 to $(N^2 - 1)$, whereas i,j,... run from 1 to 3.

A.1 Minkowski Space

A four-vector in space and time is defined by its contravariant components

$$x^\mu = (t, \vec{x}) = (x^0, x^1, x^2, x^3) \quad \text{with} \quad \mu = 0, 1, 2, 3.$$

The Minkowski space has the metric $g^{\mu\nu} = \text{diag}(1, -1, -1, -1)$ with $g_{\mu\nu} = g^{\mu\nu}$ and $g_{\mu\nu}\,g^{\nu\rho} = \delta^\rho_\mu$. The scalar product is defined as

$$p\,x = p^\mu x_\mu = g_{\mu\nu}p^\mu x^\nu = p^0 x^0 - \vec{p}\vec{x} \,, \qquad p^\mu = i\,\partial^\mu = i\frac{\partial}{\partial x_\mu} = \left(i\frac{\partial}{\partial t}, \frac{1}{i}\vec{\nabla} \right)$$

x_μ is called the covariant four-vector. Transformations of arbitrary four-vectors and tensors are done with the metric tensor by

$$T^{\mu\nu} = g^{\mu\rho}g^{\nu\sigma}T_{\rho\sigma} \quad \text{and} \quad T_\nu{}^\mu = g_{\nu\rho}T^{\rho\mu}$$

A.2 Dirac Algebra

The γ-matrices fullfil the Clifford-Algebra

$$\{\gamma^\mu, \gamma^\nu\} = 2g^{\mu\nu} \tag{A.1}$$

that is in Minkowski space $(\gamma^0)^2 = \mathbb{1}$ and $(\gamma^i)^2 = -\mathbb{1}$. The contraction of a four-vector with a γ-matrix has the conventional abbreviation $\gamma_\mu p^\mu = \not{p}$ and the relations $\not{p}\not{p} = p^2$ and $\not{p}\not{k} = 2(pk) - \not{k}\not{p}$ holds. Furthermore the matrix γ_5 is defined by

$$\{\gamma^\mu, \gamma^5\} = 0 \,, \qquad \gamma_5 = \gamma^5 = i\gamma^0\gamma^1\gamma^2\gamma^3 \,, \qquad (\gamma_5)^2 = \mathbb{1}$$

In the Dirac-representation the γ-matrices are given as

$$\gamma^0 = \begin{pmatrix} 1 & 0 \\ 0 & -1 \end{pmatrix} \quad \boldsymbol{\gamma} = \begin{pmatrix} 0 & \boldsymbol{\sigma} \\ -\boldsymbol{\sigma} & 0 \end{pmatrix}, \quad \gamma^5 = \begin{pmatrix} 0 & 1 \\ 1 & 0 \end{pmatrix},$$

where σ denotes the Pauli-matrices. With γ^5 one can defines the projectors

$$\omega_L = \omega_- = (1 - \gamma_5)/2 \quad \text{and} \quad \omega_R = \omega_+ = (1 + \gamma_5)/2 \tag{A.2}$$

that extract the left- and right-handed part of a spinor.
If $u_\lambda(p)$ and $v_\lambda(p)$ are spinors for fermion and antifermion with spin λ and momentum p, the Dirac equation reads:

$$(\not{p} - m)u_\lambda(p) = 0, \qquad (\not{p} + m)v_\lambda(p) = 0 \tag{A.3}$$

To calculate polarized cross sections with fermions in the initial state the relation [123]

$$\{u_\lambda(p)\overline{u}_\lambda(p), v_\lambda(p)\overline{v}_\lambda(p)\} = \begin{cases} \frac{1}{2}(\mathbb{1} \pm \lambda\gamma^5)\not{p} & \text{for massless fermions} \\ \frac{1}{2}(\mathbb{1} + \lambda\gamma^5\not{s})(\not{p} \pm m) & \text{for massive fermions} \end{cases}$$

is needed. The plus sign refers to the $u\overline{u}$ and the minus sign to $v\overline{v}$. $\lambda = \pm 1$ is the helicity and s is the unit vector in the direction of the spin axis in the particle rest frame, boosted into the CMS. s fulfills the condition $s\dot{p} = 0$ and $s^2 = -1$. The unpolarized formula is received by setting $\lambda = 0$ and multiply by 2.

The charge-conjugation matrix C fulfills

$$C^\dagger = C^{-1}, \qquad C^T = -C, \tag{A.4}$$

that leads to (no summation over i) [132]

$$\Gamma' = C\Gamma_i^T C^{-1} = \eta_i \Gamma_i, \qquad \text{with} \quad \eta_i = \begin{cases} 1 & \text{for } \Gamma_i = 1, \, i\gamma_5, \, \gamma_\mu\gamma_5 \\ -1 & \text{for } \Gamma_i = \gamma_\mu, \, \sigma_{\mu\nu} \end{cases} \tag{A.5}$$

While calculating Feynman diagrams traces of γ-matrices occur. To calculate them the following relations have been used:

$$Tr[\mathbb{1}] = 4, \qquad\qquad Tr[\gamma^\mu\gamma^\nu\gamma^\rho\gamma^\sigma] = 4(g^{\mu\nu}g^{\rho\sigma} + g^{\mu\sigma}g^{\nu\rho} - g^{\mu\rho}g^{\nu\sigma}),$$
$$Tr[\gamma^\mu\gamma^\nu] = 4g^{\mu\nu}, \qquad\qquad Tr[\gamma^5\gamma^\mu\gamma^\nu\gamma^\rho\gamma^\sigma] = -4\,i\,\varepsilon^{\mu\nu\rho\sigma},$$
$$Tr[\gamma^{\mu_1}\ldots\gamma^{\mu_{2n+1}}] = 0, \qquad\qquad Tr[\gamma^5\gamma^{\mu_1}\ldots\gamma^{\mu_i}\,;\,i < 4] = 0,$$

where $\varepsilon^{\mu\nu\rho\sigma}$ is the total antisymmetric Levi-Civita-Tensor defined by

$$\varepsilon^{\mu\nu\rho\sigma} = -\varepsilon_{\mu\nu\rho\sigma} = \begin{cases} +1 & \text{if } \{\mu, \nu, \rho, \sigma\} \text{ is an even permutation of } \{1, 2, 3, 4\} \\ -1 & \text{if } \{\mu, \nu, \rho, \sigma\} \text{ is an odd permutation of } \{1, 2, 3, 4\} \\ 0 & \text{otherwise} \end{cases}$$

Another used operator is

$$f \overleftrightarrow{\partial_\mu} g = f\,\partial_\mu g - \partial_\mu f \cdot g \tag{A.6}$$

A.3 Dirac Matrices in D Dimensions

To regularize the divergent tensor integrals the dimension of space-time is continued to $D = 4 - \epsilon$. Then the Dirac-matrices has to be evaluated in D dimensions. The γ-matrices fulfills

$$\{\gamma^\mu, \gamma^\nu\} = 2g^{\mu\nu}$$

The following relations hold:

$$g_{\mu\nu}g^{\mu\nu} = \delta^\mu_\mu = D \ ,$$
$$\gamma_\rho\gamma^\rho = \frac{1}{2}g_{\mu\rho}\{\gamma^\mu, \gamma^\rho\} = D \ ,$$
$$\gamma_\rho\gamma^\mu\gamma^\rho = (2 - D)\,\gamma^\mu \ .$$
$$\gamma_\rho\gamma_\mu\gamma_\nu\gamma^\rho = 4g_{\mu\nu} - (4 - D)\gamma_\mu\gamma_\nu \ ,$$
$$\gamma_\rho\gamma_\mu\gamma_\nu\gamma_\sigma\gamma^\rho = -2\gamma_\sigma\gamma_\nu\gamma_\mu + (4 - D)\gamma_\mu\gamma_\nu\gamma_\sigma \ ,$$
$$\gamma_\rho\gamma_\mu\gamma_\nu\gamma_\sigma\gamma_\kappa\gamma^\rho = 2(\gamma_\kappa\gamma_\mu\gamma_\nu\gamma_\sigma + \gamma_\sigma\gamma_\nu\gamma_\mu\gamma_\kappa) - (4 - D)\gamma_\mu\gamma_\nu\gamma_\sigma\gamma_\kappa \ .$$

Higher contractions $\gamma_\rho\gamma^\mu\gamma^\nu \ldots \gamma^\rho$ can be derived by these relations.

A.4 One Loop Tensor Integrals

For the calculation of the tensor integrals the convention of [150] is used. Fig. A.1 shows the momentum and mass definitions for an arbitrary one-loop integral. Note that all external momenta are incoming.
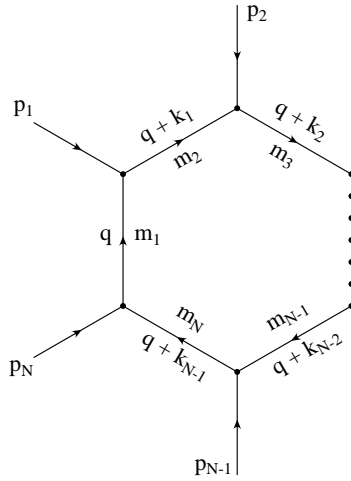
Figure A.1: Convention for the N-point tensor integrals.

The integrals belonging to this graph are given by:

$$T^N_{\{\mu_1\dots\mu_i\}}(k_1\dots k_{N-1};m_1\dots m_N) =$$
$$\int_{-\infty}^{+\infty}d^Dq\,\frac{(2\pi\mu)^{4-D}}{i\pi^2}\,\frac{\{q_{\mu_1}\dots q_{\mu_i}\}}{[q^2-m_1^2][(q+k_1)^2-m_2^2]\dots[(q+k_{N-1})^2-m_N^2]}$$

The external momenta are related to the internal one by the relations:

$$p_1 = k_1, \quad p_2 = k_2 - k_1, \quad \dots, \quad p_N = k_N - k_{N-1}$$

$$k_1 = p_1, \quad k_2 = p_1 + p_2, \quad \dots, \quad k_N = \sum_{i=1}^{N} p_i. \tag{A.7}$$

The Tensor integrals can be decomposed:

$$B_\mu = k_{1\mu}B_1 , \qquad\qquad B_{\mu\nu} = k_{1\mu}k_{1\nu}B_{11} + g_{\mu\nu}B_{00} ,$$

$$C_\mu = \sum_{i=1}^{2} k_{i\mu}C_i , \qquad\qquad C_{\mu\nu\rho} = \sum_{i=1}^{2}(g_{\mu\nu}k_{i\rho} + g_{\nu\rho}k_{i\mu} + g_{\mu\rho}k_{i\nu})C_{00i}$$

$$C_{\mu\nu} = \sum_{i,j=1}^{2} k_{i\mu}k_{j\nu}C_{ij} + g_{\mu\nu}C_{00} , \qquad\qquad + \sum_{i,j,l=1}^{2} k_{i\mu}k_{j\nu}k_{l\rho}C_{ijl} ,$$

$$D_\mu = \sum_{i=1}^{3} k_{i\mu}D_i , \qquad\qquad D_{\mu\nu} = \sum_{i,j=1}^{3} k_{i\mu}k_{j\nu}D_{ij} + g_{\mu\nu}D_{00} ,$$

$$D_{\mu\nu\rho} = \sum_{i,j,l=1}^{3} k_{i\mu}k_{j\nu}k_{l\rho}D_{ijl} + \sum_{i=1}^{3}(g_{\mu\nu}k_{i\rho} + g_{\nu\rho}k_{i\mu} + g_{\mu\rho}k_{i\nu})D_{00i} ,$$

$$D_{\mu\nu\rho\sigma} = \sum_{i,j,l,n=1}^{3} k_{i\mu}k_{j\nu}k_{l\rho}k_{n\sigma}D_{ijln} + \sum_{i,j=1}^{3}(g_{\mu\nu}k_{i\rho}k_{j\sigma} + g_{\nu\rho}k_{i\mu}k_{j\sigma} + g_{\mu\rho}k_{i\nu}k_{j\sigma} + g_{\mu\sigma}k_{i\nu}k_{j\rho}$$
$$+ g_{\nu\sigma}k_{i\mu}k_{j\rho} + g_{\rho\sigma}k_{i\mu}k_{j\nu})D_{00ij} + (g_{\mu\nu}g_{\rho\sigma} + g_{\mu\rho}g_{\nu\sigma} + g_{\mu\sigma}g_{\nu\rho})D_{0000} .$$
$$\tag{A.8}$$

Some of the received integrals are UV and IR Divergent. That means ... In the $\overline{\text{MS}}$ scheme one defines the UV Divergence Δ

$$\Delta = \frac{2}{\varepsilon} - \gamma_E + \log(4\pi)$$

with the Euler-Mascheroni constant $\gamma_E = 0,5772157\dots$. By use of Δ one can divide the tensor integrals into a part containing the divergence and a finite part. The divergent parts up to 4 point integrals are

$$A^\Delta(m_1) = m_1^2\,\Delta \qquad\qquad\qquad B_{11}^\Delta = \frac{1}{3}\Delta$$

$$B_0^\Delta = \Delta \qquad\qquad\qquad C_{00}^\Delta = \frac{1}{4}\Delta$$

$$B_1^\Delta = -\frac{1}{2}\Delta \qquad\qquad\qquad C_{001}^\Delta = C_{002}^\Delta = -\frac{1}{12}\Delta$$

$$B_{00}^\Delta(k_1^2,m_1,m_2) = \frac{1}{12}\left(3m_1^2 + 3m_2^2 - k_1^2\right)\Delta \qquad\qquad D_{0000}^\Delta = \frac{1}{24}\Delta$$

All other integrals up to order N = 4 are finite.

A.5   SU(N)

The group SU(N) is built by the algebra

$$[T^a, T^b] = i f^{abc} T^c \ ,$$

with the hermitian, traceless generators $T^a (a = 1, 2, \ldots, N^2 - 1)$ and the structure constant f^{abc}. After normalization: $\text{Tr}(T^a T^b) = 1/2 \delta^{ab}$, the structure constant fulfill the relation:

$$i f^{abc} = 2 \text{Tr}\left([T^a, T^b] T^c \right). \tag{A.9}$$

A large set of relations to calculate SU(N) factors can be found in [153].
The SU(N) algebra is needed to calculate the color factors appearing in scattering processes with colored particles. In case of a large number of Feynman diagrams one will also have a large set of different color factors. It is useful to automatize and integrate the calculation into a computer program. Normally one tries to collect the generators T^a to products of traces and solve this by certain relations. The disadvantage of this map is the large number of relations that would appear especially for d^{abc} and f^{abc} (d^{abc} is defined by $d^{abc} = 2\text{Tr}(\{T^a, T^b\}T^c)$. On the other side one could incorporate the numeric Gell-Mann matrices and values of the d^{abc} and f^{abc}. But this would limit one to the case of SU(3).
Another road-map for SU(N) that is used and implemented in a computer program reads as follow (assuming a given factor with the elements f^{abc}, δ^{ab}, δ_{ij}, T^a_{ij} and traces of $T^a T^b$...):

- Use the relation (A.9) means $f^{abc} = -2i \, \text{Tr}\left(T^a T^b T^c \right) + 2i \, \text{Tr}\left(T^b T^a T^c \right)$ to eliminate all structure constants

- Write all traces $\text{Tr}\left(T^a T^b ... T^c \right)$ in component form: $\sum_{i,j,k,\ldots,l}^{N} T^a_{ij} T^b_{jk} .... T^c_{li}$

- Absorb all δ^{ab} and use relation $\sum_a^{(N^2 - 1)} T^a_{ij} T^a_{kl} = \frac{1}{2}(\delta_{il}\delta_{jk} - \frac{1}{N}\delta_{ij}\delta_{kl})$

- At least calculate the only remaining δ's by use of $\sum_j^{N} \delta_{ij}\delta_{jk} = \delta_{ik}$ and $\sum_i^{N} \delta_{ii} = N$

These are the only needed relations. To optimize them and safe computer calculation time one should also include the relations: $f^{aab} = 0$, $(f^{abc})^2 = N(N^2 - 1)$, $f^{abc} f^{ebc} = N\delta^{ae}$, $i f^{abc} T^c_{ij} = [T^a, T^b]_{ij}$, $T^a_{ii} = 0$, $T^a_{ij} T^a_{jk} = (N^2 - 1)/(2N)\delta_{ik}$ and $\delta^{aa} = N^2 - 1$. To absorb δ-functions as far as possible is obvious.
The remaining result will only depend on N.

If one calculates colored scattering processes in the MSSM automatically with software like Mathematica one has to be careful with selecting the color factors. In SM QCD for one single amplitude one could easily search for all color elements, kill doubles and write them in front of the amplitude. In MSSM this is not possible because sums with different color terms in one single coupling can occur e.g. in the 4-squark coupling.

Appendix B

SPS Parameters

This appendix shows the MSSM input parameters for the SPS1 and SPS5 point of the Snowmass workshop [136] taken from [154]. The masses and mixing angles were calculated using the model-file of FormCalc [123] version 3.0. The neutralino and chargino mixing matrices are not denoted.

B.1   SPS 1

The MSSM input parameter of SPS 1 are:

$$
\begin{aligned}
&M_{\tilde{e}_L,\tilde{\mu}_L} && = 196.64 \text{ GeV}, && M_{\tilde{e}_R,\tilde{\mu}_R} = 136.23 \text{ GeV}, \\
&M_{\tilde{\tau}_L} && = 195.75 \text{ GeV}, && M_{\tilde{\tau}_R} && = 133.55 \text{ GeV}, && A_\tau && = -254.20 \text{ GeV}, \\
&M_{\tilde{u}_L,\tilde{d}_L,\tilde{c}_L,\tilde{s}_L} && = 539.86 \text{ GeV}, && M_{\tilde{u}_R,\tilde{c}_R} = 521.66 \text{ GeV}, \\
&&&&& M_{\tilde{d}_R\tilde{s}_R} && = 519.53 \text{ GeV}, \\
&M_{\tilde{t}_L,\tilde{b}_L} && = 495.91 \text{ GeV}, && M_{\tilde{t}_R} && = 424.83 \text{ GeV}, && A_t && = -510.01 \text{ GeV}, \\
&&&&& M_{\tilde{b}_R} && = 516.86 \text{ GeV}, && A_b && = -772.66 \text{ GeV}, \\
&\mu && = 352.39 \text{ GeV}, && M_{A^0} && = 393.63 \text{ GeV}, && \tan\beta = 10 \text{ GeV}, \\
&m_{\tilde{g}} && = 595.19 \text{ GeV}, && M_1 && = 99.13 \text{ GeV}, && M_2 && = 192.74 \text{ GeV}.
\end{aligned}
$$

The following masses and mixing angles arises:

Fermions:

$$m_{\tilde{e}_1} = 202.32 \text{ GeV}, \qquad m_{\tilde{e}_2} = 142.72 \text{ GeV},$$
$$m_{\tilde{\mu}_1} = 202.32 \text{ GeV}, \qquad m_{\tilde{\mu}_2} = 142.72 \text{ GeV},$$
$$m_{\tilde{\tau}_1} = 132.97 \text{ GeV}, \qquad m_{\tilde{\tau}_2} = 206.29 \text{ GeV}, \qquad \theta_{\tilde{\tau}} = 163.663°,$$
$$m_{\tilde{u}_1} = 537.20 \text{ GeV}, \qquad m_{\tilde{u}_2} = 520.50 \text{ GeV},$$
$$m_{\tilde{c}_1} = 537.20 \text{ GeV}, \qquad m_{\tilde{c}_2} = 520.50 \text{ GeV},$$
$$m_{\tilde{t}_1} = 375.90 \text{ GeV}, \qquad m_{\tilde{t}_2} = 584.63 \text{ GeV}, \qquad \theta_{\tilde{t}} = 144.275°,$$
$$m_{\tilde{d}_1} = 543.07 \text{ GeV}, \qquad m_{\tilde{d}_2} = 520.11 \text{ GeV},$$
$$m_{\tilde{s}_1} = 543.07 \text{ GeV}, \qquad m_{\tilde{s}_2} = 520.11 \text{ GeV},$$
$$m_{\tilde{b}_1} = 486.23 \text{ GeV}, \qquad m_{\tilde{b}_2} = 529.88 \text{ GeV}, \qquad \theta_{\tilde{b}} = 122.783°.$$

Higgs masses:

$$m_{h^0} = 111.62 \text{ GeV}, \qquad m_{H^0} = 394.14 \text{ GeV},$$
$$m_{A^0} = 393.63 \text{ GeV}, \qquad m_{H^\pm} = 401.76 \text{ GeV},$$

Neutralinos:

$$m_{\tilde{\chi}_1^0} = 377.87 \text{ GeV}, \qquad m_{\tilde{\chi}_2^0} = 358.80 \text{ GeV},$$
$$m_{\tilde{\chi}_3^0} = 176.62 \text{ GeV}, \qquad m_{\tilde{\chi}_4^0} = 96.18 \text{ GeV},$$

Charginos:

$$m_{\tilde{\chi}_1^+} = 378.51 \text{ GeV}, \qquad m_{\tilde{\chi}_2^+} = 176.06 \text{ GeV},$$

B.2   SPS 5

The MSSM parameter of SPS 5 are:

$$M_{\tilde{e}_L,\tilde{\mu}_L} = 252.24 \text{ GeV}, \qquad M_{\tilde{e}_R,\tilde{\mu}_R} = 186.76 \text{ GeV},$$
$$M_{\tilde{\tau}_L} = 250.13 \text{ GeV}, \qquad M_{\tilde{\tau}_R} = 180.89 \text{ GeV}, \qquad A_\tau = -1179.34 \text{ GeV},$$

$$M_{\tilde{u}_L,\tilde{d}_L,\tilde{c}_L,\tilde{s}_L} = 643.88 \text{ GeV}, \qquad M_{\tilde{u}_R,\tilde{c}_R} = 625.44 \text{ GeV},$$
$$M_{\tilde{d}_R \tilde{s}_R} = 622.91 \text{ GeV},$$
$$M_{\tilde{t}_L,\tilde{b}_L} = 535.16 \text{ GeV}, \qquad M_{\tilde{t}_R} = 360.54 \text{ GeV}, \qquad A_t = -905.63 \text{ GeV},$$
$$M_{\tilde{b}_R} = 620.50 \text{ GeV}, \qquad A_b = -1671.36 \text{ GeV},$$

$$\mu = 639.80 \text{ GeV}, \qquad M_{A^0} = 693.86 \text{ GeV}, \qquad \tan\beta = 5 \text{ GeV},$$
$$m_{\tilde{g}} = 710.31 \text{ GeV}, \qquad M_1 = 121.39 \text{ GeV}, \qquad M_2 = 234.56 \text{ GeV}.$$

The following masses and mixing angles arises:

Fermions:

$$m_{\tilde{e}_1} = 256.43 \text{ GeV}, \qquad m_{\tilde{e}_2} = 191.27 \text{ GeV},$$
$$m_{\tilde{\mu}_1} = 256.43 \text{ GeV}, \qquad m_{\tilde{\mu}_2} = 191.27 \text{ GeV},$$
$$m_{\tilde{\tau}_1} = 180.41 \text{ GeV}, \qquad m_{\tilde{\tau}_2} = 258.04 \text{ GeV}, \qquad \theta_{\tilde{\tau}} = 166.398°,$$
$$m_{\tilde{u}_1} = 641.78 \text{ GeV}, \qquad m_{\tilde{u}_2} = 624.53 \text{ GeV},$$
$$m_{\tilde{c}_1} = 641.78 \text{ GeV}, \qquad m_{\tilde{c}_2} = 624.53 \text{ GeV},$$
$$m_{\tilde{t}_1} = 201.42 \text{ GeV}, \qquad m_{\tilde{t}_2} = 657.83 \text{ GeV}, \qquad \theta_{\tilde{t}} = 146.628°,$$
$$m_{\tilde{d}_1} = 646.41 \text{ GeV}, \qquad m_{\tilde{d}_2} = 623.37 \text{ GeV},$$
$$m_{\tilde{s}_1} = 646.41 \text{ GeV}, \qquad m_{\tilde{s}_2} = 623.37 \text{ GeV},$$
$$m_{\tilde{b}_1} = 533.39 \text{ GeV}, \qquad m_{\tilde{b}_2} = 625.13 \text{ GeV}, \qquad \theta_{\tilde{b}} = 102.757°.$$

Higgs masses:

$$m_{h^0} = 114.46 \text{ GeV}, \qquad m_{H^0} = 694.95 \text{ GeV},$$
$$m_{A^0} = 693.86 \text{ GeV}, \qquad m_{H^\pm} = 698.51 \text{ GeV},$$

Neutralinos:

$$m_{\tilde{\chi}_1^0} = 652.97 \text{ GeV}, \qquad m_{\tilde{\chi}_2^0} = 642.83 \text{ GeV},$$
$$m_{\tilde{\chi}_3^0} = 226.22 \text{ GeV}, \qquad m_{\tilde{\chi}_4^0} = 119.59 \text{ GeV},$$

Charginos:

$$m_{\tilde{\chi}_1^+} = 652.83 \text{ GeV}, \qquad m_{\tilde{\chi}_2^+} = 226.07 \text{ GeV},$$

Bibliography

[1] Glashow, S. L., *Nucl. Phys.* 22 (1961) 579.

[2] Weinberg, S., *Phys. Rev. Lett.* 19 (1967) 1264.

[3] A. Salam. *Proceedings of the 8th Nobel Symposium.* ed. N. Svartholm, Almquist and Wiskell, Stockholm 1968.

[4] S. L. Glashow, J. Iliopoulos and L. Maiani, *Phys. Rev.* D2 (1970) 1285.

[5] H. Fritzsch, M. Gell-Mann and H. Leutwyler, *Phys. Lett.* B47 (1973) 365.

[6] Higgs, Peter W., *Phys. Lett.* 12 (1964) 132.

[7] Higgs, Peter W., *Phys. Rev. Lett.* 13 (1964) 508–509.

[8] Higgs, Peter W., *Phys. Rev.* 145 (1966) 1156–1163.

[9] Englert, F. and Brout, R., *Phys. Rev. Lett.* 13 (1964) 321–322.

[10] Kibble, T. W. B., *Phys. Rev.* 155 (1967) 1554–1561.

[11] Wess, J. and Zumino, B., *Phys. Lett.* B49 (1974) 52.

[12] Wess, J. and Zumino, B., *Nucl. Phys.* B70 (1974) 39–50.

[13] For an introduction see: J. Wess and J. Bagger. *Supersymmetry and Supergravity.* 2nd Edition, Princeton Series in Physics, 1992.

[14] Bityukov, S. I. and Krasnikov, N. V. (2002) [hep-ph/0210269].

[15] Brandenburg, A. and Maniatis, M. and Weber, M. M. (2002) [hep-ph/0207278].

[16] Nelson, Philip and Osland, Per, *Phys. Lett.* B115 (1982) 407.

[17] Kileng, B. and Osland, P., *Z. Phys.* C66 (1995) 503–512 [hep-ph/9407290].

[18] Campbell, B. A. and Scott, J. A. and Sundaresan, M. K., *Phys. Lett.* B126 (1983) 376–378.

[19] Kane, Gordon L. and Rolnick, William B., *Nucl. Phys.* B217 (1983) 117.

[20] Djouadi, A. and Drees, M., *Phys. Rev.* D51 (1995) 4997–5006 [hep-ph/9411314].

[21] 2001. *Report on the NLC: A report submitted to Snowmass '01.* Fermilab-Conf 01-075, LBLL-47935, SLAC-R-571; T. Abe et al. *Linear collider physics resource book for Snowmass 2001*, American Linear Collider Working Group, SLAC-R-570, May 2001.

[22] Koh et al. Abe. *Particle physics experiments at JLC.* ACFA Linear Collider Working Group, KEK-REPORT-2001-1, 2001 [hep-ph/0109166].

[23] Takahashi, T., *Nucl. Instrum. Meth.* A472 (2001) 4–11.

[24] I. et al. Watanabe. *gamma gamma collider as an option of JLC.* KEK-REPORT-97-17.

[25] H. Burkhardt and V. Telnov. *CLIC 3-TeV photon collider option.* CERN-SL-2002-013-AP, CLIC-NOTE-508, May 2002.

[26] B. Badelek et al. *TESLA Technical Design Report, Part VI, Chapter 1: Photon collider at TESLA.* ECFA/DESY Photon Collider Working Group, 2001 [hep-ex/0108012].

[27] Telnov, V., *Nucl. Instrum. Meth.* A472 (2001) 43–60 [hep-ex/0010033].

[28] Ginzburg, I. F. et al., *JETP Lett.* 34 (1981) 491.

[29] Ginzburg, I. F. et al., *Nucl. Instr. Meth.* 205 (1983) 47.

[30] Drees, Manuel and Hikasa, Ken-ichi, *Phys. Lett.* B252 (1990) 127–134.

[31] Beenakker, W. and Hopker, R. and Zerwas, P. M., *Phys. Lett.* B349 (1995) 463–468 [hep-ph/9501292].

[32] Arhrib, A. and Capdequi-Peyranere, M. and Djouadi, A., *Phys. Rev.* D52 (1995) 1404–1417 [hep-ph/9412382].

[33] Eberl, H. and Bartl, A. and Majerotto, W., *Nucl. Phys.* B472 (1996) 481–494 [hep-ph/9603206].

[34] Sabine Kraml. *Stop and sbottom phenomenology in the MSSM.* 1999 [hep-ph/9903257].

[35] Chang, C.-H. et al., *Nucl. Phys.* B515 (1998) 15–33 [hep-ph/9704413].

[36] H. Spiesberger, M. Spira and P. M. Zerwas, in: *Scattering,* ed. P. Sabatier, Academic Press, London. (2000) [hep-ph/0011255].

[37] Y. Fukuda et al., *Phys. Rev. Lett.* 82 (1999) 2644 [hep-ex/9812014].

[38] S. Fukuda et al., *Phys. Rev. Lett.* 86 (2001) 5651 [hep-ex/0103032].

[39] Q. R. Ahmad et al., *Phys. Rev. Lett.* 89 (2002) 011302 [nucl-ex/0204009].

[40] M. Gell-Mann, P. Ramond and R. Slansky, in Supergravity, ed.F. van Nieuwen-huizen and D. Freedman, North Holland 1979; T. Yanagida, Proceedings, Unified Theory and the Baryon Number in the Universe, KEK 1979; Mohapatra, Ra-bindra N. and Senjanovic, Goran, *Phys. Rev. Lett.* 44 (1980) 912.

[41] Blair, G. A. and Porod, W. and Zerwas, P. M., *Eur. Phys. J.* C27 (2003) 263–281 [hep-ph/0210058].

[42] Cabibbo, N., *Phys. Rev. Lett.* 10 (1963) 531–532.

[43] Kobayashi, M. and Maskawa, T., *Prog. Theor. Phys.* 49 (1973) 652–657.

[44] LEP Higgs working group, *Phys. Lett.* B565 (2003) 61–75 [hep-ex/0306033, http://lephiggs.web.cern.ch/LEPHIGGS/papers/].

[45] E. Witten, *Nucl. Phys.* B188 (1981) 513.

[46] Machacek, M. E. and Vaughn, M. T., *Nucl. Phys.* B222 (1983) 83.

[47] Machacek, M. E. and Vaughn, M. T., *Nucl. Phys.* B236 (1984) 221.

[48] Machacek, M. E. and Vaughn, M. T., *Nucl. Phys.* B249 (1985) 70.

[49] Ibanez, L. E. and Ross, G. G., *Phys. Lett.* B105 (1981) 439.

[50] L. E Ibanez, C. Lopez and C. Munoz, *Nucl. Phys.* B256 (1985) 218–252.

[51] Einhorn, M. B. and Jones, D. R. T., *Nucl. Phys.* B196 (1982) 475.

[52] V. D. Barger, M. S. Berger and P. Ohmann, *Phys. Rev.* D47 (1993) 1093–1113 [hep-ph/9209232].

[53] U. Amaldi, W. de Boer and H. Furstenau, *Phys. Lett.* B260 (1991) 447–455.

[54] de Boer, W., *Prog. Part. Nucl. Phys.* 33 (1994) 201–302 [hep-ph/9402266].

[55] H. Georgi, H. R. Quinn and S. Weinberg, *Phys. Rev. Lett.* 33 (1974) 451–454.

[56] S. Weinberg, *Phys. Lett.* B62 (1976) 111.

[57] E. Gildener and S. Weinberg, *Phys. Rev.* D13 (1976) 3333.

[58] L. Susskind, *Phys. Rev.* D20 (1979) 2619–2625.

[59] Martin, S. P. (1997) [hep-ph/9709356].

[60] J. R. Ellis et al., *Nucl. Phys.* B238 (1984) 453–476.

[61] Freedman, Daniel Z. and van Nieuwenhuizen, P. and Ferrara, S., *Phys. Rev.* D13 (1976) 3214–3218.

[62] Deser, S. and Zumino, B., *Phys. Lett.* B62 (1976) 335.

[63] Van Nieuwenhuizen, P., *Phys. Rept.* 68 (1981) 189–398.

[64] Nilles, H. P., *Phys. Rept.* 110 (1984) 1.

[65] H. E. Haber and G. L. Kane, *Phys. Rept.* 117 (1985) 75.

[66] Gunion, J. F. and Haber, H. E., *Nucl. Phys.* B272 (1986) 1.

[67] Girardello, L. and Grisaru, M. T., *Nucl. Phys.* B194 (1982) 65.

[68] S. Weinberg. *The Quantum Theory of Fields.* Vol.II, Cambridge University Press, 1996.

[69] T. Kugo. *Eichtheorie.* Springer Verlag, Berlin 1997.

[70] T. Fritzsche. *Untersuchungen zum Massenspektrum von Neutralinos und Charginos im MSSM.* Diploma Thesis, 2003.

[71] Eidelman, S. and Jegerlehner, F., *Z. Phys.* C67 (1995) 585–602 [hep-ph/9502298].

[72] Burkhardt, H. and Pietrzyk, B., *Phys. Lett.* B356 (1995) 398–403.

[73] Plothow-Besch, H., *Int. J. Mod. Phys.* A10 (1995) 2901–2920.

[74] K. Hagiwara et al., *PDG-Review 'Quantum chromodynamics', Physical Review D.* 66 (2002) 010001 [http://pdg.lbl.gov].

[75] T. Affolder et al., *Phys. Rev. Lett.* 88 (2002) 041801 [hep-ex/0106001].

[76] S. Abachi et al., *Phys. Rev. Lett.* 75 (1995) 618–623.

[77] K. Hagiwara et al., [Particle Data Group Collaboration], *Phys. Rev.* D66 (2002) 010001 [http://pdg.lbl.gov].

[78] J. Abdallah et al. *LEP SUSY Working Group Collaboration.* 2002 [http://lepsusy.web. cern.ch/lepsusy].

[79] Barbieri, R. and Maiani, L., *Nucl. Phys.* B224 (1983) 32.

[80] Drees, M. and Hagiwara, K., *Phys. Rev.* D42 (1990) 1709–1725.

[81] P. H. Chankowski et al., *Nucl. Phys.* B417 (1994) 101–129.

[82] Bollini, C. G. and Giambiagi, J. J., *Nuovo Cim.* B12 (1972) 20–25.

[83] Ashmore, J. F., *Lett. Nuovo Cim.* 4 (1972) 289–290.

[84] 't Hooft, Gerard and Veltman, M. J. G., *Nucl. Phys.* B44 (1972) 189–213.

[85] Hollik, W. and Kraus, E. and Stockinger, D., *Eur. Phys. J.* C23 (2002) 735–747 [hep-ph/0007134].

[86] Hollik, W. and Stockinger, D., *Eur. Phys. J.* C20 (2001) 105–119 [hep-ph/0103009].

[87] Siegel, W., *Phys. Lett.* B84 (1979) 193.

[88] D. M. Capper, D. R. T. Jones and P. van Nieuwenhuizen, *Nucl. Phys.* B167 (1980) 479.

[89] I. Jack et al., *Phys. Rev.* D50 (1994) 5481 [hep-ph/9407291].

[90] Siegel, W., *Phys. Lett.* B94 (1980) 37.

[91] 't Hooft, G., *Nucl. Phys.* B61 (1973) 455.

[92] 't Hooft, G., *Nucl. Phys.* B62 (1973) 444.

[93] Ross, D. A. and Taylor, J. C., *Nucl. Phys.* B51 (1973) 125. Erratum-ibid. B58 (1973) 643.

[94] Bohm, M. and Spiesberger, H. and Hollik, W., *Fortsch. Phys.* 34 (1986) 687.

[95] Hollik, Wolfgang and others, *Nucl. Phys.* B639 (2002) 3–65 [hep-ph/0204350].

[96] Hollik, W. and Rzehak, H. (2003) [hep-ph/0305328].

[97] H. Rzehak. *Das Sfermion-Massenspektrum des Minimalen Supersymmetrischen Standardmodells auf Einschleifenniveau, Diploma Thesis.* 2001.

[98] W. Hollik. *Renormalization of the Standard Model.* 1993. MPI-PH-93-21.

[99] Dabelstein, A., *Z. Phys.* C67 (1995) 495–512 [hep-ph/9409375].

[100] P. Chankowski, S. Pokorski and J. Rosiek, *Nucl. Phys.* B423 (1994) 437–496 [hep-ph/9303309].

[101] Hahn, T. and Schappacher, C., *Comput. Phys. Commun.* 143 (2002) 54–68 [hep-ph/0105349].

[102] J. Kublbeck, M. Bohm and A. Denner, *Comput. Phys. Commun.* 60 (1990) 165–180.

[103] Hahn, T., *Comput. Phys. Commun.* 140 (2001) 418–431 [hep-ph/0012260].

[104] T. Fritzsche. privat communication. 2003.

[105] R. W. Assmann et al. *A 3-TeV e+ e- linear collider based on CLIC technology.* CERN-2000-008.

[106] B. et al. Badelek. *TESLA: The Superconducting electron positron linear collider with an integrated X-ray laser laboratory.* Technical Design Report, DESY 2001-011, ECFA 2001-209, TESLA Report 2001-23, TESLA-FEL 2001-05, March 2001.

[107] T. et al. Abe. *Linear collider physics resource book for Snowmass 2001. 4: Theoretical, accelerator, and experimental options.* American Linear Collider Working Group, 2001 [hep-ex/0106058].

[108] Ginzburg, I. F. et al., *Nucl. Instr. Meth.* A219 (1984) 5.

[109] Telnov, V. I., *Nucl. Instrum. Meth.* A294 (1990) 72.

[110] Telnov, V., *Nucl. Instrum. Meth.* A355 (1995) 3.

[111] D. Schulte. *Study of electromagnetic and hadronic background in the interaction region of the TESLA Collider.* Dissertation. DESY-TESLA-97-08.

[112] E.M. Lifshitz W.B. Berestetzky and L.P. Pitajewski. *Lehrbuch der Theoretischen Physik. Band 4.* 19986.

[113] G. L Kotkin, V. G. Serbo and A. Schiller, *Int. J. Mod. Phys.* A7 (1992) 4707–4745.

[114] K. Yokoya and P. Chen. *Beam-beam phenomena in linear colliders.* Tsukuba KEK - KEK-Prepr.-91-002 (91/04,rec.Jul.) 36 p.

[115] Schulte, D., *eConf.* C980914 (1998) 127.

[116] Ohl, Thorsten, *Comput. Phys. Commun.* 101 (1997) 269–288 [hep-ph/9607454].

[117] Telnov, V., *Nucl. Instrum. Meth.* A494 (2002) 35–44 [hep-ex/0207093].

[118] M. V. Galynskii et al., *Nucl. Instrum. Meth.* A472 (2001) 267–279 [hep-ph/0012338].

[119] Ginzburg, I. F. and Kotkin, G. L., *Eur. Phys. J.* C13 (2000) 295–300 [hep-ph/9905462].

[120] Zarnecki, A. F., *Acta Phys. Polon.* B34 (2003) 2741–2758 [hep-ex/0207021].

[121] V. Telnov. *privat communication.* 2003.
http://www.desy.de/~telnov/ggtesla/spectra/.

[122] Klasen, M. et al., *Nucl. Phys.* B609 (2001) 518–536 [hep-ph/0104044].

[123] Hahn, T. and Perez-Victoria, M., *Comput. Phys. Commun.* 118 (1999) 153–165 [hep-ph/9807565].

[124] Vermaseren, J. A. M. (2000) [math-ph/0010025].

[125] Mertig, R. and Bohm, M. and Denner, A., *Comput. Phys. Commun.* 64 (1991) 345–359.

[126] Passarino, G. and Veltman, M. J. G., *Nucl. Phys.* B160 (1979) 151.

[127] van Oldenborgh, G. J., *Comput. Phys. Commun.* 66 (1991) 1–15.

[128] van Oldenborgh, G. J. and Vermaseren, J. A. M., *Z. Phys.* C46 (1990) 425–438.

[129] G. P. Lepage. *VEGAS: An adaptive Multidimensional Integration Program.* 1980. CLNS-80/447.

[130] W. H. Press et al. *Numerical recipes in Fortran 77 and Fortran 90 : Source code for recipes and example programs.* 1996 [http://www.nr.com]. Cambridge Univ. Press.

[131] Berge, S. and Klasen, M., *Phys. Rev.* D66 (2002) 115014 [hep-ph/0208212].

[132] A. Denner et al., *Nucl. Phys.* B387 (1992) 467–484.

[133] A. Freitas, A. von Manteuffel and P. M. Zerwas. (2003) [hep-ph/0310182].

[134] Berge, S. and Klasen, M. (2003) [hep-ph/0303032].

[135] Li, S. P. and Liu, H. C. and Silverman, Dennis, *Phys. Rev.* D31 (1985) 1736.

[136] Allanach, B. C. et al., *Eur. Phys. J.* C25 (2002) 113–123 [hep-ph/0202233].

[137] M. Gluck, E. Reya and A. Vogt, *Phys. Rev.* D45 (1992) 3986–3994.

[138] S. Dawson, E. Eichten and C. Quigg, *Phys. Rev.* D31 (1985) 1581.

[139] Berge, S. and Klasen, M. and Umeda, Y., *Phys. Rev.* D63 (2001) 035003 [hep-ph/0008081].

[140] Grifols, J. A. and Sola, J., *Z. Phys.* C18 (1983) 185.

[141] Rizzo, T. G., *Phys. Rev.* D40 (1989) 2803.

[142] F. Cuypers, G. J. van Oldenborgh and R. Ruckl, *Nucl. Phys.* B409 (1993) 144–160 [hep-ph/9302302].

[143] Kon, T., *Phys. Lett.* B316 (1993) 181–187 [hep-ph/9307257].

[144] Choudhury, D. and Datta, A., *Nucl. Phys.* B592 (2001) 35–54 [hep-ph/0005082].

[145] S. Kraml. *Stop and Sbottom Phenomenology in the MSSM, Dissertation.* 1999 [hep-ph/9903257].

[146] F. del Aguila et al., *Nucl. Phys.* B537 (1999) 561–585 [hep-ph/9806451].

[147] D.Z. Freedman, K. Johnson and J.I. Latorre, *Nucl. Phys.* B371 (1992) 353–414.

[148] F. del Aguila et al., *Phys. Lett.* B419 (1998) 263–271 [hep-th/9709067].

[149] Lee, T. D. and Nauenberg, M., *Phys. Rev.* 133 (1964) B1549–B1562.

[150] Denner, A., *Fortschr. Phys.* 41 (1993) 307–420.

[151] 't Hooft, G. and Veltman, M. J. G., *Nucl. Phys.* B153 (1979) 365.

[152] A. Sommerfeld. *Atombau und Spektrallinien Bd. 2.* Braunschweig (1939).

[153] Muta, T., *World Sci. Lect. Notes Phys.* 57 (1998) 1.

[154] Nabil Ghodbane and Hans-Ulrich Martyn. *Compilation of SUSY particle spectra from Snowmass 2001 benchmark models.* 2002 [hep-ph/0201233].

Acknowledgement

Ich versichere, diese Arbeit selbständig verfaßt und keine anderen als die angegebenen Quellen und Hilfsmittel benutzt zu haben.

Stefan Berge
Hamburg, November 2003